4-2019

Bedrock Topography Mapping of the East Leroy and Climax 7.5' Quadrangles, MI using HVSR and Other Geophysical Methods

Tyler A. Norris

BEDROCK TOPOGRAPHY MAPPING OF THE EAST LEROY AND CLIMAX 7.5' QUADRANGLES, MI USING HVSR AND OTHER GEOPHYSICAL METHODS

by

Tyler A. Norris

A thesis submitted to the Graduate College
in partial fulfillment of the requirements
for the degree of Master of Science
Geological and Environmental Sciences
Western Michigan University
April 2019

Thesis Committee:

Alan E. Kehew, Ph.D., Chair
William A. Sauck, Ph.D.
Robb Gillespie, Ph.D.

ACKNOWLEDGEMENTS

I thank Dr. Alan Kehew for taking me on as his graduate student and for his guidance throughout the whole project. I also thank Dr. William Sauck, who supported me through many days of field work and processing geophysical data. I additionally thank Dr. Robb Gillespie for providing feedback and ideas for multiple aspects of the project. This project would not have been possible without the aid of the Groundwater Research and Education Foundation Grant. I give great thanks to John Yellich, the director of the Michigan Geologic Survey, who helped obtain the grant and arranged drilling operations. Wolverine Gas and Oil, West Bay Exploration, & SEI also deserve acknowledgement for providing industry seismic data. I also thank John Esch of Michigan's DEQ for helping with HVSR interpretation, mapping techniques, and gamma logging. I also thank the residents of the East Leroy- Climax area for allowing me to work on their lands. I especially thank the Hunt's and Steury's for permitting drilling on their property.

Others who sacrificed their time to support me in the field and lab also deserve recognition, such as Clay Juopperini, Austin Johnson, and Guzalay Satar. I also give special thanks to Ben Seiderman and Karl Backhaus, who taught me the basics of field and GIS mapping and introduced the Tromino to me. I especially thank my significant other Alyson Poorbaugh for her constant support and spending countless hours accommodating me while I worked on the project. I also thank my family and friends for their undying support.

Tyler A. Norris

BEDROCK TOPOGRAPHY MAPPING OF THE EAST LEROY AND CLIMAX 7.5' QUADRANGLES, MI USING HVSR AND OTHER GEOPHYSICAL METHODS

Tyler A. Norris, M.S.

Western Michigan University, 2019

Geophysical methods were used to estimate bedrock depths below sedimentary cover and infer previously unknown features in two adjacent topographic quadrangles (Climax & East Leroy) in Michigan, USA. The study area contains mostly Mississippian Shale bedrock overlain by Wisconsin-aged glacial drift deposited during multiple glacial advances and retreats of the Saginaw Lobe (Laurentide Ice Sheet). These glacial events created complex landform assemblages that have only recently been mapped in detail near-surface, but are still poorly understood in the subsurface. Buried bedrock valleys typically contain coarse glacial sediment and thus are valuable aquifers, but these can be difficult to locate due to a lack of surface expression and bedrock topography information. The Horizontal to Vertical Spectral Ratio (HVSR) technique was used to estimate the thickness of the upper of a two-layer case where a soft unconsolidated geologic layer (glacial sediment) is underlain by a harder substrate (bedrock). Additional techniques such as vertical resistivity soundings and active seismic refraction/reflection surveys were employed to compare with HVSR, boring logs, and industry seismic data results to better understand the subsurface. This study resulted in the discovery of several bedrock lows that are interpreted as bedrock valleys or tunnel valleys, which may contain aquifers and provide insight to Pleistocene glacial history. Bedrock highs correspond to terminal ice margins and have some control over post-glacial drainage systems.

TABLE OF CONTENTS

Table of Contents -- Continued

LIST OF TABLES

LIST OF FIGURES

List of Figures -- Continued

List of Figures -- Continued

CHAPTER I

INTRODUCTION

Glacial geomorphologic interpretations of Michigan are based largely on Leverett and Taylor's 1915 monograph, although newer interpretations provide additional insight into the area's glacial history. This century old study provided an unprecedented understanding of surficial deposits of the Great Lakes region but included only general assumptions of the subsurface from sparse water well data. Other publications such as Martin (1955) and Farrand and Bell (1982) further developed the glacial history of the Southern Peninsula. Although Leverett and Taylor's work was remarkable on a regional scale, current investigations must address issues relating to groundwater flow, aggregate mining, bedrock topography, and glacial deposits in greater detail by using modern methods. Much of southwestern Michigan is stratigraphically complex due to multiple glacial lobe interactions, asynchronous ice sheet movements, and the resulting over-riding features. Moreover, current trends in population growth and agricultural irrigation demand more groundwater extraction, and mapping efforts are now critical to the discovery and protection of aquifers and other natural resources.

Delineating bedrock valleys is an important aspect of these subsurface studies. Bedrock valleys are often infilled with highly permeable sediments that constitute productive aquifers and provide zones of preferential groundwater pathways. During the most recent ice age, meltwater discharged from the retreating wet-based glacial ice produced high velocity subglacial streams that flowed into available channels or eroded new channels. These specific types of bedrock valleys are known as tunnel valleys. An important distinction between the two terms for a valley should be made during interpretation. "Bedrock Valleys" are incised bedrock lows that may originate from fluvial processes with no implied glacial influence, whereas "Tunnel Valleys"

have hummocky sides and bottoms formed from high velocity subglacial meltwater flow. Furthermore, another term “Tunnel Channel” infers a genetic origin involving catastrophic river erosion and channel filling, whereas a “Tunnel Valley” is a broader term used for a subglacial valley incised and then broadened through the discharge of additional glacial meltwater (O’Cofaigh, 1996; Clayton et al., 1999). This subglacial origin of a valley is further evidenced by the occurrence of outwash fans at moraine breaches (Clayton et al., 1999). These tunnel valley features are typically parallel to glacial ice flow and are sometimes buried by subsequent sediment deposited during glacial retreat episodes (Kehew et al., 2013).

Locating buried tunnel or bedrock valleys is often a challenging task that requires the utilization of various methods. The principal technique used in this study is the Horizontal to Vertical Spectral Ratio (HVSR) method, which provides a low cost, rapid, and effective means of estimating depth to bedrock by using passive seismic energy. This technique is accomplished by first determining a peak resonance frequency (f_0) of a sediment layer overlying bedrock with a high shear wave acoustic impedance. The thickness of the sediment layer can then be calculated if its shear wave velocity (Vs) is known (Chandler and Lively, 2016). Because a characteristic shear wave velocity is typically not known, a calibration curve can be developed by using control wells and by creating a reliable relationship between the observed peak frequency and measured sediment thickness.

Portions of Kalamazoo and Calhoun counties in southwestern Michigan, USA have yet to be properly mapped to bedrock, but are suspected to contain bedrock valleys based on glacial history and surface features. Surveyed HVSR data analyzed in conjunction with other geophysical methods along with direct subsurface information from boring logs can generate a more accurate representation of the bedrock surface. The synthesis of various datasets provides

an ideal opportunity to discover bedrock glacial features based on drift thicknesses and bedrock morphology.

Study Area

The Climax and East Leroy 7.5-minute USGS topographic quadrangles are located in southwestern Michigan, USA (Figure 1). The western one-third of the Climax quadrangle lies within Kalamazoo County, while the remaining portion of the study area lies within Calhoun County. The East Leroy quadrangle has several surficial valleys identifiable on LiDAR imagery based on relationships of lakes, rivers, and wetlands. Surface water also flows in a dendritic pattern away from a drainage divide towards the north eastern and south western parts of the study area. Surface water flows through Graham, Pearl, and Sonoma Lakes, which are large lakes nestled within surficial tunnel valleys, and Cotton Lake, which is located within the same deep valley containing Pine Creek. Several man-made surface water drainage systems have also been excavated in parts of the study area.

Both the Climax and East Leroy quadrangles lie within the path of the Saginaw Lobe of the Laurentide Ice Sheet, although deeper deposits formed during earlier glacial events may exist. Since Leverett and Taylor's 1915 mapping efforts, additional mapping has occurred and surficial interpretations have been expanded (e.g., Kozlowski, 1999; Kehew and Esch, 2013; Kehew and Esch, 2014). The Sturgis Moraine and the Kalamazoo Moraine of the Saginaw Lobe are located south and north of the study area, respectively. A portion of the uplands known as the Tekonsha Margin (moraine) is situated within the mapped quadrangles (Figure 2). A collection of elongated hills interpreted as drumlins dominate much of the Climax quadrangle and extend into East Leroy (Figure 3). This area is known as the Union Streamlined Plain (Dodson, 1985). These drumlins and other topographic uplands are composed of poorly sorted, non-stratified

glacial sediments known as diamicton. Although no surficial evidence suggests that tunnel valleys occur in the Climax quadrangle, two surficial tunnel valleys were identified in the East Leroy quadrangle (Kehew and Esch, 2014). These valleys and others may have similar shape in the underlying bedrock topography. At least one speculative north-south trending tunnel valley was hypothesized in prior works based on the deep, approximately N-S trending surficial valley occupied by Pine Creek (Kehew et al., 2017).

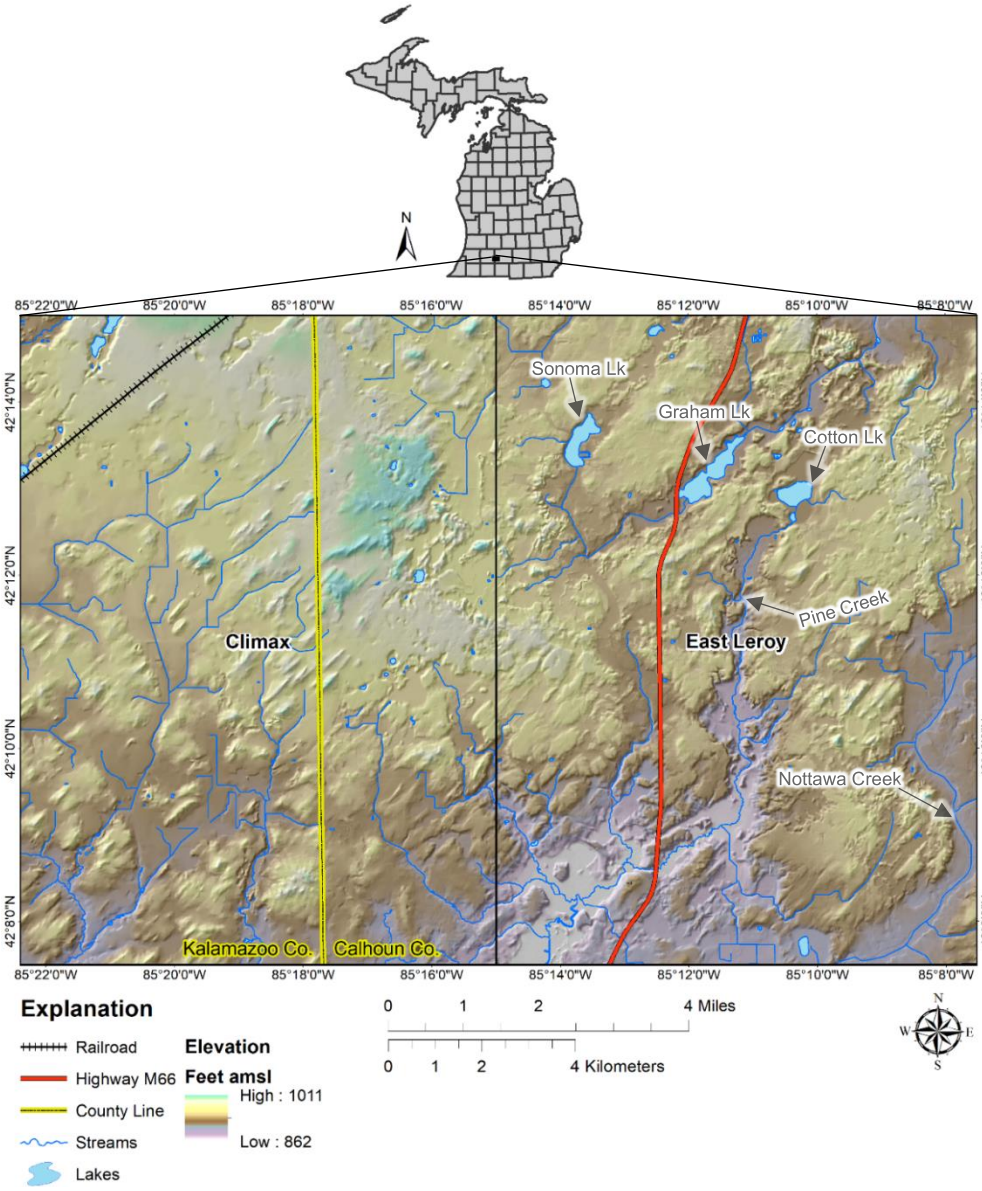

Figure 1. Study area location in Michigan, USA. LiDAR digital elevation model (DEM) is overlain with hillshade to display surficial elevation throughout the Climax and East Leroy quadrangles.

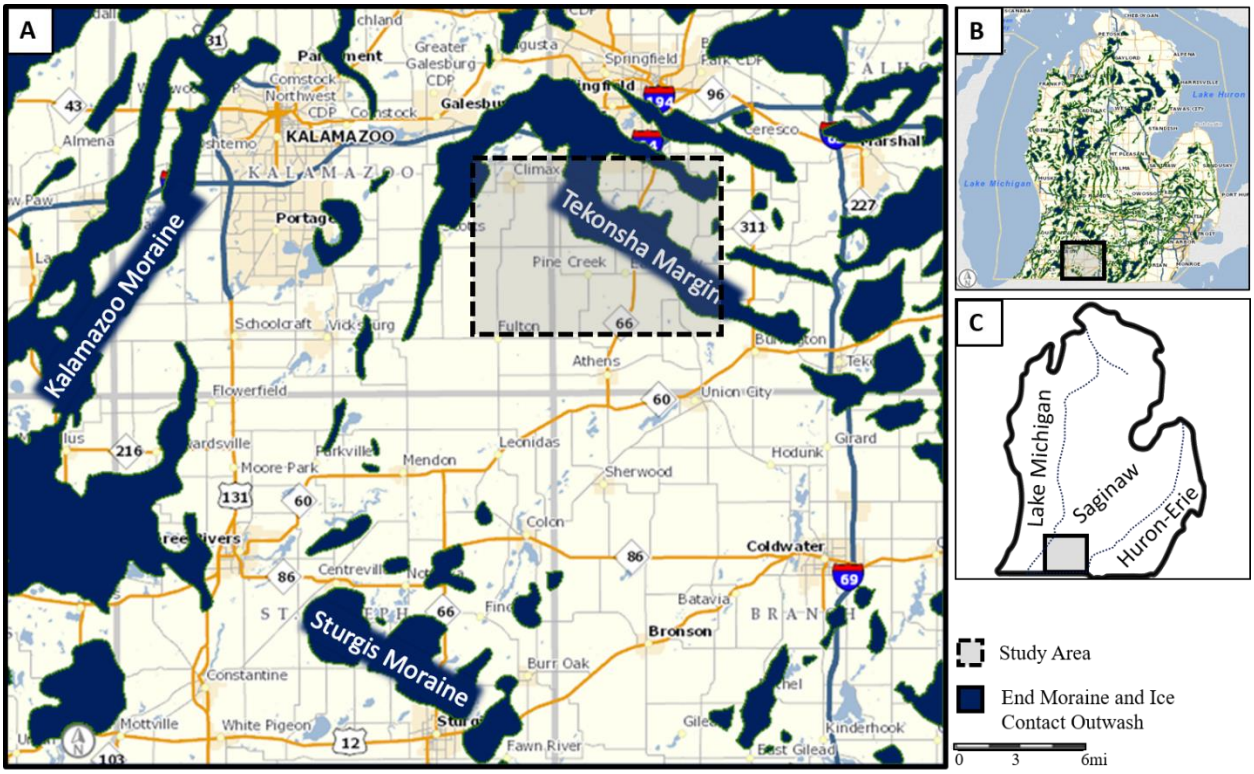

Figure 2. Reference maps displaying glacial lobe and moraine deposits both within and surrounding the shaded study area (data adapted from DEQ Geowebface). **(A)** Map showing approximate end moraine and contact deposits in a portion of southwestern Michigan. Note that the Tekonsha Moraine (Margin) lies within Climax and East Leroy quadrangles. Also note that the Kalamazoo Moraine continues to the north of the map. **(B)** Overview map displaying morainal features within Michigan's Lower Peninsula. The field of view in part A is outlined. **(C)** Generalized glacial lobe boundaries of Michigan's Lower Peninsula. Note that the field of view in part A is primarily composed of the path of the Saginaw Lobe, as is the study area.

The land in this area is predominantly used for agriculture and is populated with farms, crop fields, and rural residents. According to the State of Michigan Wellogic database, the area covered by (and surrounding) the East Leroy and Climax quadrangles contains over 3,000 water wells. Over 400 of these wells are reported to penetrate bedrock. Water supplies in the area are largely provided by groundwater aquifers for drinking water and irrigation purposes. According to the Michigan DEQ Geowebface, environmental assessments confirm several contaminated sites throughout the study area, with concentrations in urban regions such as the towns of Climax

and Athens. Noted pollutants include nitrates and light non-aqueous phase liquids (LNAPLs), such as benzene and xylenes. Well installations in the area often tap into deeper aquifers to avoid drawing from contaminated bodies. Agriculture is prevalent in much of the study area; corn crops are in constant need of fertilization, which further contributes to groundwater nitrate contamination.

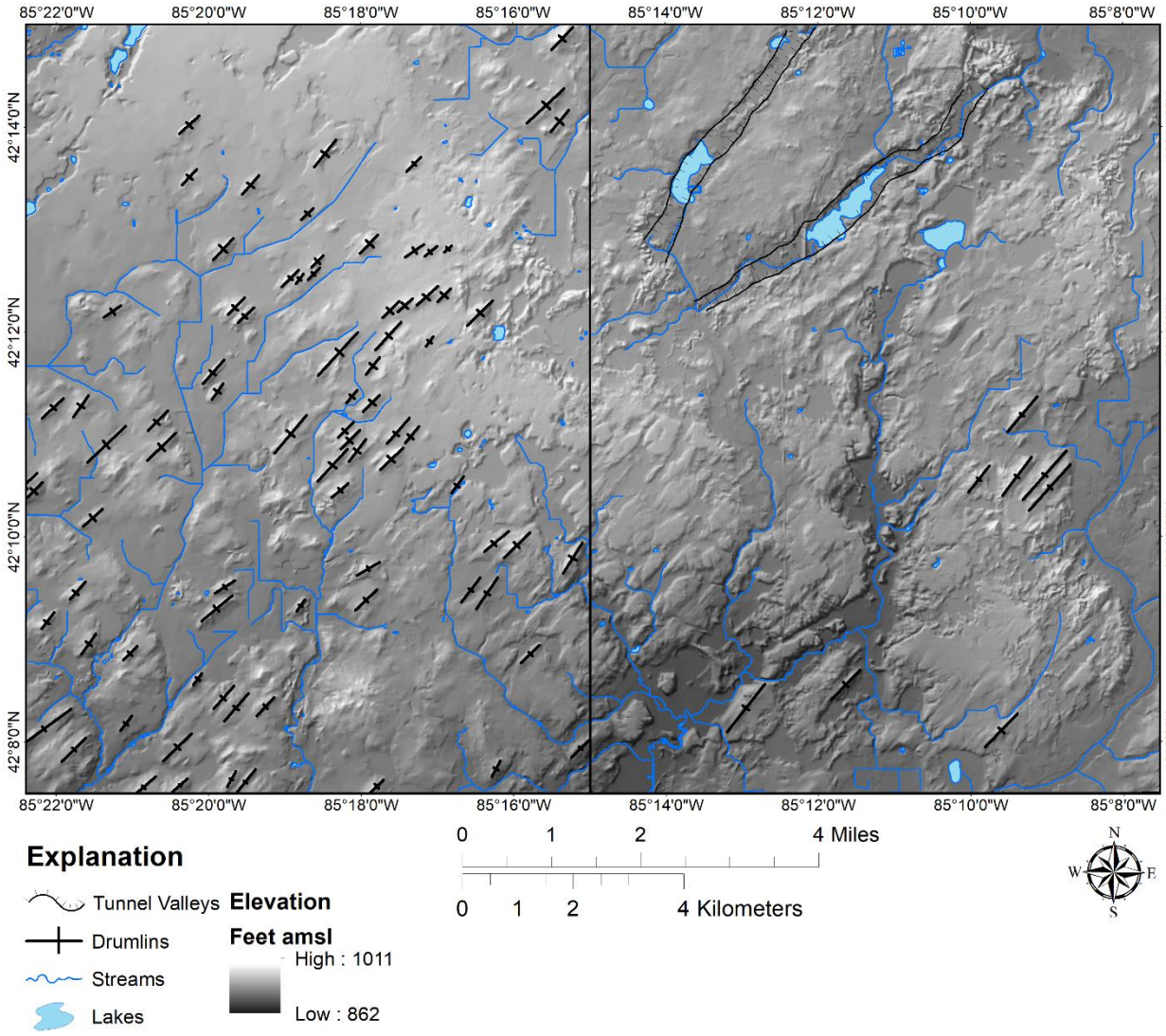

Figure 3. Several surficial geologic features in the study area. Note the NE-SW oriented drumlins and tunnel valleys. Also note the relatively deep surficial valley extending roughly N-S and NE-SW though the middle of the East Leroy quadrangle.

Previous geological studies in the area provided regional scale resolution of bedrock topography and drift thickness, but a few studies detailed smaller subregions within or around the East Leroy and Climax quadrangles. Generalized bedrock geologies and drift thicknesses were included in the Hydrogeologic Atlas of Michigan (Rieck, 1983) by using water well records. Recent GIS bedrock mapping compilations were also produced by the Michigan Department of Environmental Quality (John Esch, personal communication). Localized studies include data from Farnsworth (1980), which indicated the presence of buried valleys from four several mile-long gravity profiles within the East Leroy quadrangle and north towards Battle Creek. Additionally, Kozlowski (1999) detailed surficial geology in the East Leroy and Union City quadrangles by using sediment texture analysis and field mapping techniques to infer drift thickness and composition. The Climax and East Leroy quadrangles were surficially mapped by Kehew and Esch (2013; 2014) as part of a Great Lakes Geologic Mapping Coalition project. These mapping projects also provided additional understandings of bedrock geology and drift thickness by performing three rotosonic borings that penetrated bedrock.

Objectives

This study was designed to employ shallow geophysical methods to assess bedrock topography and drift thickness and to identify glacial features that may constitute valuable groundwater resources in unconsolidated sediments. First, an HVSR survey was conducted across two topographic quadrangles to determine bedrock topography and to identify buried glacial features (most notably, tunnel valleys that incise bedrock). The passive seismic method was used to demonstrate the effectiveness of this low-cost, rapidly applied field technique where bedrock depth was previously unmapped in detail. Additionally, active seismic refraction/reflection profiles and vertical resistivity soundings were performed over several locations, primarily those thought to lie above a possible tunnel valley, to compare with the HVSR findings. Two test borings within portions of the speculated valley were drilled for the project to provide subsurface information and more bedrock control. Moreover, three interpreted 2D seismic lines provided by West Bay Exploration and Wolverine Gas and Oil were used to verify HVSR determined bedrock depths and topography.

CHAPTER II

GEOLOGICAL BACKGROUND

Bedrock Geology

The study area is located within the Michigan Basin, which regionally slopes gently inward towards the center of the intracratonic basin. This basin is known for notable resource extraction, including oil, rock salt, potash, and gypsum. Rock layers in the Michigan Basin range from Early Paleozoic to Mesozoic in age. Tectonic activities contributing to the structural formation of the Michigan Basin are typically interpreted as a result of the late Appalachian and Acadian Orogenies (Howell & van der Pluijm, 1990). Such orogenic pulses facilitated subsidence in the basin and created sources of clastic input eroded from the uplifting Appalachian Mountains during the Paleozoic Era. Although the Michigan Basin is currently considered seismically inactive, the continued occurrence of low magnitude earthquakes is speculated to be caused by fault line structures in the bedrock that trend approximately NE-SW and NW-SE. Two localized earthquakes immediately adjacent to the study area (one in Scotts, Kalamazoo Co. and another in Union City, Calhoun Co.) occurred during 2015. These events suggest that such fault lines also run throughout portions of the bedrock in the study site (Fujita and Sleep, 1991).

Mississippian-age bedrock near the surface throughout the study area is composed of the Coldwater Shale with occurrences of the conformably overlying Marshall Sandstone (Figure 4). These units formed as a result of erosion and multiple transgressive and regressive sequences typically found throughout most of the basin's stratigraphy. Understanding the study area's bedrock geology is important for the geophysical portion of the investigation and eventual

interpretation of glacial features. The Marshall Sandstone is typically well-lithified compared to the underlying Coldwater Shale; however, it can be unconsolidated at the 'weathered' bedrock surface. The Marshall Sandstone denotes the base of the Mississippian aquifer, whereas the Coldwater Shale acts as a semi-confining hydrogeologic unit (Olcott, 1992). Water wells drilled into units deep within the Coldwater Shale often yield groundwater that is high in dissolved solids or brines (Olcott, 1992). Because of salinity issues with extracting water from these deep units, shallow wells drilled into coarse drift are often preferred (when the Marshall Sandstone is not present).

The Coldwater Shale is chiefly a variously shaded green to blue silty shale with minor limestone and dolomite intervals (Keller and Rexroad, 1986). The unit was deposited in an off-shore marine environment during the end of a major regression sequence in the Mississippian Period (Dorr and Eschman 1970). This unit is seldom tapped as a water source within the study area because of its impermeable, fine-grained lithology. Iron concretions sporadically occur throughout the shale. The Coldwater Shale is characterized in seismic reflection sections by a doublet caused by a consolidated dolomite-limestone interval near the middle to upper portions of the unit (Milstein, 1987). This doublet could be an issue of importance in HVSR interpretation, as it could mark a false base of glacial drift if the hard dolostone is overlain by weathered or unconsolidated shale. However, because the Coldwater Shale is typically weathered and eroded at the contact between it and the overlying drift, HVSR readings may be adversely affected due to a low shear wave acoustic impedance contrast. This situation would present difficulty when attempting to interpret the contact surface with geophysical results.

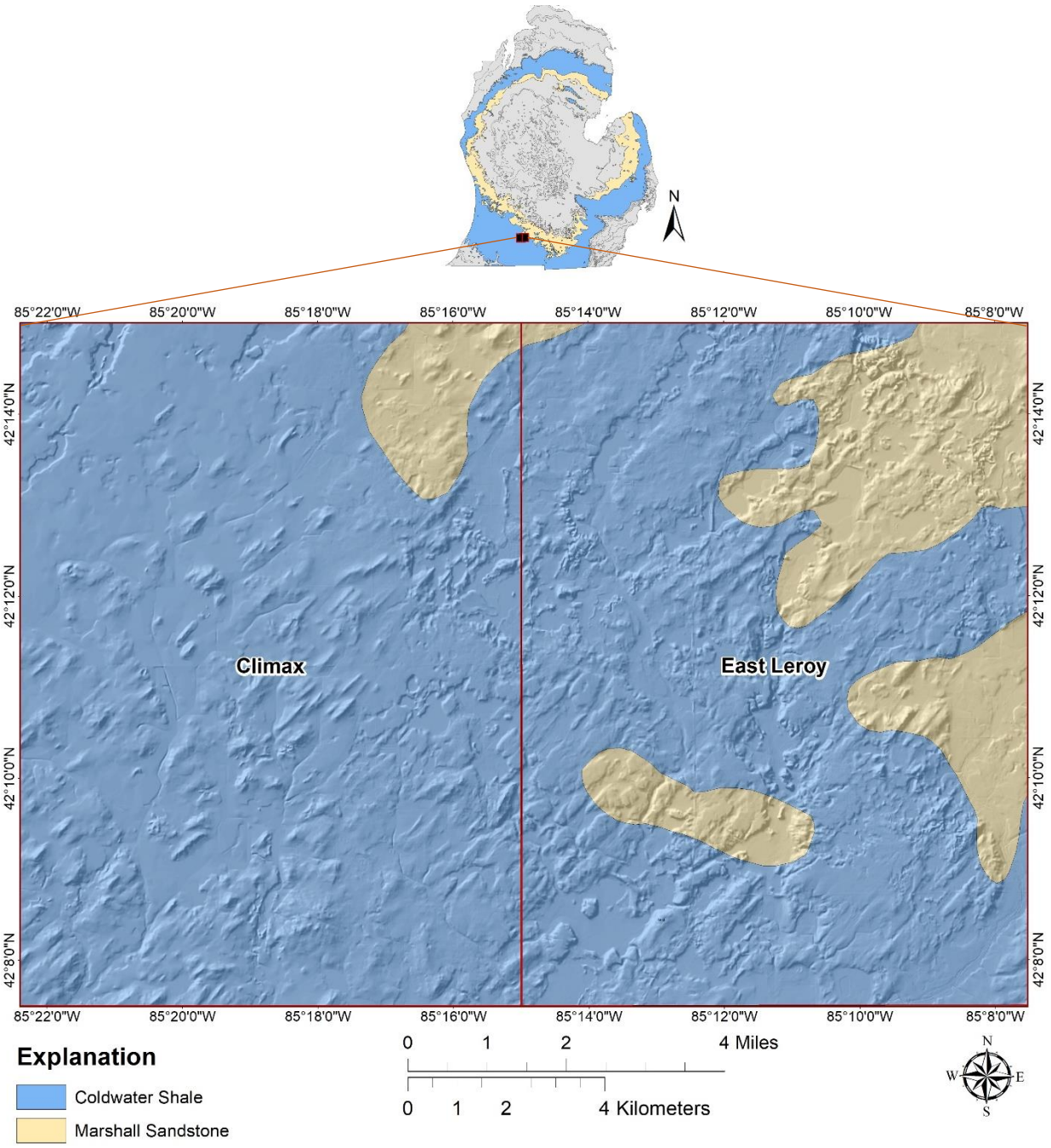

Figure 4. Bedrock units in the study area. The bedrock contacts of the Michigan Basin (Lower Peninsula) are displayed in the reference map at the top, with the extent of the Coldwater Shale and Marshall Sandstone highlighted. The study area map denotes unit subcrops according to the State of Michigan's open GIS database. Hillshade overlay is provided to display relative surface relief for context.

The Marshall Sandstone subcrops as a sandstone layer with variable coloration towards the northeast of the study area. It is generally light tan to grey colored and consists of an upper unit, the Napoleon Sandstone, that is coarse-grained with cross-beds and ripple marks, and a lower unit, the Marshall, that is a finer-grained sandstone (Milstein, 1987). The Marshall sandstone marks the onset of a transgression, but also contains minor siltstone layers and a fine clay matrix (Dorr and Eschman, 1970). Overall, the Marshall Sandstone is considered a potential aquifer with high hydraulic conductivities.

Glacial History

Millions of years after the formation of the Michigan Basin, the Laurentide Ice Sheet extended across what is now Canada and the northern United States and reached its maximum southward extent during the Pleistocene Epoch. Events shaping modern landscapes in Michigan consist of multiple glacial and interglacial intervals. The most recent glacial events to affect the Great Lakes Region are the Illinoian, Sangamon Interglacial, and Wisconsin episodes. Little evidence exists to conclude that Illinoian deposits occur within the study area, although some deposits do occur to the south in St. Joseph County (Gillespie et al., 2008; Kozlowski, 1999). During the Sangamon Interglacial episode, southwest Michigan was deglaciated, allowing for notable soil development. Most of the drift in the area is a result of the most recent glacial episode, the Wisconsin.

The Late Wisconsin glacial episode, specifically the Michigan subepisode (Hansel and Johnson, 1996), marked the overall retreat of the Laurentide Ice Sheet that created many of the features in the study area (Figure 5). Multiple lobe advances and retreats occurred during this overall retreat from about 24,000 to 18,000 years BP. After the Last Glacial Maximum (~24,000 yrs BP), the development and separation of major ice lobes became more pronounced. Three of

the Great Lake ice sheet lobes: Lake Michigan, Saginaw, and Huron-Erie, formed and last converged in southwestern Michigan (Figure 5a). The Saginaw Lobe was the last glacial lobe to affect the study area (Figure 5b). Over time, Quaternary glacial processes re-worked landscapes and deposited thick packages of poorly sorted glacial drift (Figure 5c). Tunnel valley networks formed beneath these ice lobes carried meltwater and sediment through channels carved into glacial debris or bedrock.

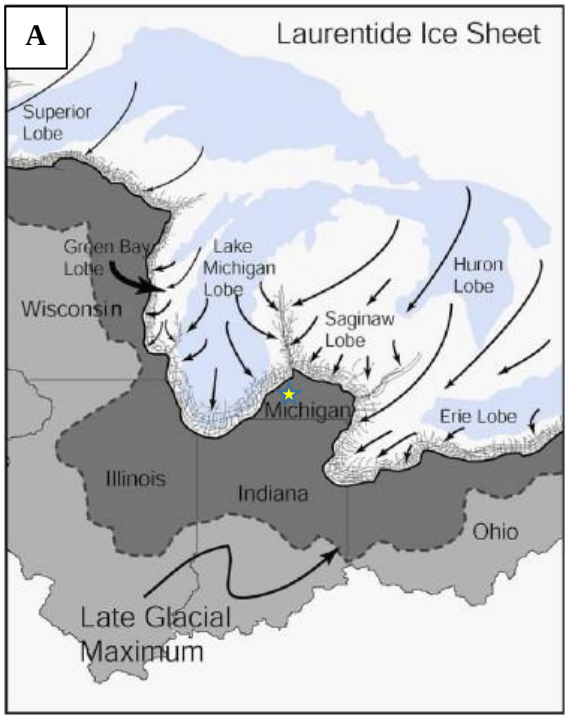

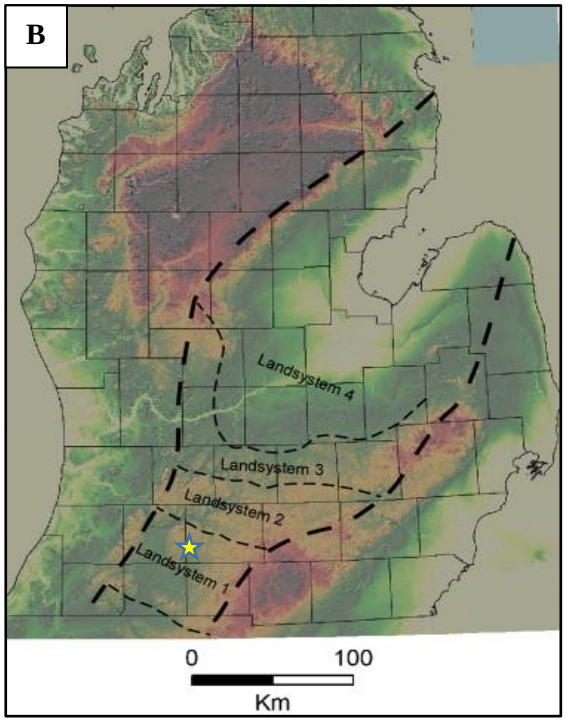

C

Era	Period	Epoch	Estimated Duration	Episode
Cenozoic	Quaternary	Pleistocene	79ka- 9.5ka	Wisconsin
			179ka - 79ka	Sangamon Interglacial
			300ka -125ka	Illinoian

Estimated Duration	Wisconsin Substage
79k-60ka	Ontario
60k-30ka	Athens-Elgrin
30k-11.5ka	Michigan

Estimated Dates	Relevant Glacial Events (Land System 1)
24ka	Saginaw Lobe LGM
20ka	Saginaw Lobe retreat
19ka	Huron-Erie Lobe advance into Saginaw Lobe territory; Saginaw Lobe forms Union Streamline Plain
18ka	Saginaw Lobe retreat into study area; meltwater flow into region, Tekonsha Margin Formation
17ka-15ka	Saginaw Lobe retreats north; possible stagnation or brief re-advance

Figure 5. A. Ice lobe positions in the Great Lakes region during the Late Wisconsin (Kehew et al., 2012). Study area denoted with a star. Note that the study area is in the path of the Saginaw Lobe; the Lake Michigan Lobe did not extend as far inland. **B.** Saginaw Lobe Landsystem classification (Kehew et al., 2012). Note that the study area is within Landsystem 1. **C.** Inferred glacial history time line of the study area. Data adapted from multiple sources including: Colgan et al., 2015; Backhaus, 2018; Gillespie, et al., 2008; Kozlowski, 1999.

The Saginaw Lobe area is a terrain rich in glacial sediments forming an array of erosional and depositional landforms. During asynchronous retreat, the Saginaw Lobe was smaller than the Lake Michigan Lobe to the west and the Huron-Erie Lobe to the east. This size difference, combined with factors such as: (1) meltwater drainage, (2) climate, and (3) drift thickness, caused the Saginaw Lobe to ablate and retreat at a much quicker pace than the surrounding lobes. Complex advances and retreats of the larger Lake Michigan and Huron-Erie Lobes allowed them to cover areas previously occupied by the Saginaw Lobe. This asynchronous movement reshaped the glacial stratigraphy in area and created overriding features and cross-cutting relationships among the deposits (Kehew et al., 1999). Further research on sediment grain characterization of deposits around southern Calhoun County supports multi-lobe interaction between the Saginaw and Huron-Erie Lobes (Erber, 2016).

Glacial-lake lobe movements cannot be attributed exclusively to climatic fluctuations and lobe thickness variations. Asynchronous ice stream behavior can also be explained by: (1) high basal fluid pressures within the Lake Michigan Lobe and Huron-Erie Lobe associated with underlying lake troughs (Patterson, 1997; Kehew et al., 2005; Jennings; 2006), (2) bedrock composition and topography (Kehew et al., 2012), or (3) potential ice stream surges (Fisher and Taylor, 2002; Fisher et al., 2003; Fisher et al., 2005). Regardless of the mechanism, such processes resulted in Saginaw Lobe deposits throughout central Michigan.

Wisconsin drift has several complex systems of moraines that mark the dynamic movements of several ice lobes. The Saginaw Lobe in southwestern Michigan experienced an overall retreat at the end of the Late Wisconsin glaciation and produced several notable moraine features. The Sturgis Moraine, an upland ridge associated with Saginaw Lobe stagnation or re-advance, occurs mostly in southern Michigan. This moraine is truncated by the moraine belt

from the Huron-Erie Lobe (Leverett & Taylor, 1915). The Tekonsha Margin, a drumlinized upland that was previously referred to as a moraine, lies northeast of the Sturgis Moraine and likely represents a brief pause during the Saginaw Lobe's retreat and interaction with the Lake Michigan Lobe. Continued lobe retreat to the north resulted in a broad, high-relief upland known as the Kalamazoo Moraine. Saginaw and Huron-Erie Lobe stagnation events during the Late Wisconsin were often followed by phases of increased meltwater drainage that eroded previous landforms and deposited outwash and glaciofluvial deposits through sluiceways or brief outburst flooding events (Kehew et al., 2012; Erber, 2016).

The study area is located amidst a drumlin field that covers much of the area between the Tekonsha Margin uplands and the Sturgis Moraine. Dodson (1985) provides additional evidence and description of this drumlinized region known as the Union Streamlined Plain. Although the origin of drumlins is subject to much debate (either by erosional or depositional processes), drumlin formation in this area is considered to be a result of basal sediment deformation under high pore pressures relating to the underlying bedrock contact between the Marshall Sandstone and Coldwater Shale (Kehew et al., 2017). The spindle shaped drumlins trend NE-SW, which parallels the Saginaw Lobe ice flow direction. These drumlins are mostly surrounded by ice-walled lake plain and proglacial or ice-contact outwash deposits.

Kehew et al. (2012; 2017) categorized deposits formed by the Saginaw Lobe into "Landsystems" to describe the glacial sediment-landform associations and glacial dynamics (refer to Figure 5). This study encompasses the area containing the Sturgis Moraine and the Union Streamlined Plain and would lie within "Landsystem 1". The boundary between Landsystem 1 and 2 generally follows the contact between the Coldwater Shale and the Marshall Sandstone because bedrock characteristics directly influenced lobe behavior. The southern, distal

end of Landsystem 1 is characterized by drumlins, hummocky terrain, coarse glaciofluvial fans, and outwash plains (Kehew et al., 2014; Kehew et al., 2017). During retreat, it is possible that the transition from permeable Marshall Sandstone to the impermeable Coldwater Shale resulted in basal pore pressure increase and deformed sediments into drumlin structures (Kehew et al., 2012).

Although glacial stratigraphy varies locally within Landsystem 1, efforts have been made to categorize sedimentary deposits. Kehew et al. (2017) identified several stratigraphic units in Landsystem 1. The lowermost basal unit is a sorted gravel immediately above the bedrock. This basal unit is overlain by a discontinuous hard and grey diamicton till with high clay content containing clastics (this unit may appear similar to weathered/ unconsolidated Coldwater Shale bedrock). Above the intermittent diacmicton is a sedimentary package of bedded sands and gravels with interfingering silt and clay layers. Next is typically an upper compact and sandy diamicton unit (this unit comprises the drumlin cores). All of these deposits are typically overlain by a variable upper unit containing postglacial fluvial and lacustrine sediments. The morphology, distribution, and relief of these surficial deposits are indicative of erosional and depositional landforms such as meltwater channels, eskers, kames, and outwash fans at ice margins.

Tunnel Valleys

Tunnel valleys are formed from subglacial meltwater flowing parallel to the ice flow direction. These tunnel valleys are terminated with outwash fans at their distal end (e.g., O'Cofaigh, 1996; Jørgensen and Sandersen 2006, Kehew et al., 2012). They form a large type of Nye channels, which are subglacial, downward-cutting, meltwater channels. Tunnel valleys are usually 5-15km long, with 2-30m of relief and an undulating and hummocky valley floor (Kehew et al., 2017). Differences in basal pore pressure, hydraulic gradients, meltwater supply,

and bed conditions all influence the development of these large erosional features. Occasionally, they form due to meltwater flow beneath an ice-marginal, underlying permafrost wedge and terminate at moraines (Hooke and Jennings, 2006). However, their dimensions and compositions vary, and their origins are often debated. Valley formation, for example, may be due to steady long-term erosion initiated by subglacial pressures (Kehew et al., 2012), or by significant outburst flooding (Fisher et al., 2005). Buried valleys observed in other regions (such as Denmark) contain sediments ranging from subglacial clay till to coarse meltwater deposits (Høyer et al., 2015). Similar valleys observed in Michigan often contain fining upward sedimentary sequences dominated by sands and gravels, denoting a loss of energy during deposition (Kehew et al., 2013). Such sediment infills originate from various materials including glacial till, glaciofluvial, and glaciolacustrine facies. Valleys are typically reused during multiple glaciations or are crosscut by modern stream networks, so sediments may be reworked and variable.

Because tunnel valleys are diverse depending on locality, they are typically interpreted using models of steady-state meltwater flow, catastrophic subglacial outburst flooding events, their proximity to ice margins, and cross-cutting relationships. Tunnel valleys in Landsystem 1 generally follow NE-SW trends and are parallel to ice lobe retreat and advance directions. Formation of tunnel valleys and other features in the area may be due to catastrophic subglacial sheet floods (Fisher et al., 2005), but this hypothesis lacks evidence in this region aside from some high energy coarse gravels underlying diamicton.

Tunnel valleys may not always erode into bedrock. Rather, the tunnel valley may only carve into glacial drift. Therefore, such valleys would be undetectable by some geophysical methods. The bedrock mapping project performed by Seiderman (2018), for example, resulted in

the discovery of a surficial tunnel valley in Kalamazoo Co. that did not incise into bedrock; however, two bedrock valleys in the same area exhibited little surface expression.

Linear features similar to tunnel valleys with N-S trends also occur and suggest an origin from previous glaciations or pre-glacial fluvial erosion (Kehew et al., 2017; Fisher et al., 2005; Rieck and Winters, 1979). One N-S trending surficial valley is present in this study area. Comparatively, other modern valleys in the Kalamazoo Co. and Calhoun Co. area may have been formed by buried ice melt-out or by glacial outburst flooding (Kehew and Kozlowski, 2007). These valleys often exhibit hummocky topography and are associated with present-day chain-of-lakes rather than large, smooth stream channels. However, Rieck and Winters (1979) interpreted that buried valleys that deviate from a N-S or NE-SW trend may have been created by a fluvially dominated, pre-glacial landscape.

Geophysical Background

Geophysical instrumentation is used in a wide variety of applications and is an important resource in both modern research and industry. Geophysical investigations can be used to detect buried bedrock valleys and other aspects of glaciated terrain that influence groundwater behavior. Buried tunnel valleys may be either filled with coarse material with high water yield potential or finer-grained sediments that act as groundwater barriers (Høyer et al., 2015). Characterizing a buried valley's shape, extent, and sediment fill composition presents a unique challenge to geophysical surveys. Methods involved in this small-scale study to detect buried valleys include: (1) passive seismic, (2) active seismic, (3) resistivity, and (4) gravity geophysics. Although gravity methods were not used in this work, results from previous gravity studies provide useful comparisons to datasets developed in this study.

Horizontal to Vertical Spectral Ratio (HVSR)

The passive seismic method was chosen as the primary method for this study because its simple and effective methodology. Similar studies previously conducted in Michigan successfully employed HVSR to asses bedrock topography (eg., Feldpausch, 2017; VanderMeer, 2018; Backhaus, 2018; Seiderman, 2018). Primary applications of the HVSR method involve: (1) the assessment of site amplification from earthquake waves (Nakamura, 1989), (2) determining surface layer resonance for engineering purposes, and (3) calculating soft sediment thickness overlying bedrock (Chandler and Lively, 2016). Although high frequency seismic waves occur during large magnitude earthquakes, smaller-scale natural and artificial sources such as ocean and lake waves, automobile operation, and vegetation swayed by wind continuously propagate into the subsurface and create low frequency micro-tremors that disturb surface layers (Nakamura, 1989).

HVSR data are typically obtained via a three component HVSR seismometer, such as a Tromino (MOHO Science and Technology) or similar instrument, that detects natural seismic waves moving through the subsurface. The exact source of these natural seismic noises is not well known, but peaks are mostly attributed to soft sediment resonance, Love waves, and maximum elliptical moments of Rayleigh waves (Chandler and Lively, 2014). Ground motion in three orthogonal directions (vertical, N-S, and E-W) is recorded by one vertical and two horizontal components. The horizontal components of the micro-tremors are amplified from shear wave interactions, with the most notable contribution from both surface Love waves and horizontally polarized shear waves (traveling in the near-vertical direction). The measured vertical component is from vertically polarized shear waves and Rayleigh waves. These shear wave velocities normally increase with depth due to material compaction, but shear wave

velocity changes may also be attributed to lithological variation and the transition from glacial sediment to bedrock. The frequency spectrum for each of the three components is calculated during post-processing. Once calculated, the E-W and N-S spectra are then combined, creating a single horizontal spectrum. The result of dividing the horizontal by the vertical spectrum, and plotting this ratio as a function of frequency, often shows a high amplitude peak (i.e., the resonance frequency).

When employing passive seismic for investigating bedrock depth (or glacial drift thickness), a strong 2:1 shear wave acoustic impedance contrast must be present between the two layers (Ibs-von Seht and Wolhenberg, 1999). The strength of an acoustic impedance contrast depends on the seismic velocities of the waves and the densities of the two layers. In an ideal two-layer case with clear subsurface resonance, the thickness of the soft upper unit is obtained through the following equation:

$$H = V_s/(4*f_o) \qquad \textbf{Equation 1}$$

where H= upper layer thickness, V_s=seismic shear velocity, and f_o= measured resonant frequency (Nakamura, 1989; Chandler and Lively, 2016). This equation presents two unknowns for an HVSR survey; data processing calculates a characteristic f_0 at a survey station, but the V_s at a site can be variable and is not known without prior experimentation. The H is typically the variable of interest to be resolved. Because determining a shear velocity for a large area is impractical, recordings are made at calibration stations where depths to bedrock (H) are known (typically from well records). These stations are then used to establish a power law regression curve unique to the study area.

Rather than relying on a single assumed shear velocity for an area to determine *H*, a more practical approach to calculate the thickness of the upper layer is created from field calibration stations by using the following equation:

$$H = af_0^{\,b} \qquad \textbf{Equation 2}$$

where *H*= sediment thickness (m), f_0= resonance frequency (Hz), and *a* and *b* are empirical fitting parameter constants (intercept and slope) determined from the regression line created from HVSR control points (Lane et al., 2008). Values *a* and *b* are obtained by plotting the depth to bedrock against the HVSR resonance peak (f_0) on bi-log-scales and creating a trendline through the calibration data points. The value for f_0 is obtained from the HVSR post-processing analysis by combining horizontal and vertical spectral data (as previously discussed). Optimal calibration stations are established at water wells or other types of boreholes that penetrate bedrock, as the well log generally provides a reliable known depth, *H*. Multiple calibration stations are needed due to regional variances in glacial drift thickness and composition that cause different V_s values.

Field problems relating to the passive seismic methodology, such as assuring adequate coupling, land accessibility, and the effects of unfavorable seismic sources sometimes necessitate the use of additional geophysical methods and several forms of error analysis to compare estimated bedrock depths. Additionally, bedrock deformation may violate the assumption of the previously described horizontal two-layer case and may result in inexact sediment thicknesses. Finally, shear wave acoustic impedance contrast at the basal contact between bedrock and the overlying glacial sediment must be 2:1 or greater to yield a quality resonance peak. Inherent errors associated with the Tromino are relatively small when evaluating general regional trends.

When combined with geophysical instrumentation datasets, results should better characterize the subsurface in areas of interest, such as at tunnel valleys.

HVSR Case Studies

Early use of passive seismic technology was used in Nakamura (1989) to assess site effects of microtremors and high frequency tremors from earthquakes to analyze engineering designs of structures in Japan. His work resulted in the "Nakamura method" of horizontal over vertical spectra to obtain a resonant frequency due to the presence of a soft surface layer. Since 1989, the technique has evolved into a method to estimate sediment thicknesses, as was done in Germany by Ibs-von Seht and Wolhenberg (1999). They were among the first to conduct broad HVSR surveys and to create a regional power law regression curve by using calibration stations. Their study produced cross sections of the western Lower Rhine Embayment and established the success of the HVSR method to map sediment thicknesses.

Others continued employing the Nakamura method, and guidelines were created by a commission of the European Union to provide recommendations and limitations of the HVSR technique in the form of the "Site EffectS assessment using AMbient Excitations" (SESAME, 2004). The SESAME project described how to obtain, process, and interpret HVSR survey data and provided nine processing criterion that an ideal ("usable") dataset should possess. Subsequent research investigating ambient noise properties has complied with these guiding principles. Nakamura (2008) eventually revisited his method by analyzing the significance of multiple resonant frequency "peaks" in the H/V spectra that may be representative of multiple layers of resonating sources. Ongoing HVSR research continues to reveal new applications for this relatively recent geophysical method.

Bedrock depth and regional glacial thickness investigations commonly employ passive seismic techniques in hydrogeologic studies. Lane et al. (2008) in one USGS study applied the HVSR method to survey areas in eastern Nebraska and Cape Cod, Massachusetts to determine bedrock surfaces for hydrogeological modelling. They concluded that shear wave acoustical impedance contrast heavily influences the quality of data. Although the Massachusetts readings were excellent as a result of denser bedrock composition, low acoustical impedance contrast between the weathered shale bedrock and the overlying sediment (combined with strong wind effects) in Nebraska often resulted in poor resolution and over-estimation of bedrock elevations.

The HVSR method has also been used in conjunction with other geophysical datasets. Another study in Slovenia used passive seismic paired with active seismic refraction profiles to map the Ljubljana Moor basin topography covered by Quaternary sediments (Gosar and Lenart, 2010). Gosar and Lenart's results were comparable using seismic refraction and HVSR data along the same profile. This finding strongly supporting the utilization of HVSR for modern bedrock mapping.

HVSR studies within the Great Lakes region of North America demonstrate the effectiveness of detecting buried valleys and features using the passive seismic technique in areas covered by glacial sediment. Chandler and Lively (2014) used the passive seismic method to map glacial drift thickness and delineate subsurface features (including bedrock valley morphologies) not effectively determined from well data in Minnesota and Wisconsin. They accomplished this project by developing their own regional calibration curves via control wells. Although rigid bedrock materials often provided them with strong, high amplitude spectral peaks, HVSR stations recordings on drift atop saproltic Cretaceous bedrock resulted in poor peaks. These data could falsely characterize the varying weathered bedrock zones or the complex

glacial stratigraphy, rather than clearly denote the top of bedrock. Chandler and Lively (2016) further analyzed peak quality by describing possible subsurface scenarios that create indistinct HVSR records, suggesting that even poor traces can be usable for bedrock mapping given adequate bedrock control. Additionally, Blake and Nash (2018) conducted an HVSR survey within the Botkins and New Knoxville quadrangles in Ohio to map bedrock for seismic hazard assessment. This survey revealed a deep and extensive buried bedrock valley, which provided insight on pre-glacial drainage systems in the Teays River valley. The study further used results of the subsurface mapping project to address earthquake hazard concerns. This analysis was done by correlating structure damage to thick packages of drift inferred from the valley geometry.

Recent glacial and bedrock mapping studies performed in Michigan utilizing the HVSR method yielded successful bedrock elevation maps. VanderMeer (2018) applied passive seismic and gravity methods in Pictured Rocks, MI to find extensive tunnel valley systems that run perpendicular to the southern shore of Lake Superior. Feldpausch (2017) also used HVSR along with gravity methods to produce bedrock topography maps and identify tunnel valley systems in the Dowling and Maple Grove quadrangles in Barry Co, MI (approximately 15 miles north of the Climax and East Leroy quadrangles – this study). Seiderman (2018) used HVSR to create a bedrock topography map of the Portage and Schoolcraft quadrangles in Kalamazoo Co., MI (approximately 15 miles west of this study area) and identified previously unknown pre-glacial valleys along with a Saginaw Lobe tunnel valley. Backhaus (2018) utilized HVSR to create a surficial map of the Bronson North and South quadrangles (located near the Michigan and Indiana border; approximately 15 miles south of the Climax- East Leroy area) and was able to identify an extensive buried cuesta.

Seismic Refraction/Reflection

Conventional near-surface seismic methods are commonly used to determine subsurface characteristics and layer depths. Energy from an active seismic source, such as explosives or hammer blows on a striker plate, are typically recorded as signals throughout a geophone spread. Seismic data from each geophone are digitally recorded to a multi-channel seismograph for processing. Subsurface P-wave reflectors and refractors are often indicators of changes in water saturation, lithology, or any other property that significantly alters the velocity of the P-wave through the subsurface. Analysis of S-waves can also be used to determine subsurface layering. Propagation of S-waves will not be affected by the top-of-water-saturation boundary, so generally only bedrock boundaries will be present. Furthermore, S-wave velocities can be directly determined for each layer. These S-wave velocities can then be utilized in HVSR calculations. Additional information on the well-established seismic methods and principles can be found in standard texts (e.g., Telford et al., 1990; Burger et al., 2006).

Small-scale seismic surveys have been determined to obtain similar results as HVSR studies (Gosar and Lenart, 2010). Therefore, applying conventional seismic methods with newer HVSR techniques can better characterize near-surface features and serve as an additional verification method for passive seismic data. Obiadazie (2011) utilized seismic surveys along with a gravity study to characterize buried tunnel valleys in Texas Township, MI. He concluded that seismic methods were generally more accurate for delineating buried valleys rather than gravity methods, especially when such valleys were carved into bedrock, rather than unconsolidated sediment (Obiadaize, 2011). However, locations allowing for long seismic spreads could not often be located. This common field problem could be addressed by utilizing HVSR techniques.

Resistivity

Data obtained from Vertical Electrical Soundings (VES) utilize the nature of electrical currents that travel through the subsurface from current electrodes to potential electrodes. Thus, glacial drift and bedrock may be distinguished by analyzing changes in the electrical properties of near-surface lithologies. Conventional resistivity methods and principles are discussed in texts such as Telford et al. (1990) and Burger et al. (2006). Electrical resistivity was utilized as an alternative to seismic interpretations when comparing HVSR data, as bedrock can be electrically detectable given adequate field conditions.

Previous studies describe the strengths and limitations of the resistivity method on glacial sediments. Resistivity methods are employed for unconsolidated sediment identification, river terrace deposit mapping, shallow aquifers and glacial groundwater characterization, and glacial effects on peatlands (Pellicer and Gibson, 2011). The Illinois Geological Survey (IGS) performed a study utilizing resistivity in glacial terrain and concluded that thin drift packages (less than 10 ft) were unrecognizable (McGinnis and Kempton, 1961). The IGS study also noted that at locations where drift composition was electrically similar to bedrock, sediment thicknesses were unable to be determined. Resistivity proved useful when other methods such as active seismic were inadequate at determining bedrock depths and sediment characterization. However, newer studies from the Illinois Geologic Survey utilizing both large resistivity sounding 2-D lines and seismic shear wave reflection analyses effectively characterized drift deposits in northeastern Illinois (Thomason et al., 2018).

Additional studies utilized vertical electrical soundings and combined datasets to characterize hydrogeological units in buried valleys. Kosinski and Kelly (1981) observed that changes in resistivity allowed for the interpretation of bedrock contacts, and bedrock depths were

inferred by correlating to nearby boreholes. Smith (1974) used resistivity in conjunction with thermal probes to delineate buried valleys in Morning Sun, Ohio; although the thermal probe survey failed to distinguish temperature trends indicative of bedrock valleys, the resistivity survey detected a buried valley network beneath glacial drift ranging from 90 to over 150 feet in thickness. Unfortunately, resistivity penetration depths may be variable in the proposed field area due to Michigan's heterogenous drift composition. The applicability of this method depends on the ability of the injected current to extend to solid bedrock, but this can vary widely depending on the medium's electrical properties and nearby conductors. Electrical resistivity produces the best results if a shallow bedrock layer is undeformed and does not have similar resistivity properties as the overlying deposits. Despite potential field complications, this method was used in this study to provide alternative subsurface modelling to compare with passive and active seismic results

CHAPTER III

METHODS

Passive Seismic

Field Survey

The HVSR survey was conducted using a Tromino Zero 3G digital tromograph made in Italy by MOHO Science and Technologies (Figure 6). The unit was equipped with three spikes that securely coupled the instrument to the ground surface. When choosing a recording station location, care was taken to avoid persistent ambient noise sources such as telephone poles swaying in the wind, flowing streams, active factories, and operating farm tractors and irrigation systems. These obstacles typically created constant, interfering surface waves that overpowered or otherwise interfered with the resonant frequency at the site. The ground surface would first be cleared of vegetation or debris and was then compacted to promote adequate ground coupling with the instrument. Ground packing was critical for proper ground coupling on coarser surfaces to improve the quality of the record. The Tromino unit was then oriented north, levelled via the built-in circular level, and firmly pressed into the earth. If the instrument felt too loose or inadequately coupled with the earth, the instrument planting process was repeated. Once the instrument was successfully coupled to the ground, the Tromino was then activated. Then, the trace “partition” or file number was recorded, and the unit was set to acquire a signal. The Tromino unit had a 15-second lag period that allowed the operator to move away from the station and avoid unwanted noise on the record.

Figure 6. Left: Tromino equipment case. Materials include: spare AA batteries, alternative hard surface spikes, USB connection cable to download field data to a computer, compass to orient the instrument north, brush to clean coupling spikes of debris, and the Tromino Zero 3G instrument (Serial no. TZ3-0032/01-15). **Right:** The "planted" Tromino unit prepared to make a station recording.

The instrument was set at every station to acquire signals at full gain with a sampling rate of 128 Hz. This setting applied no filtering to the signal and captured traces within a frequency range of 0.5 – 64 Hz (i.e., the minimum sampling rate that will not produce errors in the record; the Nyquist frequency). Because natural recorded signals are discontinuous, the entire recording length must be long enough to register 200 cycles of the resonant frequency (SESAME, 2004). Normally, a 16-minute record satisfies this criterion in regions of thin drift and was deemed appropriate based on the area's estimated drift thickness from water well records (10- 250 feet). Regions of thicker drift generally require a longer recording time. Latitude and longitude coordinates were recorded at each station by using GPS cell phone applications and were later

verified when projected in GIS. Observations were noted concerning traffic density and proximity to the instrument, distance to nearby structures, and weather conditions. When wind gusts were noticeably strong (>15 mph), adverse effects were reduced using by a protective cover, such as an inverted, weighted plastic tote. Even with such precautions, it was apparent during post-processing that wind had compromised several station recordings, which warranted conducting another 16-minute recording to replace the affected reading.

HVSR data points were gathered at roughly ½ mile intervals, primarily along "safe" roadsides with adequate ground exposure for instrument coupling. Other survey locations included public lands such as cemeteries and parking lots, and on private property when given permission. Denser sampling spacing was performed in several locations to improve lateral resolution of bedrock features. The Tromino stores a limited number of traces (50 partitions or files for this survey unit), so data was transferred to a computer at the end of the field day to be processed in Grilla software.

HVSR Data Processing

Stored HVSR traces were imported and processed in Grilla software, a program designed to analyze and display graphs of spectral data (MOHO Science and Technology). Data were organized by date, county, and station number. Spectral ratios were analyzed in 15 to 20 second processing windows which allowed for two enhancements. The first was the ability to edit (remove) selected windows containing unwanted noise bursts (such as passing cars). The second was then to enable Grilla to do basic statistical analyses of the results of the remaining 40 or so usable processing windows (e.g. the standard deviation of the resonant peak frequency -along the frequency axis, and the standard deviations of the spectral ratio amplitudes - along the vertical

axis). The goal of this flexibility in processing is to calculate a resonant peak with maximum amplitude and minimum standard deviation. According to SESAME (2004) guidelines, the processing window width selection should be chosen with respect to the expected resonant frequency; at least 10 cycles of the resonant frequency should be recorded within the window. For example, a 1 Hz resonance frequency would have a period of 1 second would require a minimum 10-second window. A larger than minimal processing window was always chosen to account for the discontinuous nature of the measured signals. It was determined that a 15-20 second processing window was optimal, whereas longer windows often included parts of noise-bursts that resulted in fewer usable windows and hence less reliable statistics. However, choosing different window sizes sometimes resulted in a different f_0 pick for the same recording. Processing windows were increased up to 20 seconds if the 15 second window produced lower SESAME scores and/or weaker peak amplitudes with high standard deviations.

Another aspect of HVSR processing involves data filtering. Frequency domain data was filtered via triangular window smoothing of 10% but was adjusted to as low as 5% when peaks were weak, broad, or poorly defined. Applying a lower smoothing factor often separated individual peaks that may have been previously smoothed into one broad peak. Very low (approx. 0.5 Hz and lower) and very high (approx. 60 Hz and higher) frequencies from unwanted ambient noises not related to the peak frequency could be ignored by manually narrowing the frequency range to be processed. The default processing range was between 0.1-64 Hz.

After processing the spectral data, a computer report was generated and assessed using SESAME criteria (2004). The H/V spectral ratio graph, resonant frequency and standard deviation, H/V time history, H/V directionality, SESAME score, and other peak characteristics were included in each station report. These data were then manually interpreted, described, and

organized into an Excel spreadsheet along with other station parameters. Ideal cases displayed only one maximum amplitude spectral H/V peak. This peak should correspond to a strong resonant peak amplitude, indicating a high impedance contrast at the glacial drift-bedrock boundary (Figure 7A). The H/V time history displayed amplitudes (by color) and frequency throughout the time of the recording; this graphic can then be edited to remove windows containing unwanted noise outside of the frequency of interest (Figure 7B- refer to previous discussion). Good quality, high-amplitude resonance signals (generally greater than 3.0) should also exhibit uniform directionality of ground motion vs azimuth, as expected from a continuous, relatively planar subsurface that is being excited by multiple distant sources (Figure 7C). A clear contrast between bedrock and drift can be further detected in the single component spectra, where the horizontal E-W and N-S components should be aligned while the vertical component deviates towards a lower magnitude, forming an "eye" shape (Figure 7D). Traces with these characteristics were considered high quality and usable for drift thickness and bedrock topography estimates. These traces typically yielded satisfactory SESAME scores (Figure 8).

Conversely, traces exhibiting multiple, compound, or subdued peaks required additional caution when processing and were likely influenced by a complex subsurface and/or a low bedrock-acoustic impedance contrast (Figures 9 and 10). These "peak frequencies" were further analyzed by considering monochromatic sources on the H/V azimuthal diagram. Unidirectional noise sources at a particular resonance frequency are indicated by a focused "bull's eye," suggesting a localized source (i.e., not multiple distant sources). Multiple peaks on the spectrum can occur from anthropogenic sources or complex subsurface conditions, such as the upper surface of a compact till.

Bedrock was sometimes identified by manually choosing a different peak that was not chosen by Grilla for the f_0; Grilla only analyzes the highest amplitude peak. This manual process was performed on records that had multiple peaks with variously high amplitudes. Also, traces denoted as "poor" were still manually identified, and could be determined to be conditionally usable if a peak on the frequency spectra produced a bedrock depth that agreed with nearby bedrock wells and either received a high SESAME score (generally 7-9 out of 9) or exhibited uniform H/V directionality. Previous studies also utilized "poor" data caused from saprolitic bedrock surfaces, provided that the station was obtained in close proximity of nearby bedrock control wells to verify picks (Chandler and Lively, 2016). Every potential data point was scrutinized and compared to nearby water well logs when considering usable peaks and their applicability in map creation.

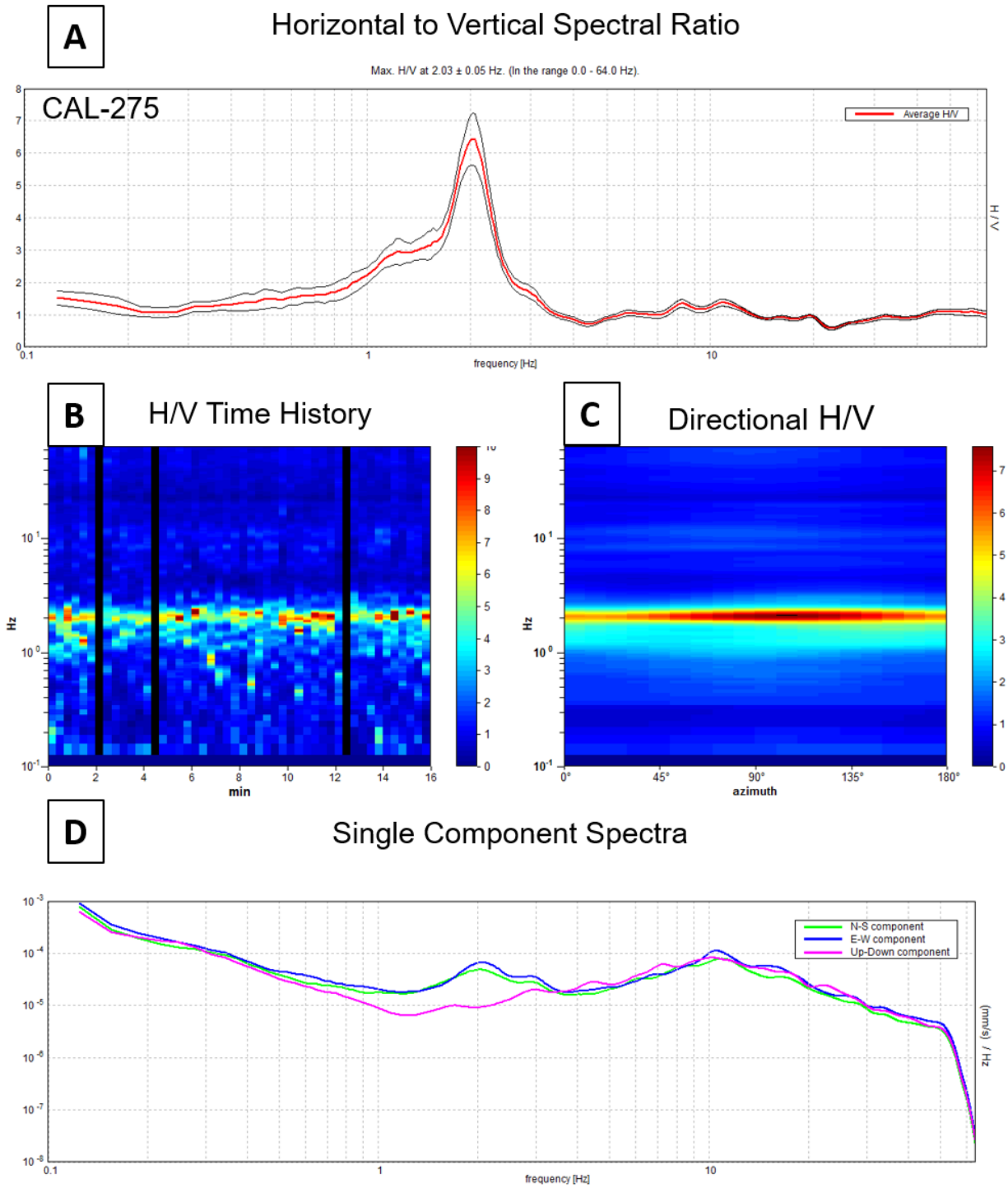

Figure 7. Quality passive seismic data example (CAL-275). **A.** H/V components are averaged (red line) with variable standard deviation ranges above and below. **B.** Processing windows of 20 seconds (48 windows for the 16-minute reading). Note that three windows were removed during processing (black lines) **C.** Strong and azimuthally-continuous ground particle motion. Note a slight bias at about 100°. **D.** Strong spectra with exaggerated "eye" shape that coincides with f_0 (2.03Hz).

Max. H/V at 2.03 ± 0.05 Hz (in the range 0.0 - 64.0 Hz).

Criteria for a reliable H/V curve [All 3 should be fulfilled]			
$f_0 > 10 / L_W$	2.03 > 0.50	OK	
$n_c(f_0) > 200$	1828.1 > 200	OK	
$\sigma_A(f) < 2$ for $0.5f_0 < f < 2f_0$ if $f_0 > 0.5$Hz $\sigma_A(f) < 3$ for $0.5f_0 < f < 2f_0$ if $f_0 < 0.5$Hz	Exceeded 0 out of 98 times	OK	
Criteria for a clear H/V peak [At least 5 out of 6 should be fulfilled]			
Exists f^- in $[f_0/4, f_0] \mid A_{H/V}(f^-) < A_0 / 2$	1.531 Hz	OK	
Exists f^+ in $[f_0, 4f_0] \mid A_{H/V}(f^+) < A_0 / 2$	2.406 Hz	OK	
$A_0 > 2$	6.44 > 2	OK	
$f_{peak}[A_{H/V}(f) \pm \sigma_A(f)] = f_0 \pm 5\%$	|0.02554| < 0.05	OK	
$\sigma_f < \varepsilon(f_0)$	0.05187 < 0.10156	OK	
$\sigma_A(f_0) < \theta(f_0)$	0.8109 < 1.58	OK	

L_W	window length
n_W	number of windows used in the analysis
$n_c = L_W n_W f_0$	number of significant cycles
f	current frequency
f_0	H/V peak frequency
σ_f	standard deviation of H/V peak frequency
$\varepsilon(f_0)$	threshold value for the stability condition $\sigma_f < \varepsilon(f_0)$
A_0	H/V peak amplitude at frequency f_0
$A_{H/V}(f)$	H/V curve amplitude at frequency f
f^-	frequency between $f_0/4$ and f_0 for which $A_{H/V}(f^-) < A_0/2$
f^+	frequency between f_0 and $4f_0$ for which $A_{H/V}(f^+) < A_0/2$
$\sigma_A(f)$	standard deviation of $A_{H/V}(f)$, $\sigma_A(f)$ is the factor by which the mean $A_{H/V}(f)$ curve should be multiplied or divided
$\sigma_{logH/V}(f)$	standard deviation of log $A_{H/V}(f)$ curve
$\theta(f_0)$	threshold value for the stability condition $\sigma_A(f) < \theta(f_0)$

Threshold values for σ_f and $\sigma_A(f_0)$					
Freq. range [Hz]	< 0.2	0.2 – 0.5	0.5 – 1.0	1.0 – 2.0	> 2.0
$\varepsilon(f_0)$ [Hz]	0.25 f_0	0.2 f_0	0.15 f_0	0.10 f_0	0.05 f_0
$\theta(f_0)$ for $\sigma_A(f_0)$	3.0	2.5	2.0	1.78	1.58
log $\theta(f_0)$ for $\sigma_{logH/V}(f_0)$	0.48	0.40	0.30	0.25	0.20

Figure 8. Example of a quality SESAME report (CAL-275; Figure 7). See SESAME, 2004 for additional explanation of values and variables.

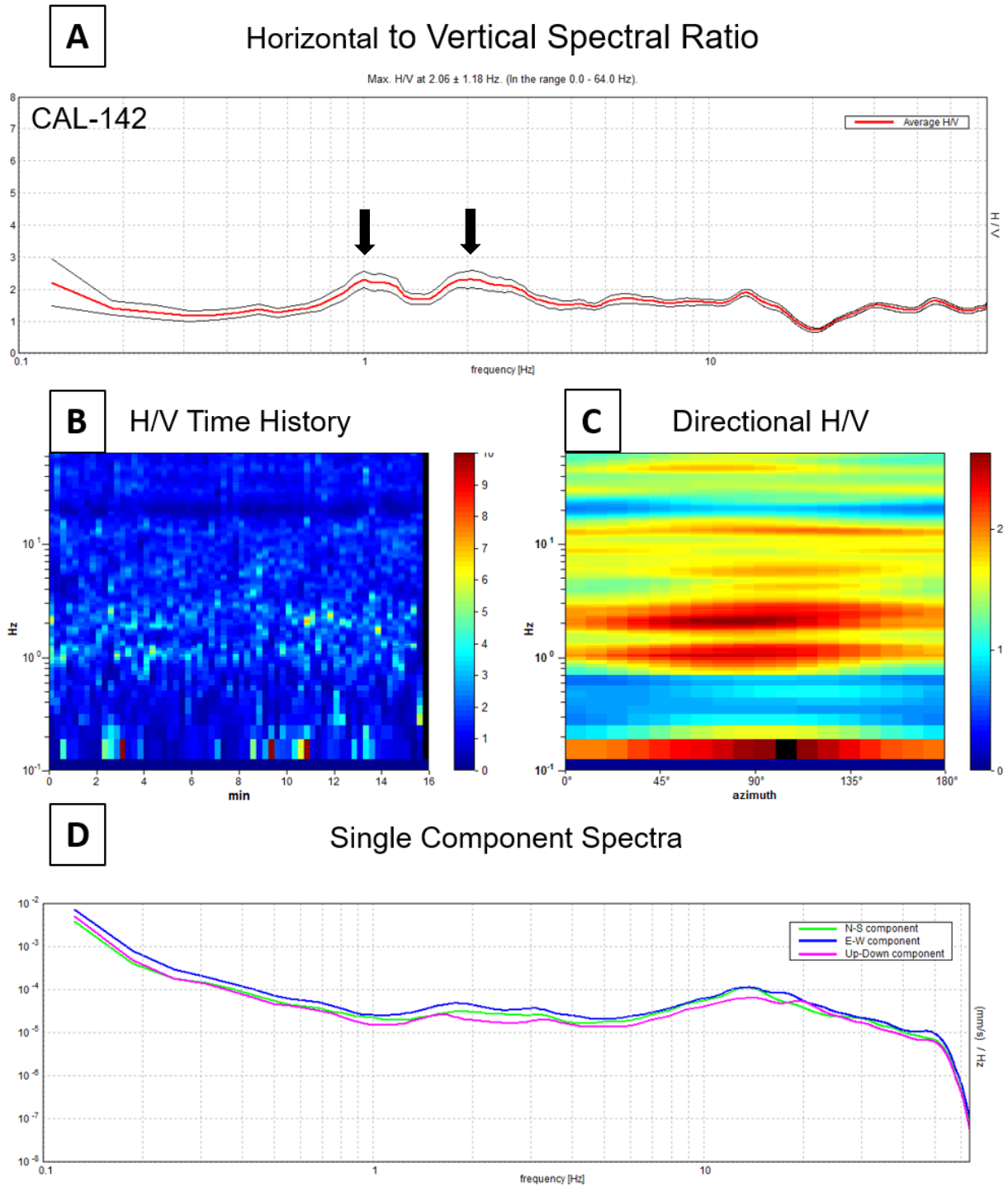

Figure 9. Example of poor quality HVSR data (CAL-142). **A.** Two similar, low amplitude peaks do not provide a clear indication of bedrock contact (arrows). Note the high standard deviation of the chosen peak. **B.** No dominant resonance frequency is observed, and H/V results are not strong or consistent over time (15 second processing window; 64 total windows). **C.** Variable directional signals were likely local and originated from multiple sources. **D.** Non-characteristic spectra lacking a strong "eye" at peak frequencies.

Criteria for a reliable H/V curve [All 3 should be fulfilled]			
$f_0 > 10 / L_w$	2.06 > 0.67	OK	
$n_c(f_0) > 200$	1949.1 > 200	OK	
$\sigma_A(f) < 2$ for $0.5f_0 < f < 2f_0$ if $f_0 > 0.5$Hz $\sigma_A(f) < 3$ for $0.5f_0 < f < 2f_0$ if $f_0 < 0.5$Hz	Exceeded 0 out of 50 times	OK	
Criteria for a clear H/V peak [At least 5 out of 6 should be fulfilled]			
Exists f^- in $[f_0/4, f_0]$ | $A_{H/V}(f^-) < A_0 / 2$			NO
Exists f^+ in $[f_0, 4f_0]$ | $A_{H/V}(f^+) < A_0 / 2$			NO
$A_0 > 2$	2.31 > 2	OK	
$f_{peak}[A_{H/V}(f) \pm \sigma_A(f)] = f_0 \pm 5\%$	|0.56989| < 0.05		NO
$\sigma_f < \varepsilon(f_0)$	1.1754 < 0.10313		NO
$\sigma_A(f_0) < \theta(f_0)$	0.2774 < 1.58	OK	

L_w	window length
n_w	number of windows used in the analysis
$n_c = L_w n_w f_0$	number of significant cycles
f	current frequency
f_0	H/V peak frequency
σ_f	standard deviation of H/V peak frequency
$\varepsilon(f_0)$	threshold value for the stability condition $\sigma_f < \varepsilon(f_0)$
A_0	H/V peak amplitude at frequency f_0
$A_{H/V}(f)$	H/V curve amplitude at frequency f
f^-	frequency between $f_0/4$ and f_0 for which $A_{H/V}(f^-) < A_0/2$
f^+	frequency between f_0 and $4f_0$ for which $A_{H/V}(f^+) < A_0/2$
$\sigma_A(f)$	standard deviation of $A_{H/V}(f)$, $\sigma_A(f)$ is the factor by which the mean $A_{H/V}(f)$ curve should be multiplied or divided
$\sigma_{logH/V}(f)$	standard deviation of log $A_{H/V}(f)$ curve
$\theta(f_0)$	threshold value for the stability condition $\sigma_A(f) < \theta(f_0)$

Threshold values for σ_f and $\sigma_A(f_0)$					
Freq. range [Hz]	< 0.2	0.2 – 0.5	0.5 – 1.0	1.0 – 2.0	> 2.0
$\varepsilon(f_0)$ [Hz]	0.25 f_0	0.2 f_0	0.15 f_0	0.10 f_0	0.05 f_0
$\theta(f_0)$ for $\sigma_A(f_0)$	3.0	2.5	2.0	1.78	1.58
log $\theta(f_0)$ for $\sigma_{logH/V}(f_0)$	0.48	0.40	0.30	0.25	0.20

Figure 10. Example of a poor SESAME report (CAL-142; Figure 9). Note that only 5 of the 9 SESAME criteria were met. This reading was not considered usable for determining drift thickness without the aid of independent bedrock control.

Repeatability and verification of HVSR station data included the collection of repeat (different time and different day) and concurrent (two instrument) stations. The locations of repeated stations obtained towards the end of the field season required some adjustment due to overgrowth and landscape changes, but these readings were collected within 15 feet of the original stations. Concurrent stations were collected simultaneously with two Tromino instruments controlled by two different field operators, but also within 15 feet of each other. Repeat and concurrent stations were processed with the same window size as the original station for consistency. Repeated stations, in some cases, yielded slightly better results and was reprocessed independently of the original station to produce more reliable depth to bedrock estimates for the final bedrock topography and drift thickness maps.

The development of a calibration curve required the collection of HVSR readings at sites of known depth to bedrock. Several HVSR stations were recorded near locations of bedrock-penetrating water wells (as documented by the State of Michigan open GIS - Wellogic database). Additionally, HVSR readings were performed at the sites of three previous rotosonic test borings and the sites of the two mud rotary borings drilled for this project. The calibration curve includes results from 18 quality HVSR recordings that were taken at sites with a variety of drift thicknesses, therefore covering an extensive range of frequencies. This calibration curve technique is required when there is a wide range of drift thicknesses, as the use of a constant average *Vs* cannot be justified due to the greater compaction of thicker drift.

Geographic Information Systems

Map creation involved the assimilation of GIS data files available on GIS open data available for the state of Michigan, such as shapefiles for streams, lakes, water wells, roads, and feature boundaries. A digital elevation model (DEM) was created from LiDAR data (10mx10m spatial resolution) for Calhoun and Kalamazoo counties to generate elevation values in the form of a raster file. Elevation values were then extracted for every HVSR station and water well location from the DEM file in ArcMap. Although accepting well log descriptions can be a subjective process, outliers were identified and omitted based on obvious irregularities in preliminary bedrock surface interpolation methods in ArcMap. Subtracting the calculated bedrock depth (glacial drift thickness) estimates from the elevation values provided the bedrock elevation used to create a bedrock topography map.

Bedrock topography and drift thickness raster surfaces were created in ArcMap by applying a kriging interpolation to the project data imported from Excel. Kriging interpolation was most the appropriate method for the datasets due to the irregular nature of the sampling scheme and the capability of the algorithm to identify spatially directional features (such as valleys). Ordinary kriging provided the lowest RMS prediction error (approximately 9.75) for both bedrock elevation and drift thickness raster surfaces. Other interpolation methods created more distorted models with higher RMS errors. For example, inverse distance weighing interpolation appeared to overestimate bedrock depths by emphasizing extreme elevation values, and natural neighbor algorithms are reported to underestimate bedrock depths (Kearsey, et al., 2018). Approximately five hundred thirty water wells that penetrated bedrock, in addition to interpreted HVSR data, contributed to the final the interpolation map of the two quadrangles and surrounding area. Furthermore, only 22 of the available 46 oil and gas well logs proved usable

for constructing the maps due to dubious or missing bottom-of-glacial contact information. Five bedrock test borings were also added to the dataset: three rotosonic borings from previous mapping efforts (Kehew and Esch, 2013; 2014), and the two mud rotary borings performed for this project.

Once a topographic map using the "true" bedrock depths was created, an additional 200 (approximate) drift wells were used to "push down" the bedrock topography interpolation surface around these wells (negative values) (John Esch, personal communication; Gao et al., 2006). Although these drift wells did not penetrate bedrock, their total depths were deeper than the bedrock contact inferred from the raster interpolation. ArcMap identified these wells by using a definition query to search for points that yielded a negative value when subtracting the bedrock elevation from the reported total depth of the well (elevation at bottom of hole). The inclusion of these data points created more accurate bedrock topography and drift thickness maps with the available log data.

The generation of cross-sections utilized an older version of ArcMap (10.2) and the Xacto cross-section tool (ver. 10) created by Jennifer Carrell of the Illinois Geological Survey. Cross-sections were constructed using surface elevation (DEM) and HVSR and well log bedrock topography data. After a line segment was created over the area of interest, the program gathered data from raster files (bedrock and surface elevations) to replicate the model in a two-dimensional vertical slice. Vertical exaggeration was defined as 30x to accentuate subtle topographic relief. Cross-sections were created to compare: (1) HVSR data to gravity profiles (Farnsworth, 1980), (2) HVSR results to seismic 2D seismic data provided by Wolverine Gas and Oil, and (3) mud rotary borings performed for this project with the interpolated bedrock topography. When comparing mud rotary borings, water well logs with lithologic boundary

depths were also plotted within a chosen radius of 300m to provide approximate subsurface units as described in driller reports. Lithology units were then lumped into broad categories (sand and gravel, silt and clay, bedrock, etc.) to accommodate the diverse (and sometimes contradictory) descriptions in the driller's logs.

Resistivity

Field Survey

Schlumberger Vertical Electrical Resistivity Soundings (VES) performed for this project were conducted on a fairly dry-ground surfaces oriented approximately N-S (Figure 11). The Iris Syscal R2 unit used for the surveys was positioned near the midpoint, and 4 wire-reel electrodes were laid out along the sounding line. Contact resistance was first checked at each electrode to ensure adequate ground contact. Electrode line spacings were expanded along the sounding line according to standard Schlumberger sounding MN and AB spacings (6 readings per decade of AB/2 spacings, with uniform expansion on a log scale). The minimum AB/2 spacing was 1m with a maximum spacing of 100m, whereas the minimum MN spacing was 0.3m with a maximum spacing of 10m. At least 10 current pulses were averaged before registering the reading. The current, voltage, SP, and electrode spacings were recorded. Expansion to the next electrode spacing was then completed. The transmitter voltage was increased to provide greater current as the AB separation increased. The Syscal R2 unit stored readings for each recording station; however, data was also recorded manually on field sheets.

Processing

The 1X1D Interpex computer software was used to plot the VES field data and do inversion. Apparent resistivity vs. current electrode spacing was inverted to provide a possible

solution (or inverse model) of layer thickness and resistivities. The number of layers and the starting resistivities and thicknesses for each layer were then adjusted (i.e., “fixed”) with the goal of obtaining a geologically reasonable model yielding a low RMS or fixing error between the field data and the forward model calculated form the inverse model.

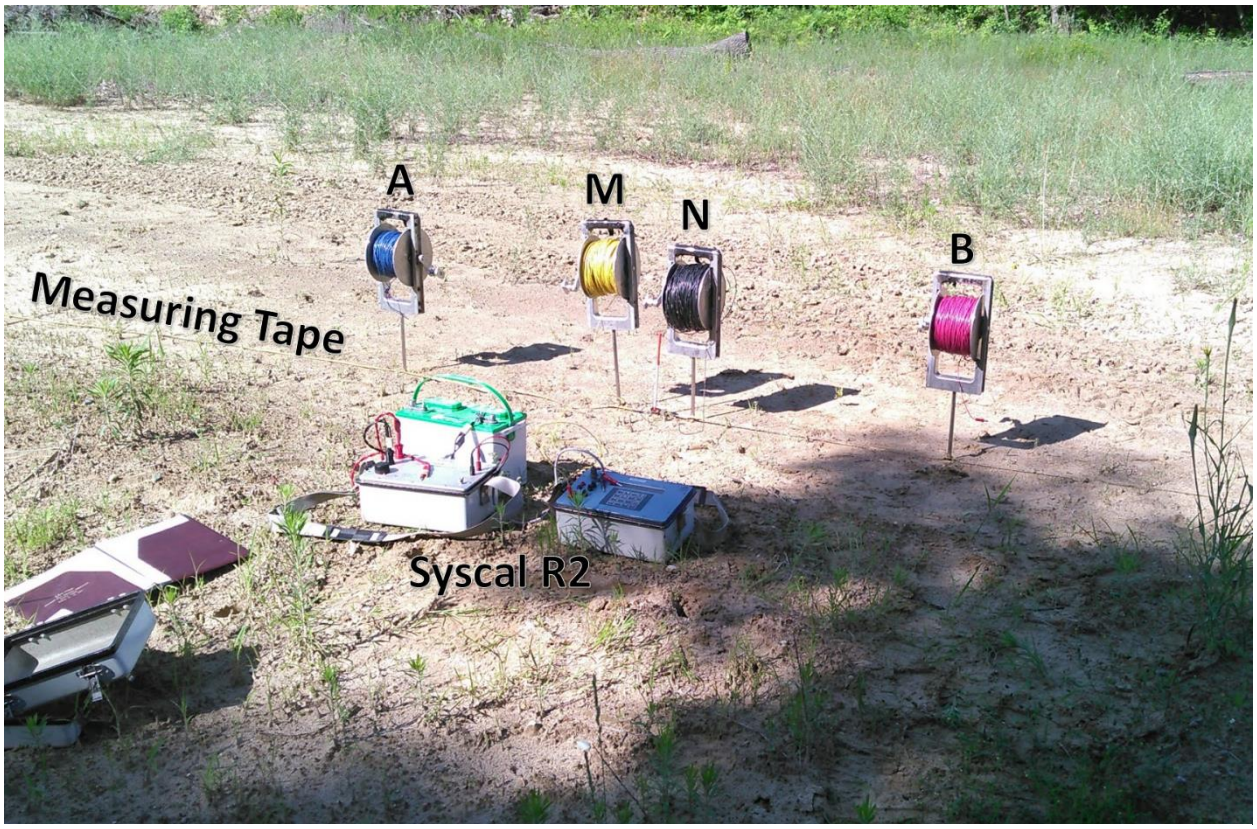

Figure 11. Field photo of the electrical resistivity VES setup using the Schlumberger Array along the sounding line. The Syscal R2 unit was powered by a 12V car battery. Fiberglass stakes held the measuring tapes in place at the midpoint. Current electrodes (A and B) and potential electrodes (M and N) are positioned to obtain the first reading for the Schlumberger setup; A and B are positioned 2 meters apart, whereas M and N are positioned 0.30 meters apart.

Active Seismic

Field Survey

Seismic reflection/ refraction surveys were performed at several accessible locations within or near surficial valleys to: (1) provide bedrock control for HVSR readings, (2) attempt to detect bedrock geometry, and (3) obtain independent site-specific shear wave velocity (*Vs*) (Figure 12). Three seismic profiles (CAL01-SEIS1, CAL02-SEIS2, CAL03-SEIS3) were performed with twenty-four vertical 40 Hz geophones connected to a Geometrics RX-24 Strataview seismograph unit powered by a 12V battery. Geophones were placed every 4m, which created a 96m spread oriented along an approximate N-S trend. Each survey line was performed along a near- level surface so that elevational corrections were not necessary during processing.

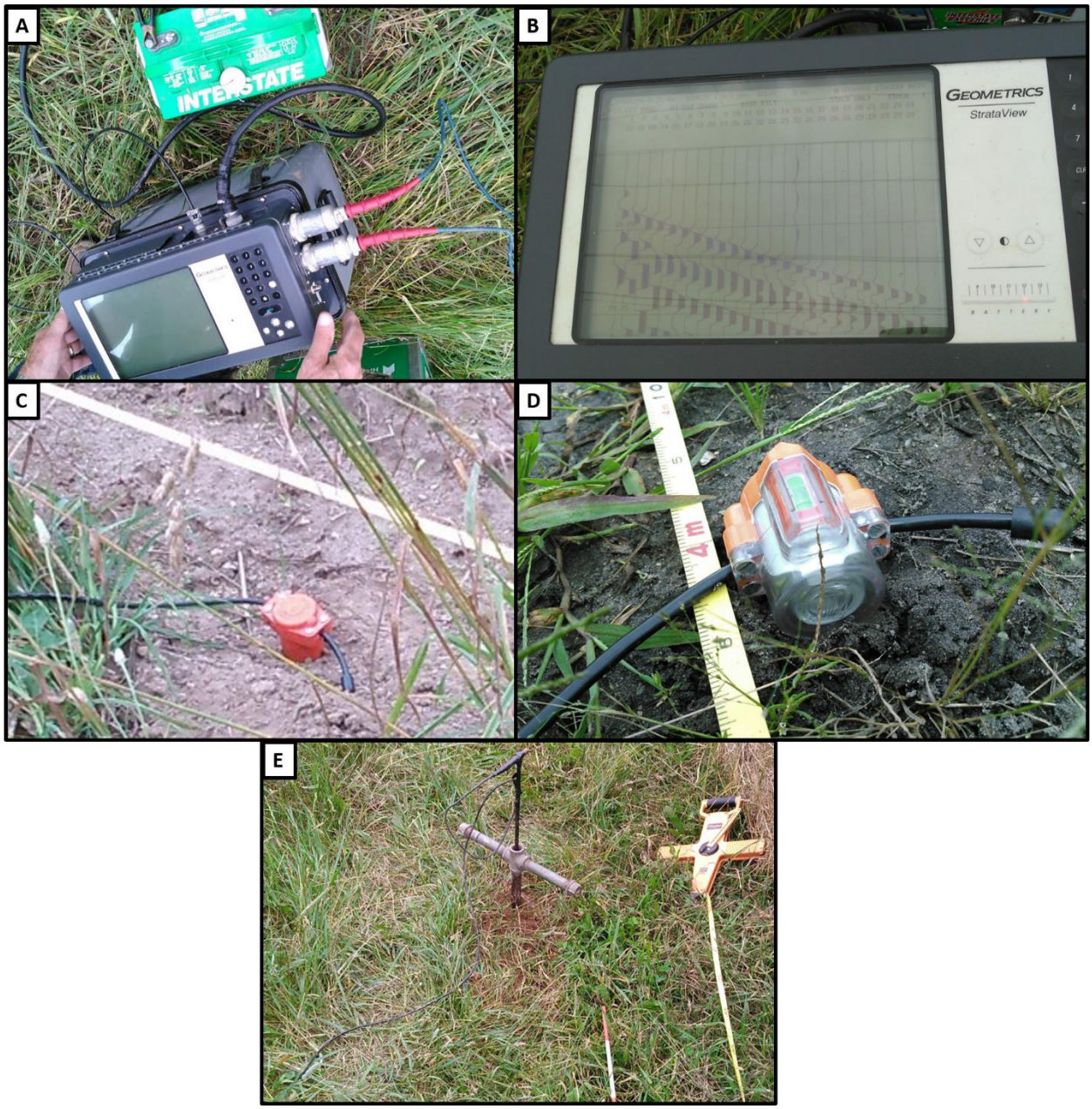

Figure 12. Photos of near-surface active seismic equipment in the field. **A.** The Geometrics Strataview seismograph unit with power, spread, and shotpoint cables attached. **B.** Example of a near-shot raw record. Early time data for each geophone is displayed; the first arrival of the direct P-wave is followed by signals of shear, reflected, refracted, and surface waves. **C.** Vertical geophone attached to the spread cable. **D.** Horizontal geophone leveled and planted radially along the spread line. **E.** Betsy seisgun buried to a depth of approximately 1m with firing pin and impact switch attached to the shot cable.

A sledgehammer & striker plate and gunpowder explosives (Betsy Seisgun) were used as seismic sources. After setting up the geophone spread, the shotpoint extension cable was unwound and attached to the instrument creating the seismic source (i.e., sledge hammer or Seisgun firing pin rod) at the desired shotpoint. The two spread cables and the shotpoint extension cable were then attached to the Geometrics Strataview seismograph positioned at the midpoint of the spread. Filters, geophone and shot point locations, and other parameters were adjusted for each file to optimize the reflected or refracted waves of interest on the Strataview display. Each site utilized a variety of shot offsets to record different raypaths and deeper reflections and refractions. Shotpoint locations consisted of an initial offset of 4m (0m coordinate; near-shot), 2m (48m coordinate; mid-shot), then 4m (100m coordinate far-shot). Additional far offsets ranged from 34m to 100m in-line with the geophone spread. Sledgehammer swings were aimed directly onto the center of the striker plate and were stacked two to four times per shotpoint. Betsy gun shotpoints were prepared by first hand-auguring a 1m deep hole, inserting the loaded barrel into the ground, and then packing native material back into the hole to prevent blowback. When released, the firing pin (attached to the shot cable) triggered the explosive.

Horizontal geophones were also employed at sites CA-GTS-3 and CA-GTS-4. These geophones were positioned at the same locations as the vertical geophones (every 4m; oriented transversely to the spread line) to record shear waves. This characterization of S- waves provided an independent method of calculating *Vs* values needed for HVSR bedrock depth calculation. These *Vs* values were valid only for the specific site (or that unique drift thickness). To ensure horizontal wave motion generation, a rectangular trench was dug deep enough to accommodate a vertically oriented striker plate and sledge hammer swing. Planting transverse horizontal

geophones and directing hammer blows horizontally in opposite directions (approximately east-west) cancelled most P-wave events while also amplifying shear waves on the field record. Each hammer blow was stacked twice in opposite directions for a total of four stacks per record. Some of horizontal geophone spread shotpoints utilized explosive sources as described previously.

Processing

Seismic data were then processed using IXRefraX Interpex and SIP (DOS-based program) display and modelling software. Analysis required adjusting display gain parameters, applying high-cut filters, and identifying seismic waveform events of interest on the time-domain seismic record. Direct and refraction events were recognized on high-gain displays by locating first breaks (i.e., the first non-noise ground motion). Shear waves arrived after the direct P-wave event at approximately twice the travel time of the P-wave arrival. Shear- waves were best recognized on a reduced-gain display. Reflected P- and S- wave arrivals were characterized on the screen display by a half hyperbola alignment across the spread. The relevant waveform was then tracked from one channel to the next, which generated characteristic graphs defined by the distance (determined by geophone number and spacing) and time (accurate to 0.25 ms per channel depending on pick values). The top-of-water-saturation was the first identifiable boundary for P-waves. Deeper investigation into the seismic record was performed by analyzing waveform trends at later times. Refraction modelling in SIP utilized picks to create depth model plots; reflection analysis used the simple X^2 -T^2 method to derive velocities and depths to reflectors from hyperbolic arrival events (assuming horizontal boundaries and isotropic velocity within each layer).

CHAPTER IV

RESULTS

HVSR Survey

More than 412 HVSR recording stations were collected across the two topographic quadrangles and immediately surrounding area. Additionally, 26 of those stations had duplicate stations obtained concurrently with another Tromino unit, and 23 stations were repeated on a different day. Only 249 of the 412 HVSR stations were considered reliable enough for map construction (Figure 13). The study site calibration curve was composed of 18 calibration stations (Table 1; Figure 14). Four of these calibration readings were taken at the four previously discussed test boring sites, while the remaining fourteen stations were taken near residential water wells that penetrated bedrock. Drift thickness (in feet) for Table 1 was provided from water well or test boring records, whereas the *Vs* was calculated by using equation 1 (refer to Chapter 2 in this study). The calculated depth (in feet) was obtained from applying the calibration equation (Figure 14) to the station's f_0; this value was then compared to the actual depth value to calculate the percent difference. The log-log plot of the bedrock depth (meters) vs. resonance frequency data produced a regression line with the equation of $y=101.39x^{-1.464}$ (refer to equation 2 in this study) and an R^2 of 0.9498. These calibration data were also plotted in terms of shear wave velocity calculated from the fundamental equation (equation 1) with respect to bedrock depth, supporting the expectation that *Vs* generally increased with depth due to compaction and lithification (Figure 15).

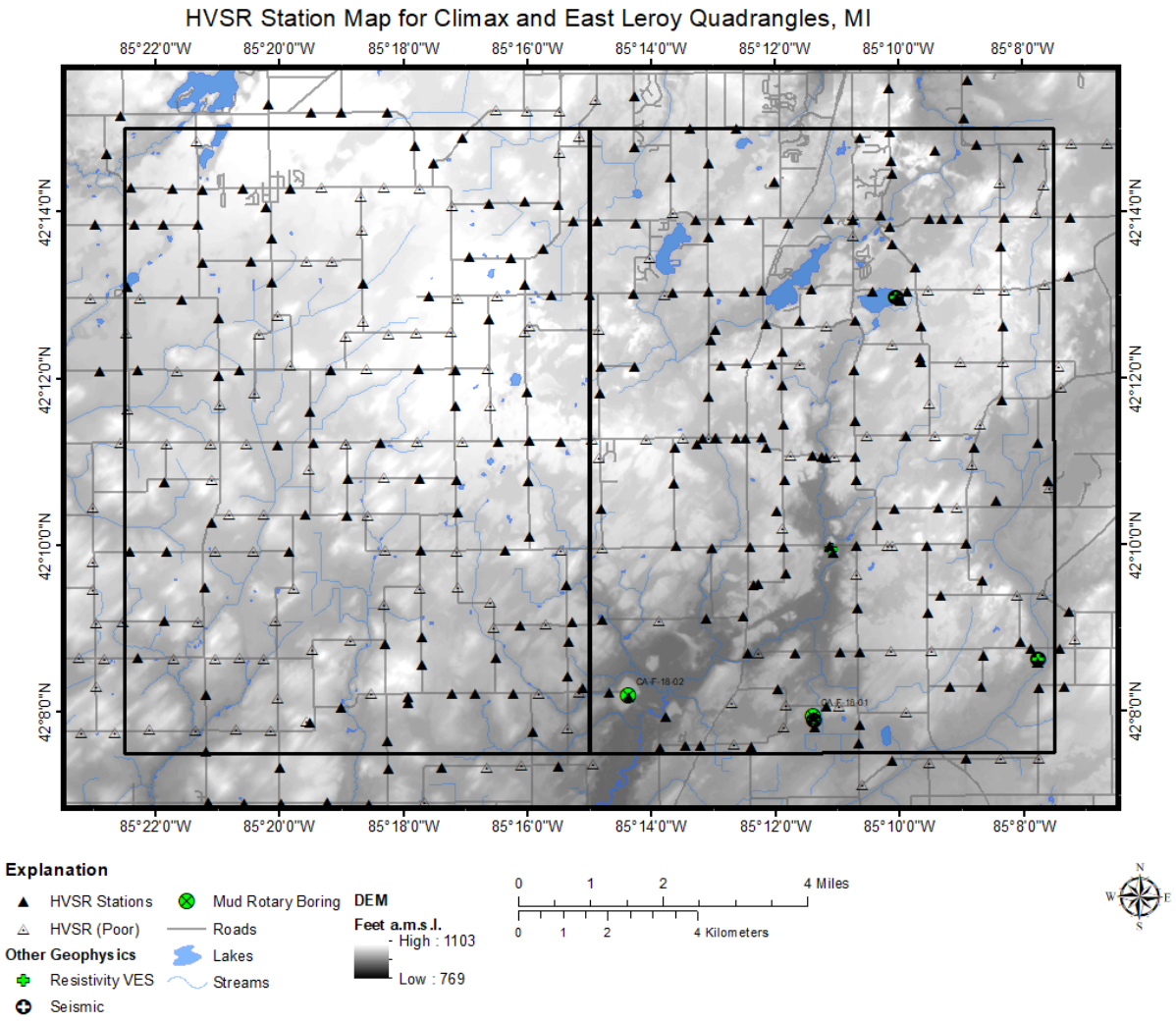

Figure 13. Map displaying data collected for this project. Note that HVSR stations denoted as "poor" failed to meet SESAME criteria, had localized noise, and/or had low amplitude compound or multiple peaks that did not correspond to reasonable bedrock depths. Mud rotary boring locations are also labeled. Several additional stations are located outside the map extent to avoid edge artifacts during contouring.

Table 1. Calibration stations used to create the power law regression plot presented in Figure 14 and the shear wave velocity plot from Figure 15.

Calibration Stations							
Station No.	fo (Hz)	Drift Thickness (m)	Drift Thickness (Ft)	Vs (m/s)	Boring	Calculated Depth (ft)	% Difference
CAL-007	5.5	7.92	26	174.35		27.42	5.47
CAL-027R	1.75	45.72	150	320.04	CA-13-14	146.61	2.26
CAL-060R	4.94	9.14	30	180.69		32.09	6.97
CAL-070	5	9.75	32	195.07		31.53	1.48
CAL-096	3.31	19.20	63	254.24		57.67	8.46
CAL-025R	3.69	16.15	53	238.44		49.19	7.19
CAL-101R	2.31	22.56	74	208.41		97.65	31.95
CAL-111	2.5	26.82	88	268.23		86.98	1.16
CAL-158	3.75	13.72	45	205.74		48.04	6.75
KAL-489	1.75	46.63	153	326.44	KA-13-01	146.61	4.17
KAL-499	2.16	25.30	83	218.58		107.73	29.80
CAL-264	2.94	21.03	69	247.33		68.60	0.58
CAL-274	2.69	27.13	89	291.89		78.13	12.21
CAL-144	2	39.62	130	317.00		120.58	7.25
CAL-147	2.63	31.39	103	330.27		80.75	21.60
CAL-278	2.16	33.53	110	289.69		107.73	2.06
CAL-268	2.31	30.79	101	284.46	CA-F-18-01	97.65	3.32
CAL-200	1.81	40.84	134	295.71	CA-F-18-02	139.55	4.14
Average							8.71

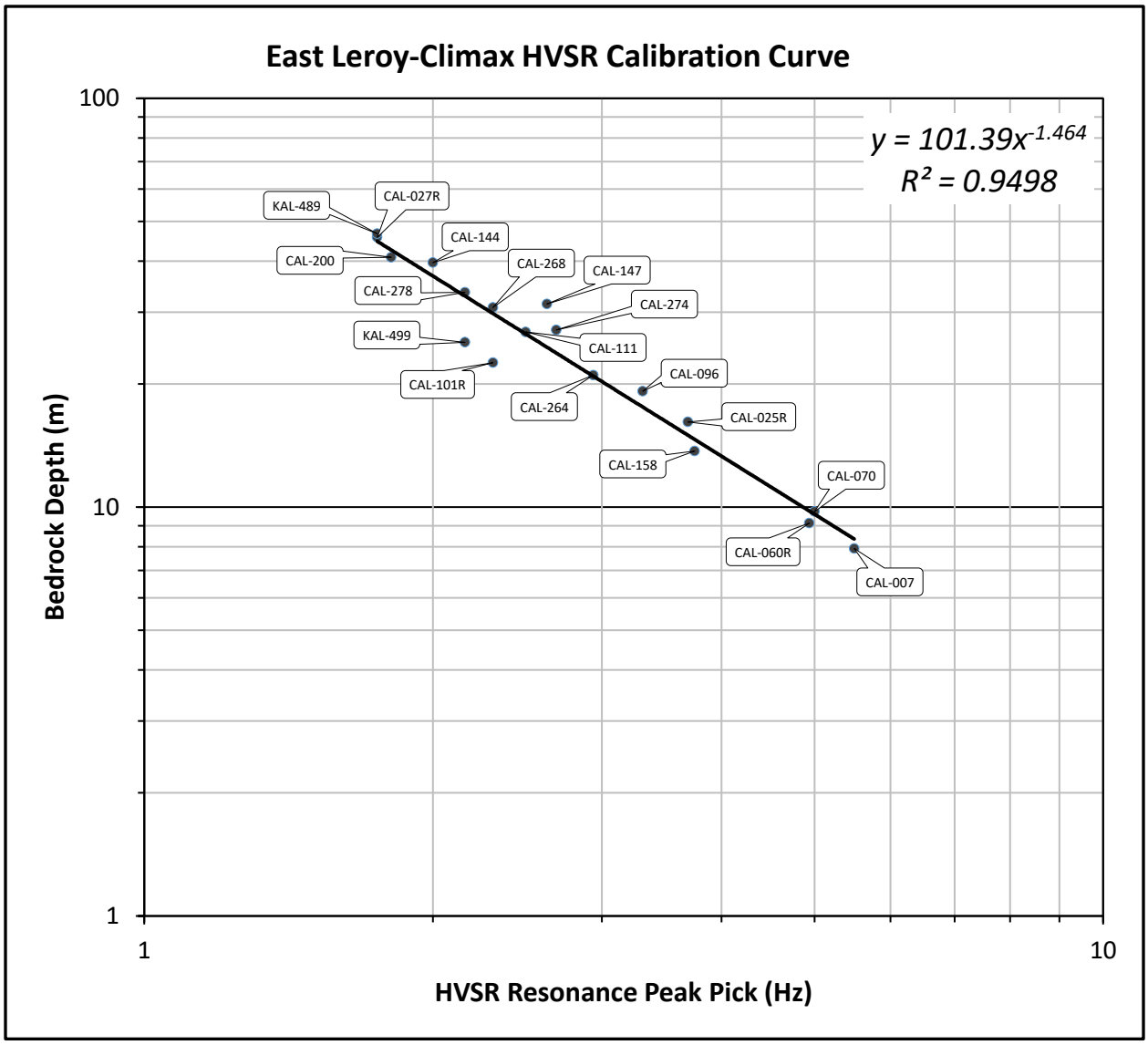

Figure 14. HVSR power-law regression plot of calibration points. The equation used to calculate bedrock depths is located at the top right of the graph. Stations CAL-027R, KAL-489, CAL-268, and CAL-200 were taken at test borings labeled CA-13-14, KA-13-01, CA-F-18-01, and CA-F-18-02 respectively.

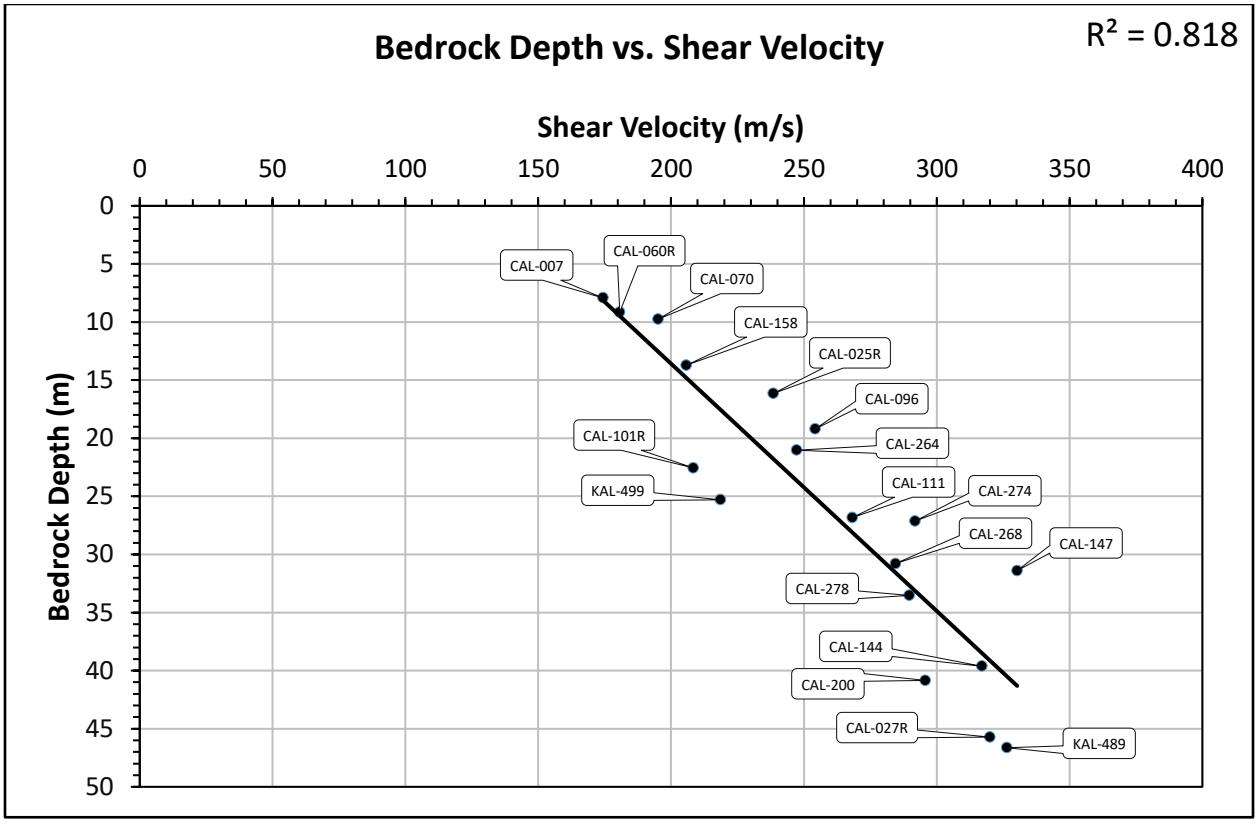

Figure 15. Plot displaying shear wave velocity increasing with depth using the data presented in Figure 14.

GIS Mapping & Cross-Sections

Interpolation methods in GIS were used to create and then contour uniform grids of estimated drift thicknesses (Figure 16) and bedrock elevations (Figure 17) using HVSR points, available water wells, test borings, and oil and gas wells. A DEM map with hillshade overlay was also created (Figure 18; notable surface valleys were outlined for reference). Bedrock topography and drift thickness maps consisting strictly of HVSR points were also created as a means to compare data (Figure 19). Results reveal two broad bedrock depressions oriented NW-SE that appear to be cross-cut by a NE-SW trending linear valley (Figure 20). Bedrock uplands seem to continue southward and eastward. Overall, bedrock relief is estimated to be about 110 meters (361 feet). Drift thickness maps appear to mimic the bedrock topography, with thicknesses ranging from 3 meters (10 feet) to 110 meters (361 feet). Thinnest regions of drift appear to be located on bedrock uplands, while the thickest drift packages are located within bedrock valleys and lowlands.

Several cross-sections were created along survey lines identical to previous works. Results from two gravity profiles by Farnsworth (1980) were compared to findings presented in this study (Figures 22 and 23). Interpreted 2-D industry seismic data lines were also traced to compare subsurface information (Figures 24, 25, and 26). However, note that 2D seismic section images (2-way time on y-axis) were not provided with depth interpretations, so only qualitative comparisons between bedrock surfaces were possible. (Note: seismic data owned or controlled by Seismic Exchange, Inc.; interpretation is that of Tyler Norris, John A. Yellich, William Sauck, Alan Kehew, and Robb Gillespie).

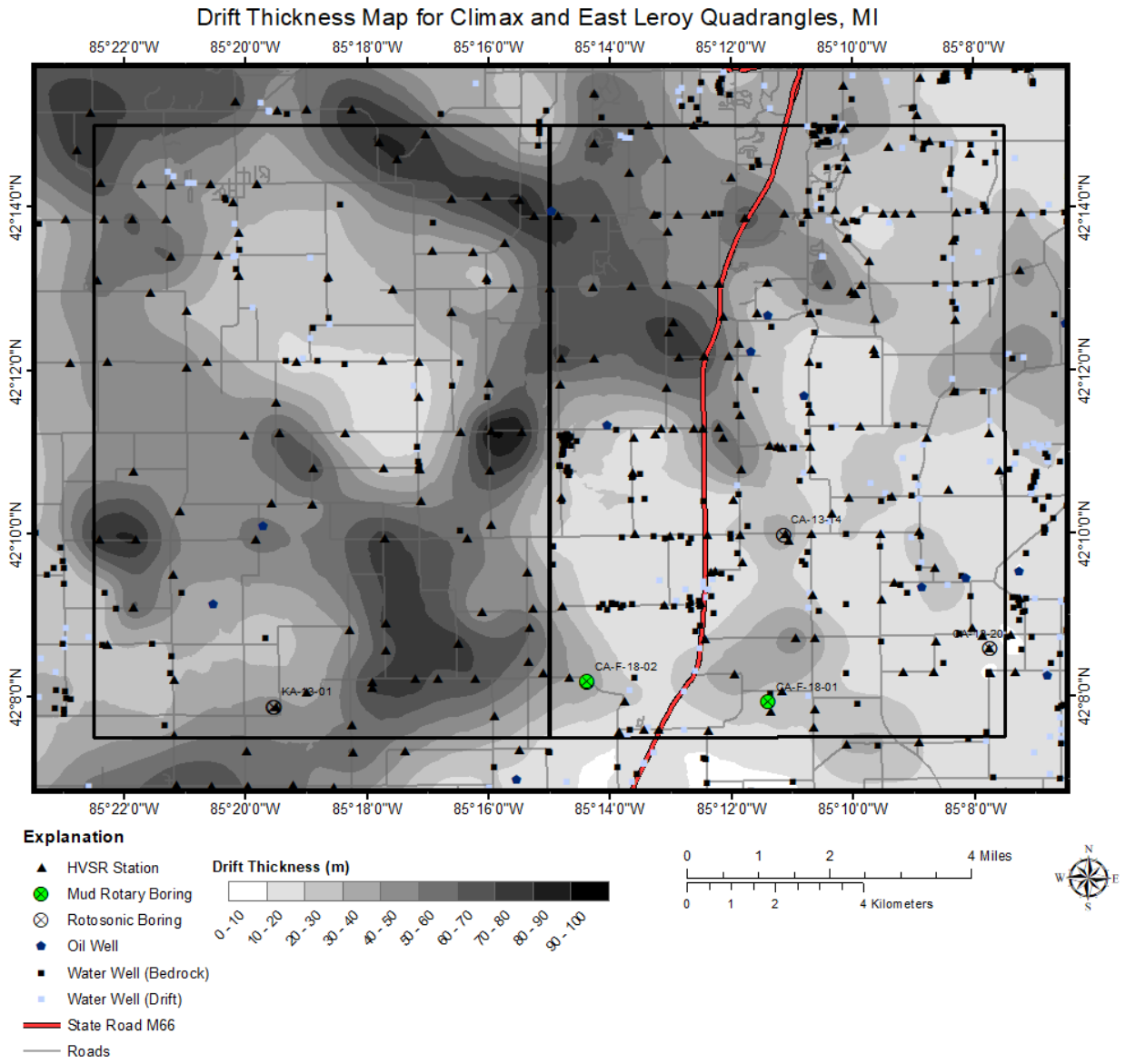

Figure 16. Drift thickness map displaying data point locations used to create a depth to bedrock (surface elevation – estimated bedrock elevation). Note that "Water Well (Drift)" points were not reported to penetrate bedrock but had total depths deeper than the interpolated bedrock surface (i.e., "push-down" method described in Chapter 3 of this study).

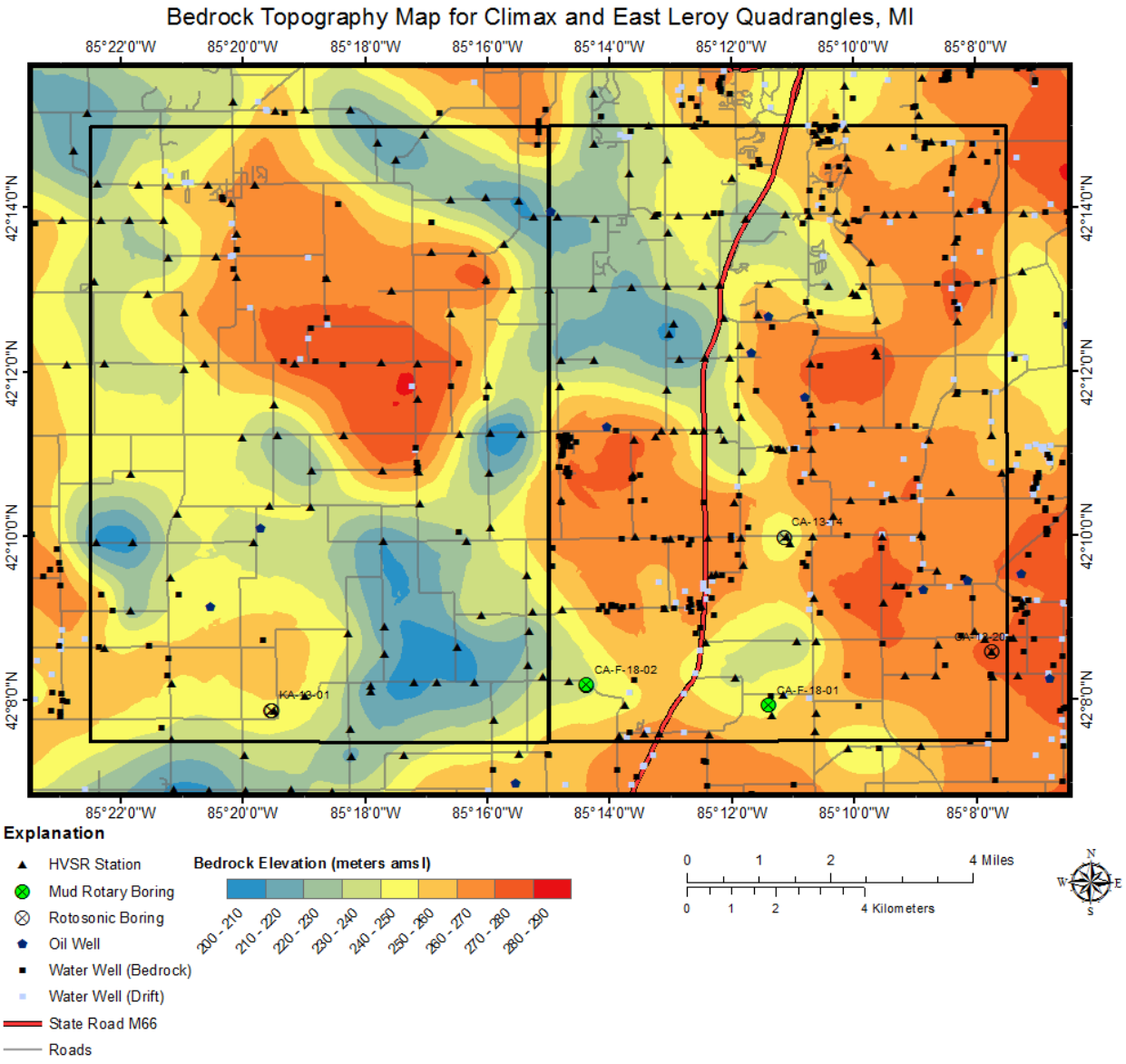

Figure 17. Bedrock topography map displaying data point locations used to create a bedrock raster surface. Note that "Water Well (Drift)" points were wells that were not reported to penetrate bedrock but had total depths deeper than the interpolated bedrock surface (i.e., "push-down" method described in Chapter 3 of this study).

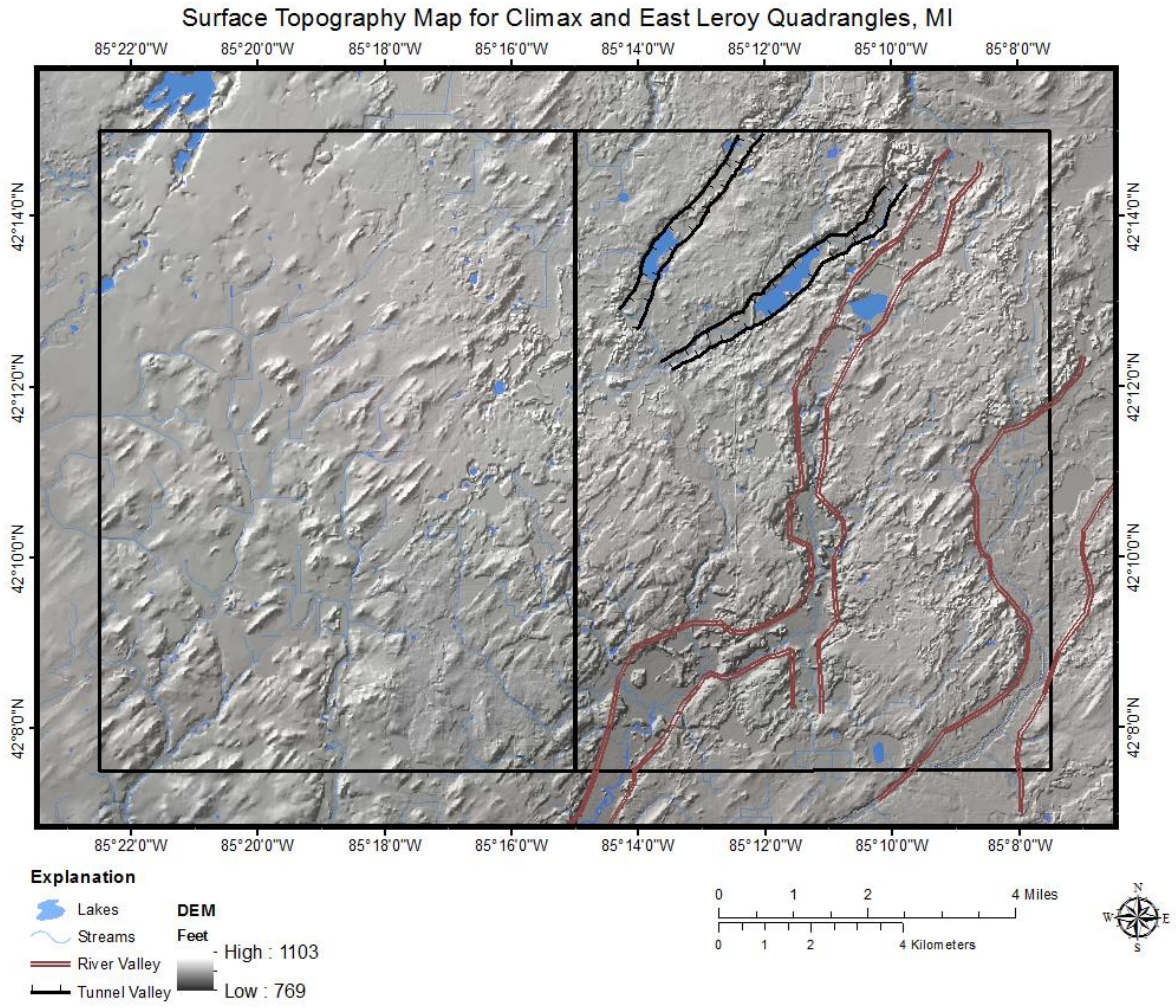

Figure 18. Surface DEM with hillshade of the study area displaying two surficial tunnel (black hashed lines) valleys and two notable river valleys (solid red lines) outlined.

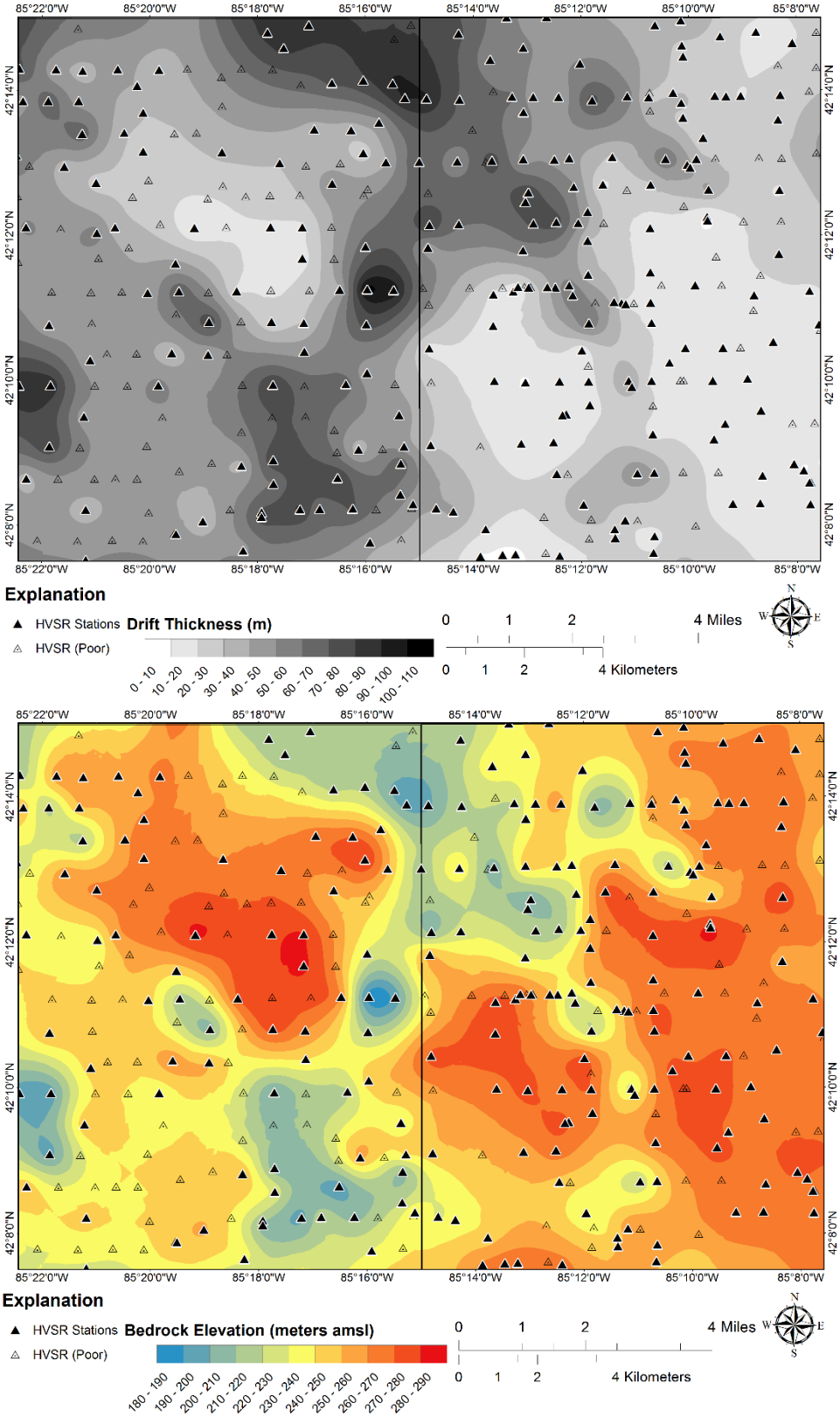

Figure 19. Drift thickness (Top) and bedrock topography (Bottom) kriging interpolation map using only quality HVSR points. Note the similarity between this map and Figures 16 and 17.

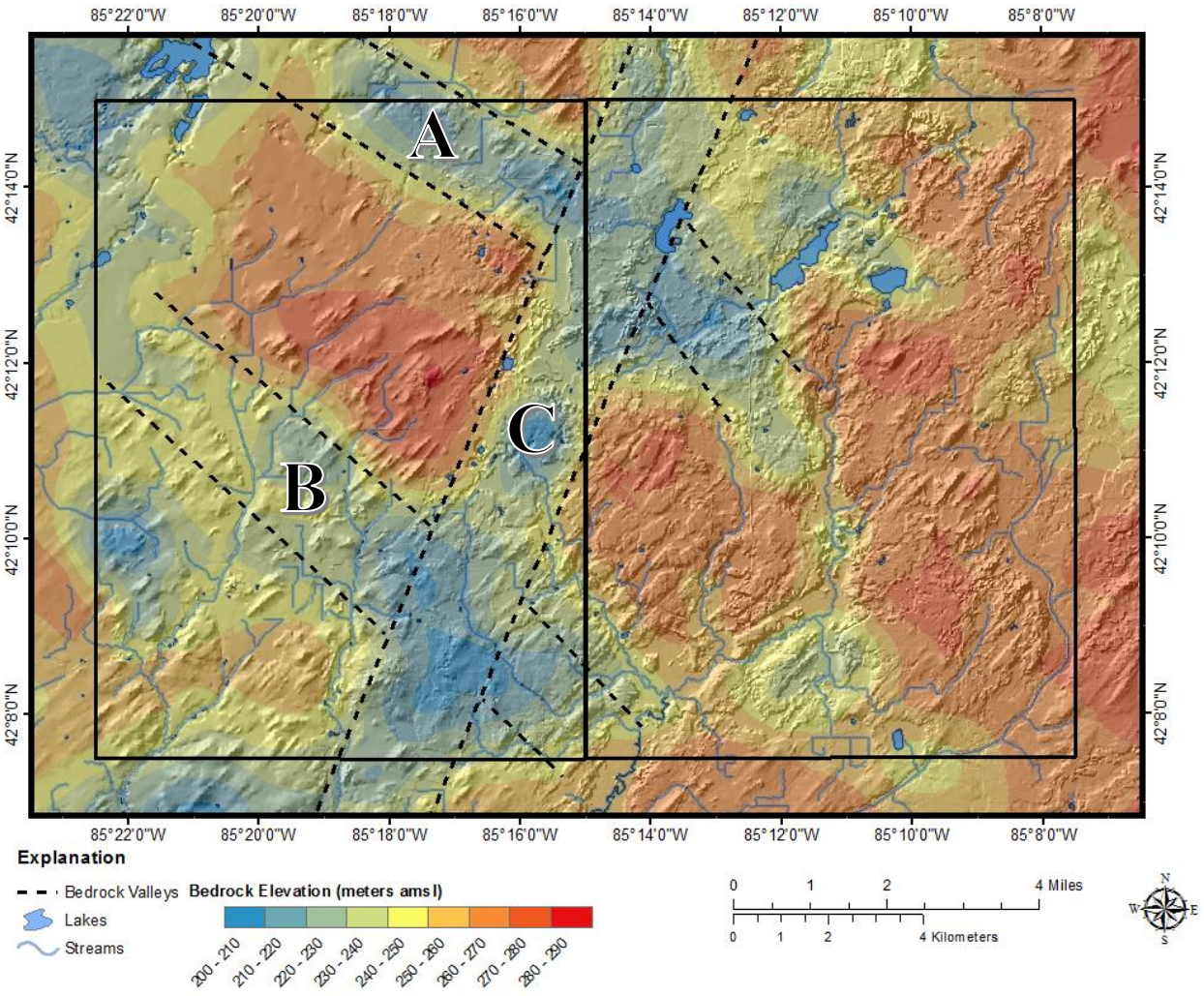

Figure 20. Bedrock topography map (colored) overlain with hillshade, streams, and lakes for surficial reference. Approximate bedrock valley locations are depicted by dashed lines. Note that the buried valleys do not correlate strongly with surface elevation/hillshade or water features.

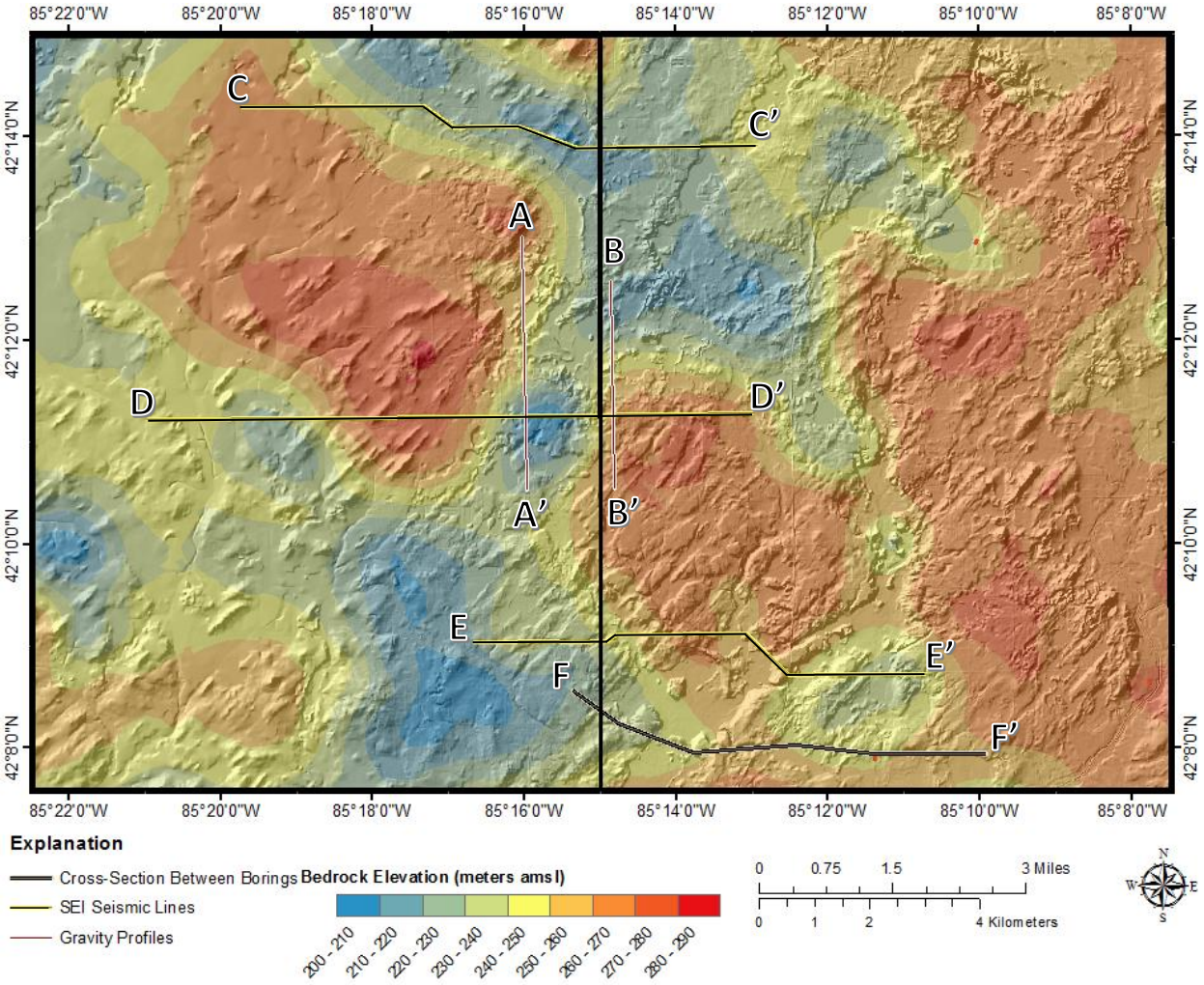

Figure 21. Bedrock topography map (colored) overlain with hillshade for surficial reference. Cross-section lines are depicted as solid lines and correspond to Figures 22 (A-A'), 23 (B-B'), 24 (C-C'), 25 (D-D'), 26 (E-E') and 30 (F-F').

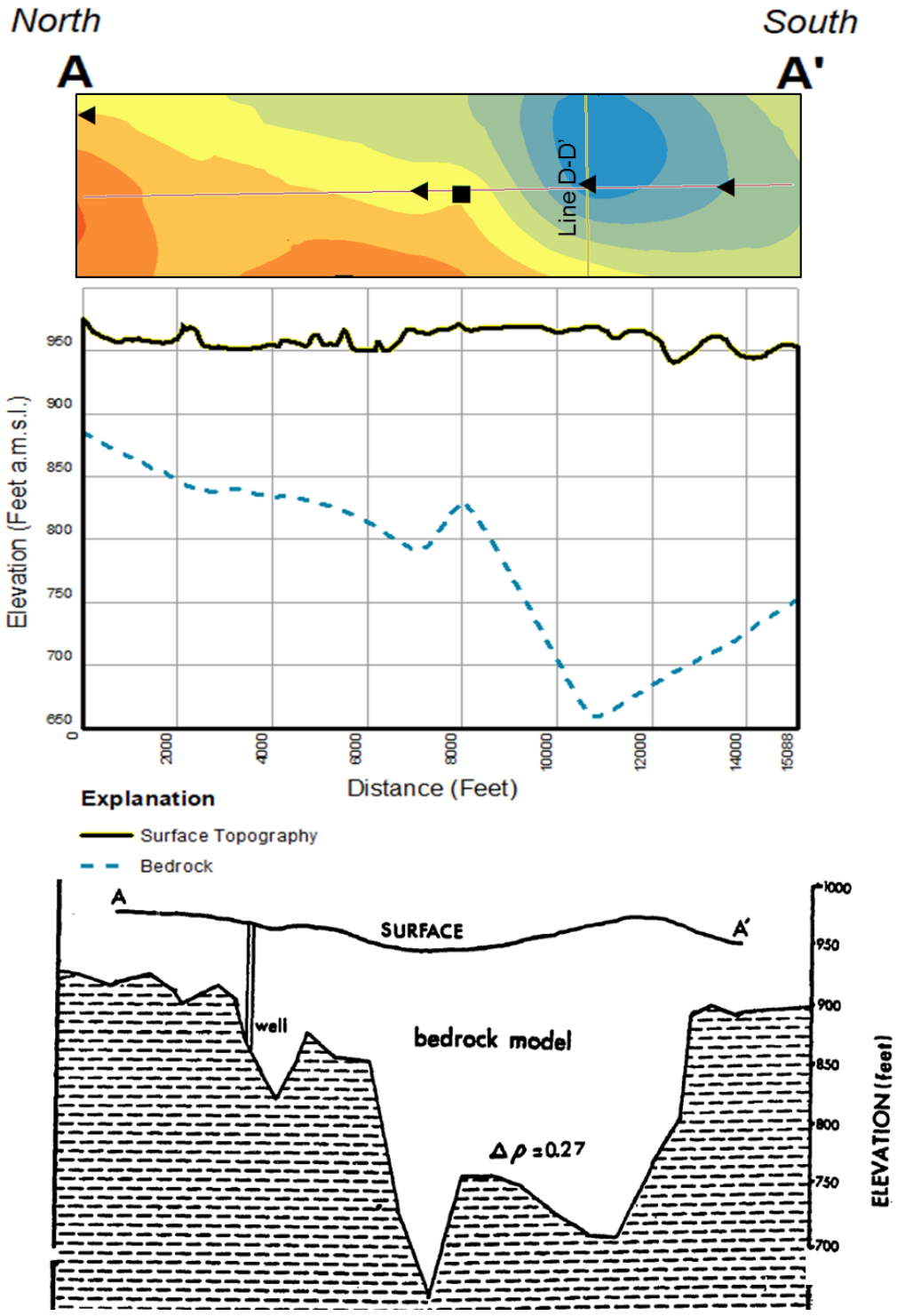

Figure 22. Cross-section A-A' from Figure 21 through HVSR and control well interpolated bedrock depths (Top; see Figure 17 for explanation) and the cross-section derived from gravity methods from Farnsworth (1980 - Bottom, modified).

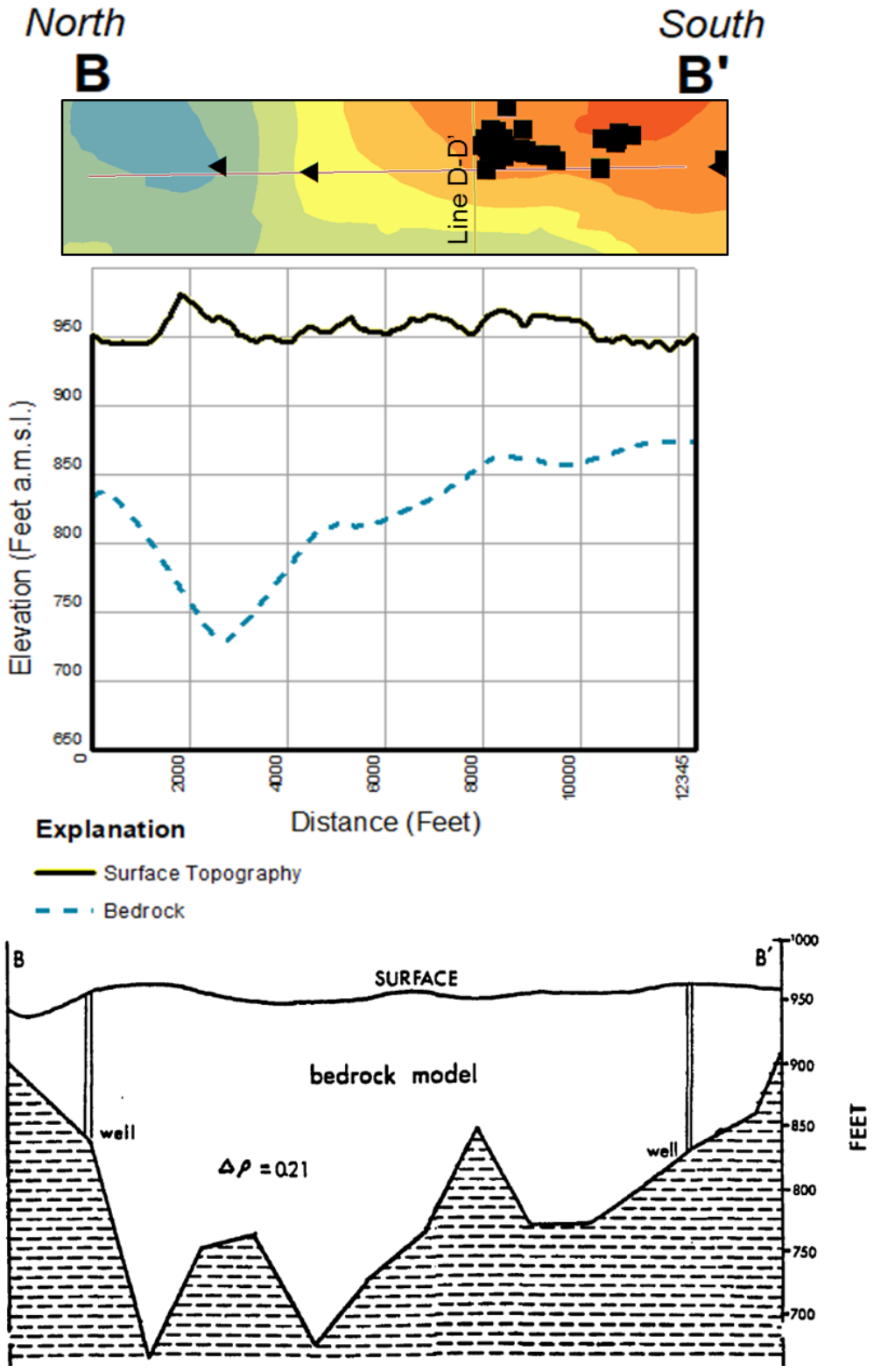

Figure 23. Cross-section B-B' from Figure 21 through HVSR and control well interpolated bedrock depths (Top; see Figure 17 for explanation) and the cross-section derived by gravity methods from Farnsworth (1980 - Bottom, modified).

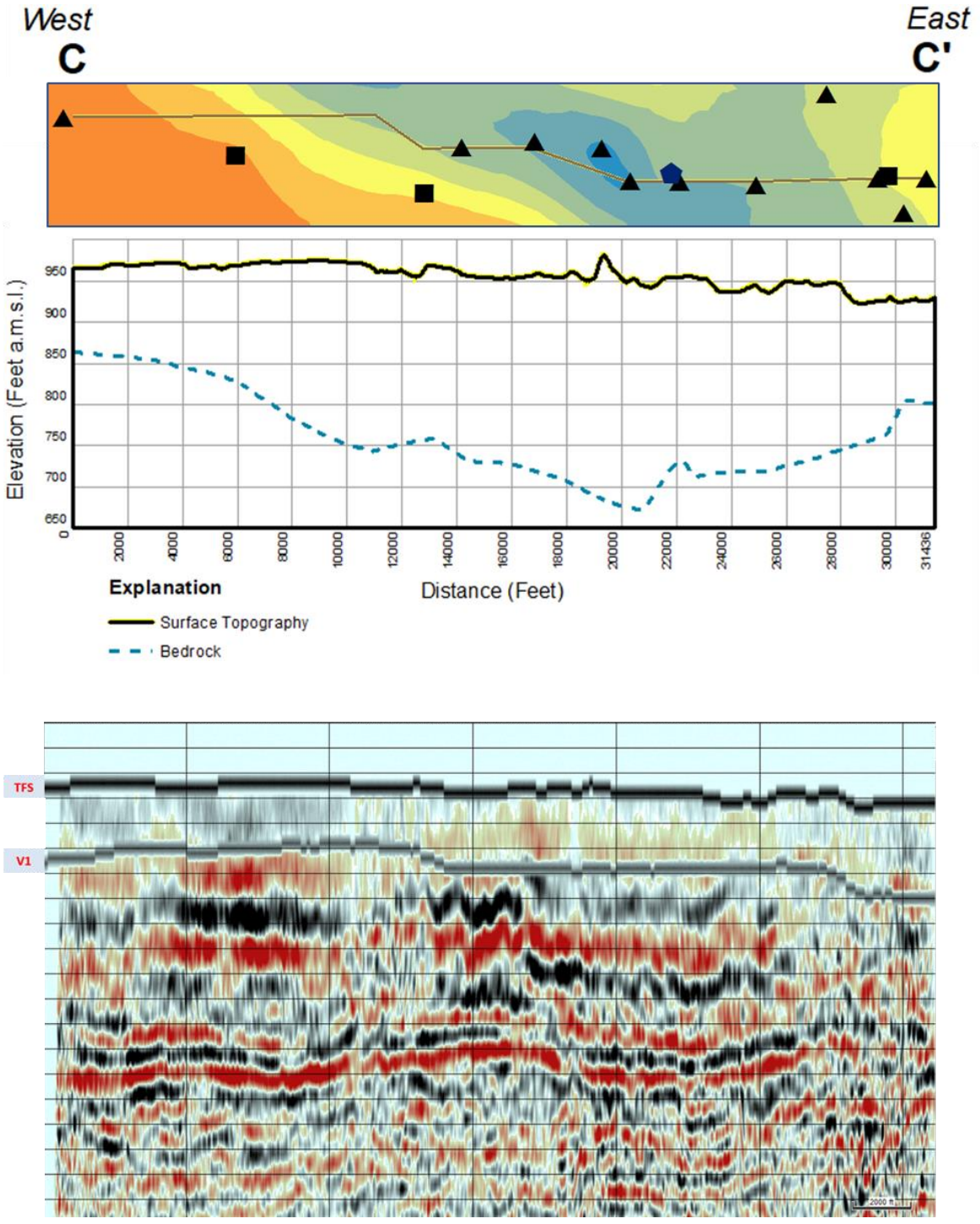

Figure 24. Cross-section C-C' from Figure 21 through HVSR and control well interpolated bedrock depths (Top; 30x vertical exaggeration; see Figure 17 for map view explanation) and the seismic section obtained from Wolverine Gas and Oil, SEI (Bottom; used with permission). Note that the seismic section has an interpreted boundary of bedrock-glacial drift denoted as V1 (units of 2-way time); black line labelled as TFS (Time of First Sample) represents surface elevation.

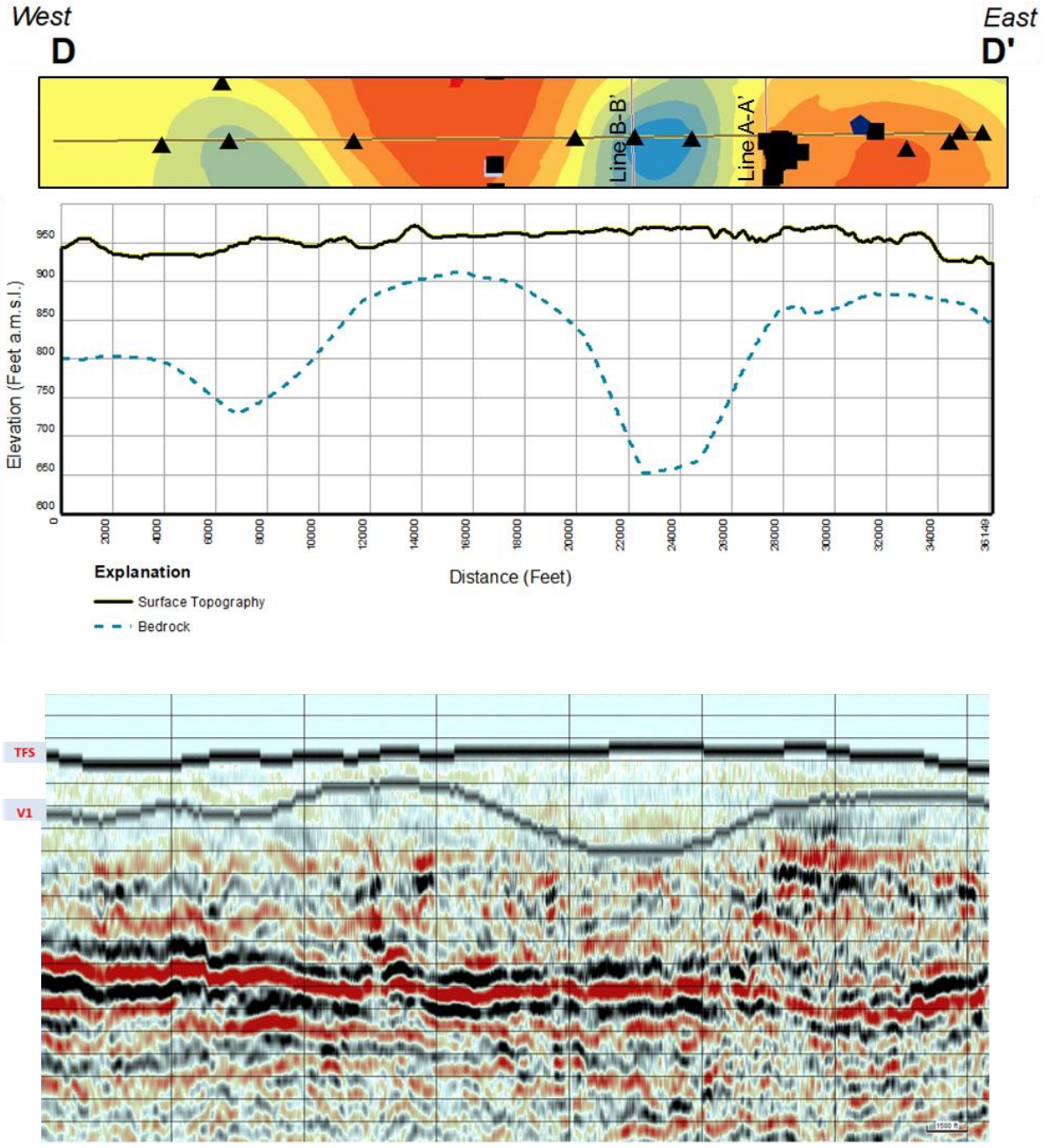

Figure 25. Cross-section D-D' from Figure 21 through HVSR and control well interpolated bedrock depths (Top; 30x vertical exaggeration; see Figure 17 for map view explanation) and the seismic section obtained from Wolverine Gas and Oil, SEI (Bottom; used with permission). Note that the seismic section has an interpreted boundary of bedrock-glacial drift denoted as V1 (units of 2-way time); black line labelled as TFS (Time of First Sample) represents surface elevation. Also note the similarity in bedrock topography between the two sections.

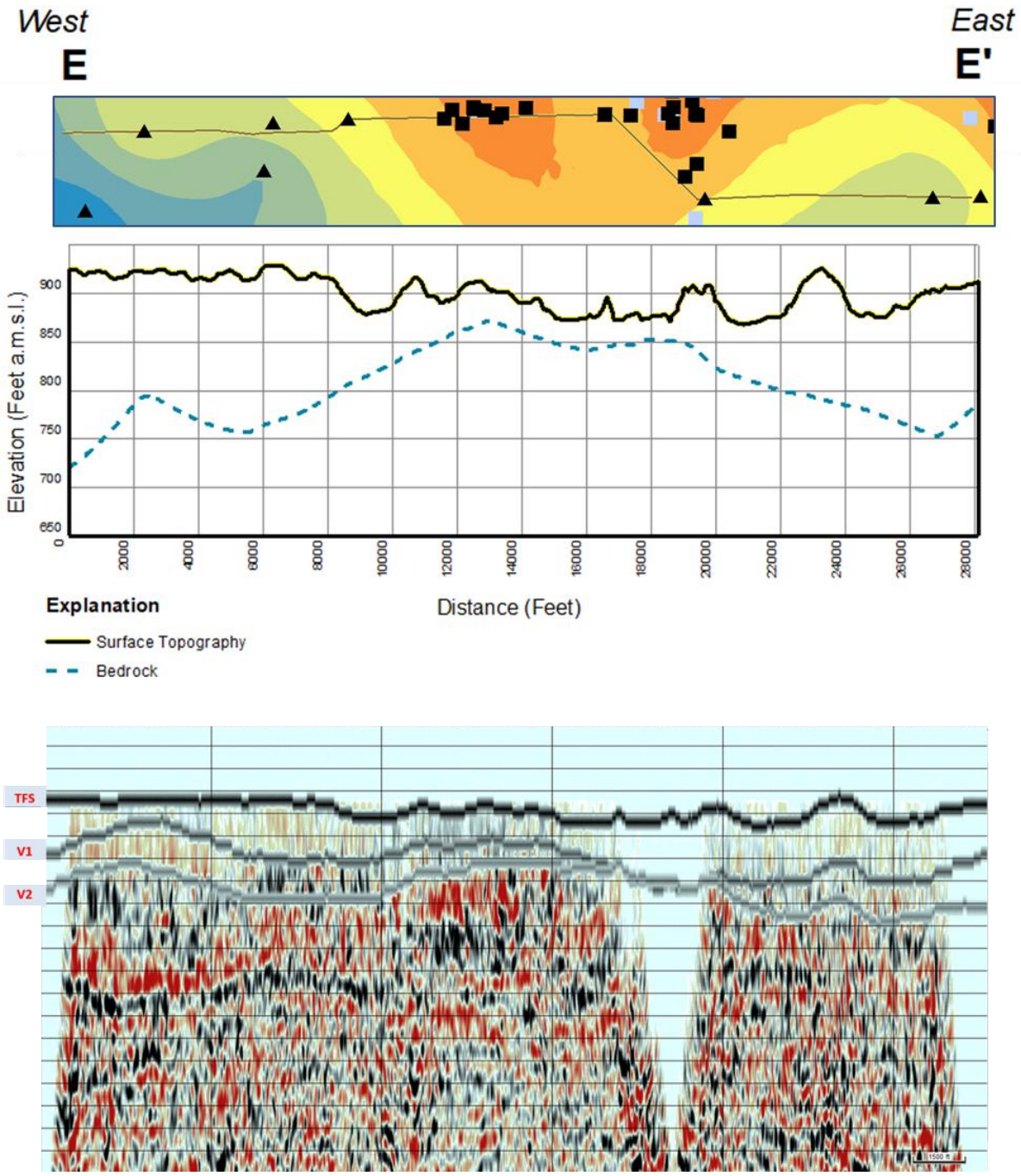

Figure 26. Cross-section E-E' from Figure 21 through HVSR and control well interpolated bedrock depths (Top images; 30x vertical exaggeration; see Figure 17 for map view explanation) and the seismic section obtained from Wolverine Gas and Oil, SEI (Bottom; used with permission). Note that the seismic section has two possible interpreted boundaries between bedrock-glacial drift (V1 and V2 - units of 2-way time), indicating difficult waveform tracking. Black line labelled as TFS (Time of First Sample) represents surface elevation. Blank zones in the seismic section are due to missing surface coverage (i.e., the survey did not have access permission).

Error Analysis

Validation of the HVSR readings involved several statistical analyses. Because several of the repeated and concurrent stations were considered "poor," and thus had variable *fo*, error analysis, for consistency, was performed by comparing a common resonance frequency in each set of records. The average peak frequency difference calculated for concurrent stations was 0.01Hz (average percent difference of 0.51%) (Table 2). This form of comparison was also conducted for stations repeated on a different day to yield an average peak frequency difference of 0.03Hz (average percent difference of 0.98%) (Table 3). Figure 27 shows histograms displaying the distribution of these data.

Direct comparisons between bedrock depths at control stations and HVSR depths calculated from the power-law calibration curve were also used to judge the internal consistency of the HVSR method and bedrock elevation model. This analysis was performed for stations recorded at a known bedrock depth (i.e., calibration stations). The average difference between the calculated bedrock depth and the observed control-well bedrock depth was 8.71% for these 18 calibration stations (See Figure 14). Note that an alternate statistic is shown by the R^2 value of 0.9498 on Figure 14, which is a measure of the predictive value of the power-law curve.

Table 2. Results of concurrent stations. The station was noted when the peak determined by Grilla was not chosen for comparison; such stations consequently do not have a standard deviation included.

Concurrent											
STATION	**Fo (A) (Hz)**	**Std. Dev. (A)**	**H/V Ampl (A)**	**Fo (B) (Hz)**	**Std. Dev. (B)**	**H/V Ampl (B)**	**Fo (A) - Fo (B) (Hz)**	**Avg. Fo (Hz)**	**Avg. Std. Dev.**	**% Fo Diff**	**Note**
CAL-013	7.44	-	2.68	7.40	-	2.98	0.04	7.42	-	0.54	Chose higher f peak for comparison
CAL-014	1.00	6.82	2.91	1.00	1.05	4.00	0.00	1.00	3.94	0.00	
CAL-015	2.13	0.75	3.70	2.00	0.77	2.97	0.13	2.07	0.76	6.30	
CAL-016	5.16	-	2.43	5.02	-	2.64	0.14	5.09	-	2.75	Chose a higher f peak for comparison
CAL-017	1.19	-	5.87	1.19	0.28	5.25	0.00	1.19	-	0.00	Chose edge of broad Fo peak for B
CAL-018	0.81	0.20	4.57	0.75	0.62	4.43	0.06	0.78	0.41	7.69	
CAL-019	0.88	0.46	4.05	0.88	0.64	4.47	0.00	0.88	0.55	0.00	
CAL-020	9.56	6.05	2.58	9.56	5.09	2.78	0.00	9.56	5.57	0.00	
CAL-021	2.75	0.78	9.73	2.75	0.09	6.34	0.00	2.75	0.44	0.00	
CAL-022	1.69	0.10	4.93	1.56	0.12	4.65	0.13	1.63	0.11	8.00	
CAL-023	1.63	0.10	4.96	1.50	0.1	4.87	0.13	1.57	0.10	8.31	
CAL-024	1.06	0.15	5.42	1.06	0.18	4.31	0.00	1.06	0.17	0.00	
CAL-025	1.00	0.48	4.62	1.00	0.2	4.19	0.00	1.00	0.34	0.00	
CAL-026	1.00	0.05	4.13	1.06	0.19	2.82	-0.06	1.03	0.12	-5.83	
CAL-027	1.88	0.04	7.03	1.94	0.05	6.14	-0.06	1.91	0.05	-3.14	
CAL-196	1.81	0.63	2.99	1.75	2.39	2.78	0.06	1.78	1.51	3.37	
CAL-197	1.88	0.29	3.67	1.88	3.05	3.43	0.00	1.88	1.67	0.00	
CAL-198	1.31	0.09	4.03	1.38	0.11	3.15	-0.07	1.35	0.10	-5.20	
CAL-199	1.13	0.42	3.38	1.19	0.29	2.64	-0.06	1.16	0.36	-5.17	
KAL-476	1.19	0.19	3.01	1.15	-	2.48	0.04	1.17	-	3.42	Double Peaks; Chose 1.19Hz peak from A
KAL-477	1.85	-	3.57	1.81	0.18	3.41	0.04	1.83	-	2.19	Doube Peaks; Chose 1.81Hz peak from B
KAL-478	1.88	0.27	3.31	1.81	0.21	2.99	0.07	1.85	0.24	3.79	
KAL-479	2.38	0.48	3.58	2.44	3.48	3.80	-0.06	2.41	1.98	-2.49	
KAL-480	2.38	0.21	2.64	2.50	0.45	2.42	-0.12	2.44	0.33	-4.92	
KAL-481	1.06	0.49	3.23	1.13	17.79	2.58	-0.07	1.10	9.14	-6.39	
KAL-482	1.88	0.42	2.67	1.88	0.67	2.48	0.00	1.88	0.55	0.00	
Average							**0.01**			**0.51**	

Table 3. Results of repeated stations. The station was noted when the peak determined by Grilla was not chosen for comparison; such stations consequently do not have a standard deviation included.

Repeat											
STATION	**Fo (Hz)**	**Std. Dev.**	**H/V Ampl**	**Fo (R) (Hz)**	**Std. Dev. (R)**	**H/V Ampl (R)**	**Fo - Fo (R) (Hz)**	**Avg. Fo (Hz)**	**Avg. Std. Dev.**	**% Fo Diff**	**Note**
CAL-007	5.50	0.44	4.78	5.25	1.93	3.69	0.25	5.38	1.19	4.65	
CAL-008	3.75	0.93	3.17	3.53	0.33	6.37	0.22	3.64	0.63	6.04	
CAL-023A	1.63	0.10	4.96	1.44	0.02	6.03	0.19	1.54	0.06	12.38	
CAL-027A	1.88	0.04	7.03	1.69	0.14	5.56	0.19	1.79	0.09	10.64	
CAL-031	2.13	0.08	3.58	1.88	0.13	3.54	0.25	2.01	0.11	12.47	
CAL-060	4.56	0.14	5.89	4.94	0.05	5.01	-0.38	4.75	0.10	-8.00	
CAL-101	2.28	0.10	5.20	2.31	0.10	5.30	-0.03	2.30	0.10	-1.31	
CAL-116	1.76	-	3.85	1.88	0.07	5.08	-0.12	1.82	-	-6.59	A-chose second peak, diff fo
CAL-145	1.19	0.06	7.20	1.19	0.11	5.35	0.00	1.19	0.09	0.00	
CAL-151	2.81	0.04	4.96	2.81	0.07	4.78	0.00	2.81	0.06	0.00	
CAL-172	1.63	0.26	3.21	1.50	0.01	4.47	0.13	1.57	0.14	8.31	
CAL-183	1.19	-	5.51	1.31	0.08	4.57	-0.12	1.25	-	-9.60	A- chose edge of peak
CAL-203	1.78	0.05	3.48	1.81	0.42	3.02	-0.03	1.80	0.24	-1.67	
CAL-253	2.28	0.73	4.14	2.38	0.56	3.02	-0.10	2.33	0.65	-4.29	
CAL-254	1.75	0.24	3.62	2.00	0.18	4.01	-0.25	1.88	0.21	-13.33	
CAL-257	4.00	0.47	3.38	3.44	0.69	2.88	0.56	3.72	0.58	15.05	
CAL-262	3.44	0.02	6.18	3.63	0.07	5.70	-0.19	3.54	0.05	-5.37	
CAL-269	1.13	0.03	5.78	1.09	0.05	5.24	0.04	1.11	0.04	3.60	
KAL-489	1.75	0.11	3.39	1.75	-	3.81	0.00	1.75	-	0.00	R- Broad; Chose edge of peak
KAL-513	1.16	0.02	4.78	1.22	0.09	5.05	-0.06	1.19	0.06	-5.04	
KAL-548	3.31	0.64	2.63	3.13	0.94	2.97	0.18	3.22	0.79	5.59	
KAL-571	2.75	0.66	4.47	2.75	0.08	3.90	0.00	2.75	0.37	0.00	
KAL-577	1.78	0.03	4.56	1.78	0.09	4.78	0.00	1.78	0.06	0.00	
Average							**0.03**			**0.98**	

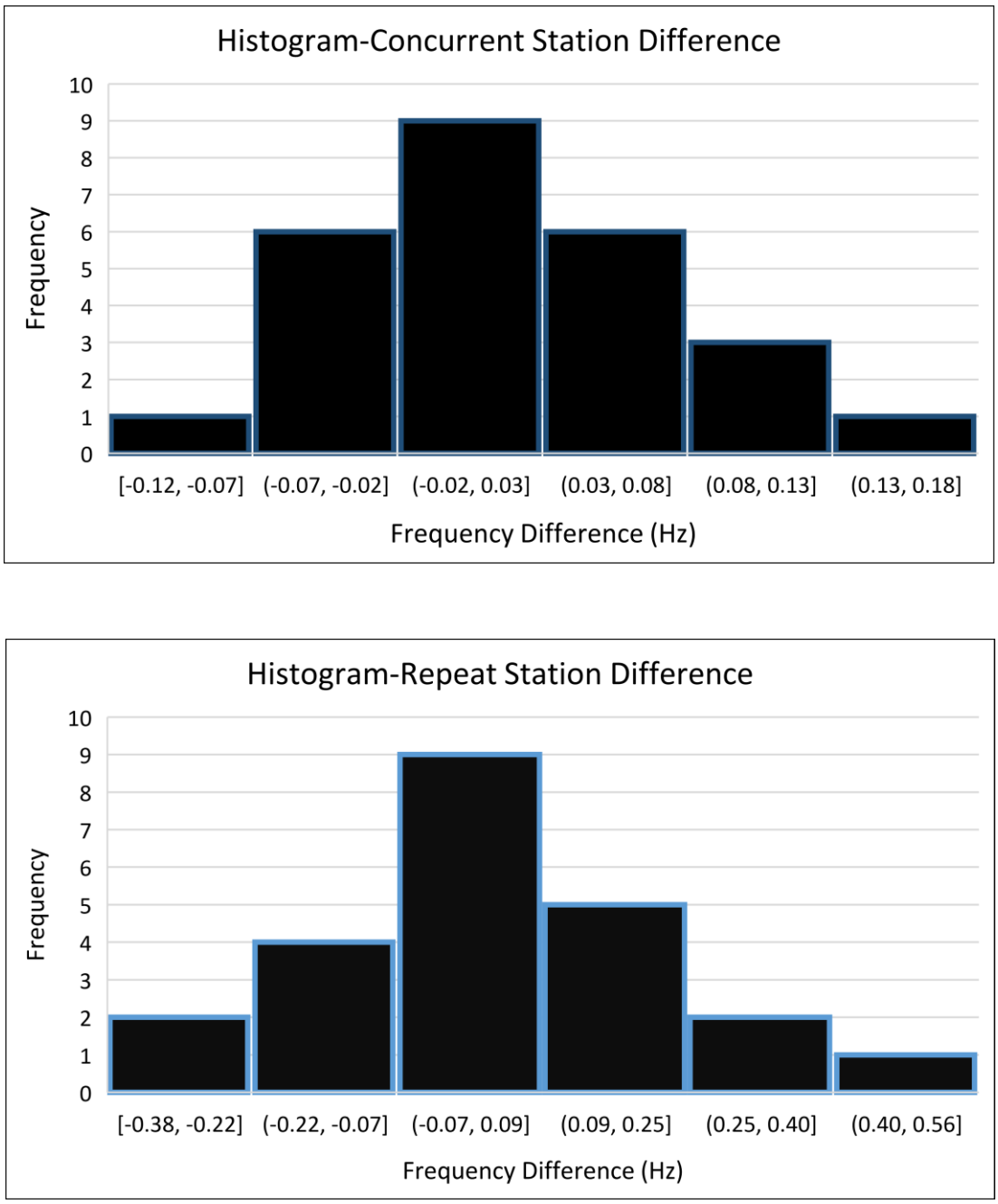

Figure 27. Histograms developed from average differences in frequency (Hz) for concurrent stations (two instruments - Top) and repeat stations (Bottom). Refer to Table 2 and Table 3 for values. Note that both histograms display a distribution similar to a normal bell curve. However, the stations repeated on a different day have greater deviation from zero.

Test Borings

Two test borings (CA-F-18-01 and CA-F-18-02) were drilled using a mud rotary rig to provide additional bedrock control for this project and to offer greater insight into subsurface lithologies. Both borings were drilled into speculative bedrock valleys based on surface topography. An HVSR station was taken at each site prior to drilling to better establish (predict) bedrock depth estimates of 30m (98 ft) for boring CA-F-18-01 (HVSR Station CAL-268) and 42m (138 ft) for boring CA-F-18-02 (HVSR Station CAL-200) (Table 1; Appendix). The calibration curve was later amended to include these HVSR stations (Figure 14).

Several geologists and I collected samples and documented drilling progress. After penetrating several feet into what was inferred to be Coldwater Shale bedrock, the hole was then gamma ray logged using a gamma sonde. Boring CA-F-18-01 was drilled to a total depth of 35m (115 ft), but the bottom several feet collapsed. Therefore, the gamma sonde was unable to log the bottom portion of the hole. This collapse may have influenced gamma detection because the log for boring CA-F-18-01 did not display the expected large increase in gamma ray activity (counts per second or CPS) typical of the clay-rich Coldwater shale that was observed from cuttings. Boring CA-F-18-02 was drilled to total depth of 49m (162 ft) with minimal collapse. Gamma logging results for CA-F-18-02 displayed a clear excursion of gamma signature that corresponded with the dense clay and shale chips along with the driller's observations. A boring log was created for each hole based on drill cutting samples, the driller's log, and the gamma log (Figures 28 and 29). Hole CA-F-18-01 appeared to encounter bedrock at approximately 31m (101ft; 98ft was predicted based on HVSR) and hole CA-F-18-02 encountered bedrock at 41m (134 ft; 138 ft was predicted based on HVSR). The percent difference between the HVSR predicted bedrock depths and the observed bedrock depths were 3.32% (CA-F-18-01; Station

CAL-268) and 4.14% (CA-F-18-02; Station CAL-200) (Table 1). The cross-section between these two borings is provided in Figure 29.

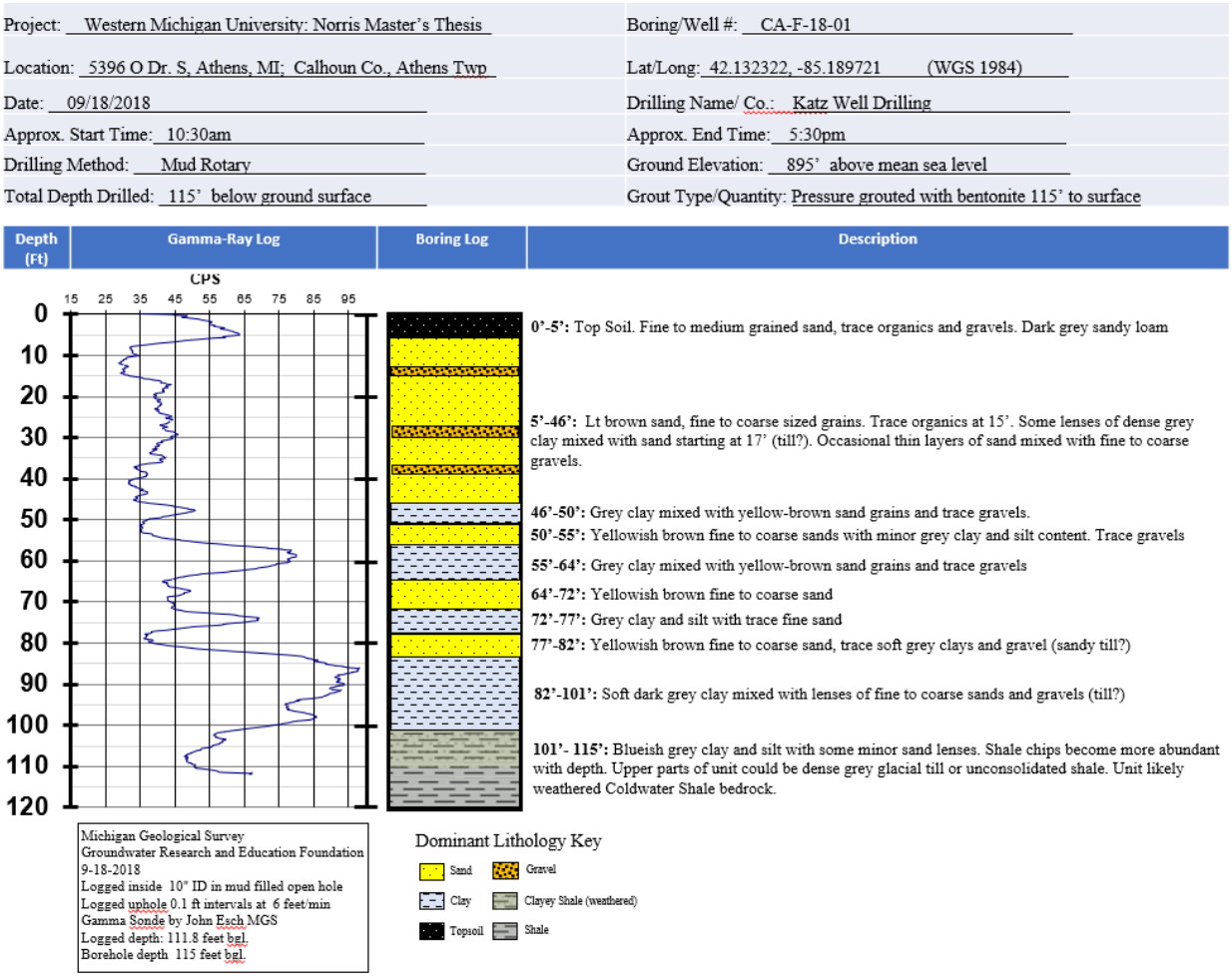

Figure 28. Boring log for CA-F-18-01. Note the gradual lithology change towards the bottom of the hole (101 ft to 115 ft) that is likely indicative of weathered Coldwater Shale or shale debris mixed with clay rich till.

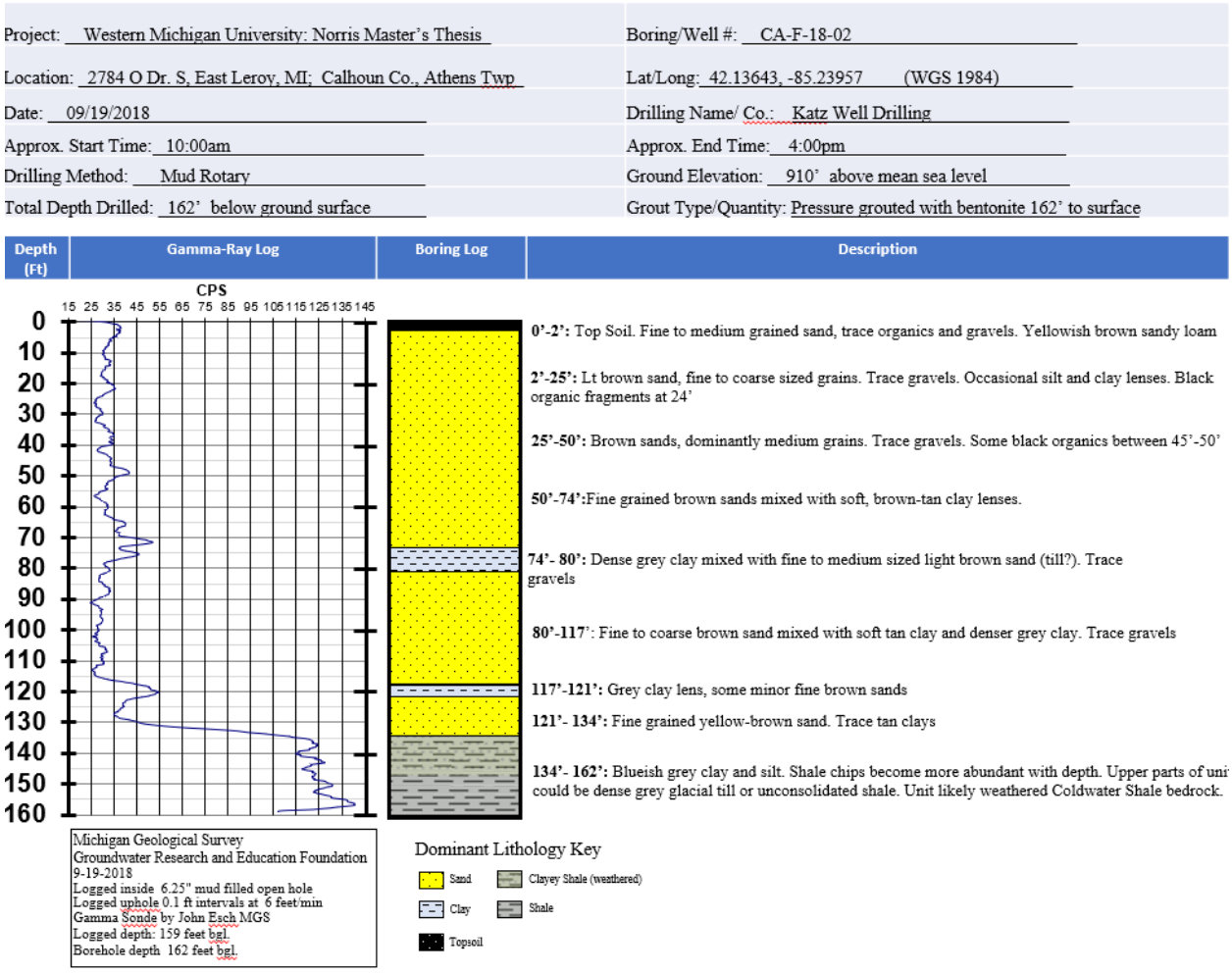

Figure 29. Boring log for CA-F-18-02. Note the observed change in lithology towards the bottom of the hole (134 ft to 162 ft) that is coincident with a strong CPS increase indicative of clay rich shale.

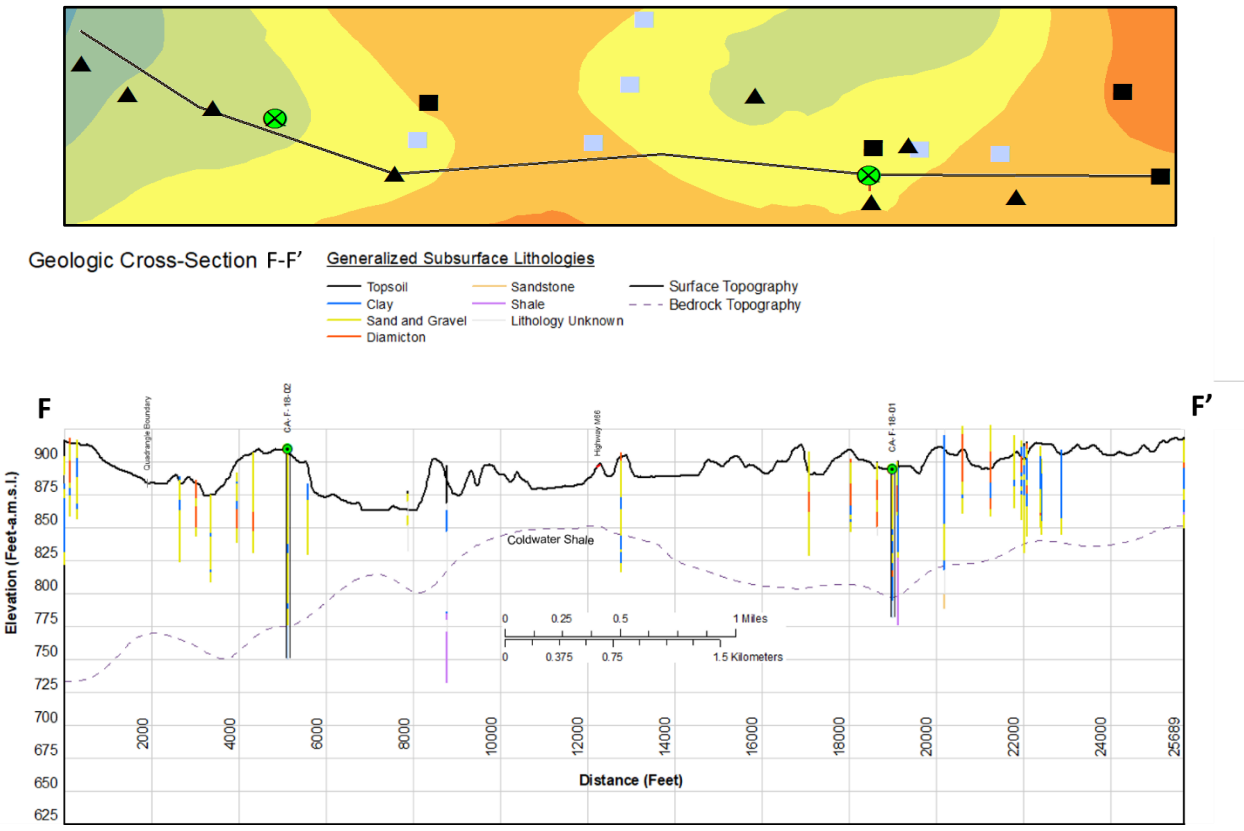

Figure 30. Cross-section along the profile between the two borings performed for this project (See Figure 21; F-F'). Top image displays control points and bedrock topography (See Figure 17 for map view explanation). Note that borings appear to be drilled atop bedrock lowlands. Well lithologies shown for context.

Resistivity & Active Seismic

Electrical and seismic methods performed at four sites (Figures 31, 33, 37, and 42) demonstrated comparable results with boring logs and HVSR data. A VES survey (Cal-01) was conducted at CA-GTS-1 (Figure 31). Results modelled in 1X1D Interpex software suggest a 6-layer case, with resistivity values and layer depths supported by lithologies documented in the log for boring CA-13-14 (Figure 32). Shale bedrock is denoted by a highly conductive layer at 43m (141 ft) modeled depth (fitting error 1.75%). This bedrock depth is similar to boring CA-13-14 (45m; 147 ft), but some variation in interpreted bedrock depth is expected due to VES line placement with respect to the boring, bulk resistivity averaging within the small number of layers within the VES model, and the fundamental assumption of the VES method that boundaries are horizontal. Nearby HVSR stations CAL-027R and CAL-275 tagged bedrock at 45.7m (150m) and 32m (105m), respectively (Table 1; Appendix), indicating variable bedrock topography throughout the area.

Figure 31. Map of CA-GTS-1 displaying resistivity sounding locations in a sand and gravel pit near K Drive S. Note the location of several HVSR stations and boring CA-13-14.

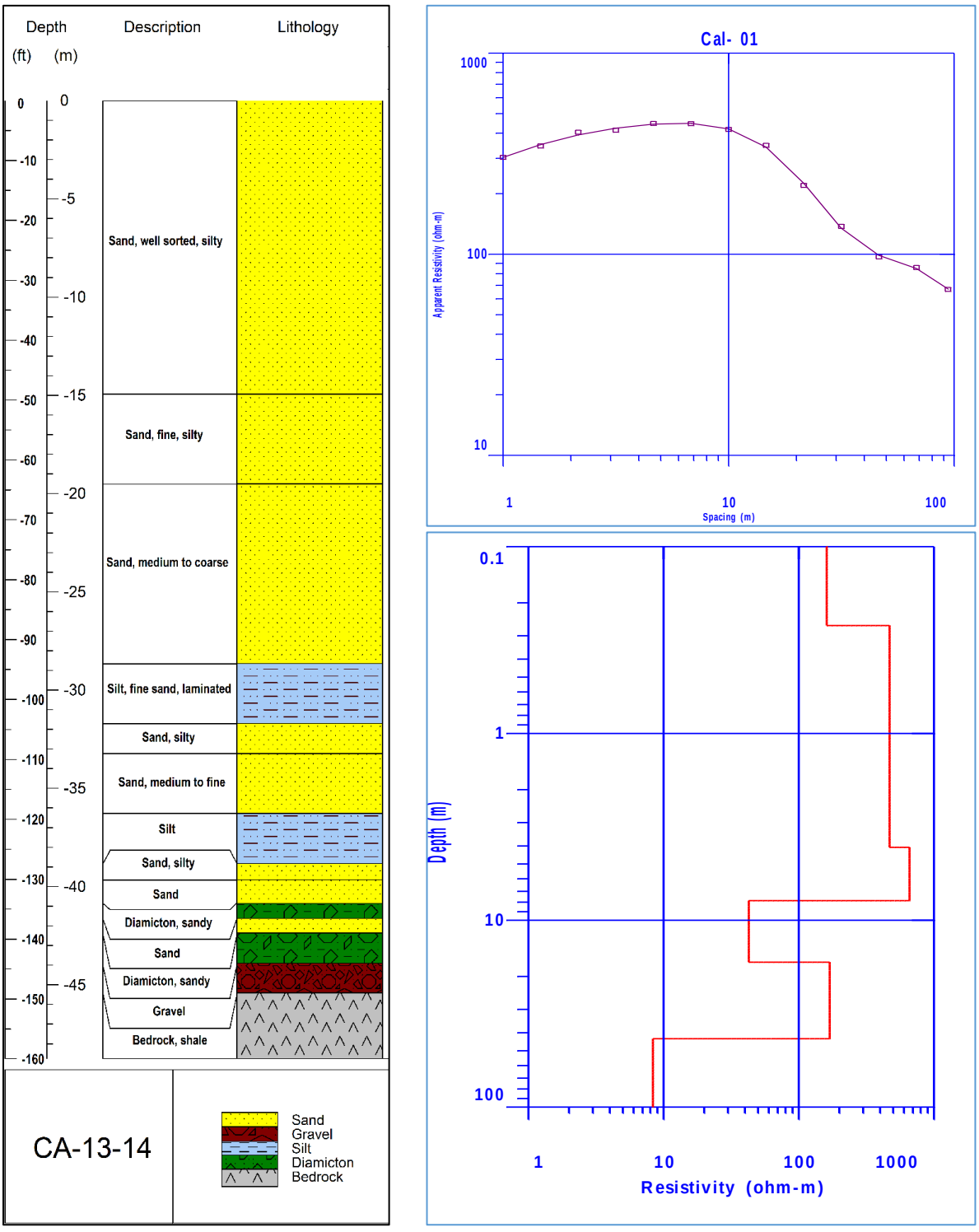

Figure 32. VES results of Cal-01 at site CA-GTS-1 (Right) and boring log from Kehew and Esch, 2014 (Left). Note that a highly conductive layer occurs at about 43m, while the shale bedrock occurs at approximately 45.5m in the boring log. Also note that HVSR stations CAL-027R (close to boring) and CAL-275 (southern end of gravel pit) tag bedrock at 45.7m and 32m, respectively.

Another Schlumberger sounding (Cal-02) was performed at CA-GTS-2 along the edge of a field near the location of another previous rotosonic boring (CA-13-20) (Figure 33). Resistivity sounding results at this location display a 5-layer case, most likely due to saturated zones and slight changes in clay or sand content (Figure 34). The deep conductive layer interpreted at 21.5m (70.5 ft) depth is suggestive of shale bedrock (fitting error 2.53%), however this lithology occurred at 13.4m (44 ft) according to the boring log. The depth discrepancy may be due to variable water content in the sedimentary layers overlying the shale, an uneven and irregular bedrock-glacial contact, or the location of the VES line with respect to the boring. Nearby HVSR station CAL-156, for comparison, has an estimated bedrock depth of 14.6m (48 ft).

Seismic refraction (SEIS1; CAL01) was conducted at site CA-GTS-2 along the same line as vertical electrical sounding Cal-02. P-wave refraction analysis indicates two layer boundaries (Figure 35). Because the bedrock surface is relatively shallow and depth is variable at this location, the second refraction is likely indicative of an irregular bedrock contact ranging from 13m (43 ft) to 17m (56 ft). Reflection analysis identified several reflectors deeper than the reported depth to the Coldwater Shale (Figure 36). Although these reflectors could be lithology changes within the Coldwater Shale, the calculated velocities are relatively low and decrease with depth (which would be highly unusual), suggesting that either weathered or unconsolidated sedimentary clay materials persist with depth or that this later reflection is a seismic multiple.

Figure 33. Map of CA-GTS-2 displaying resistivity and seismic survey lines in a field near N Drive S. Note the locations of several HVSR stations and boring CA-13-20.

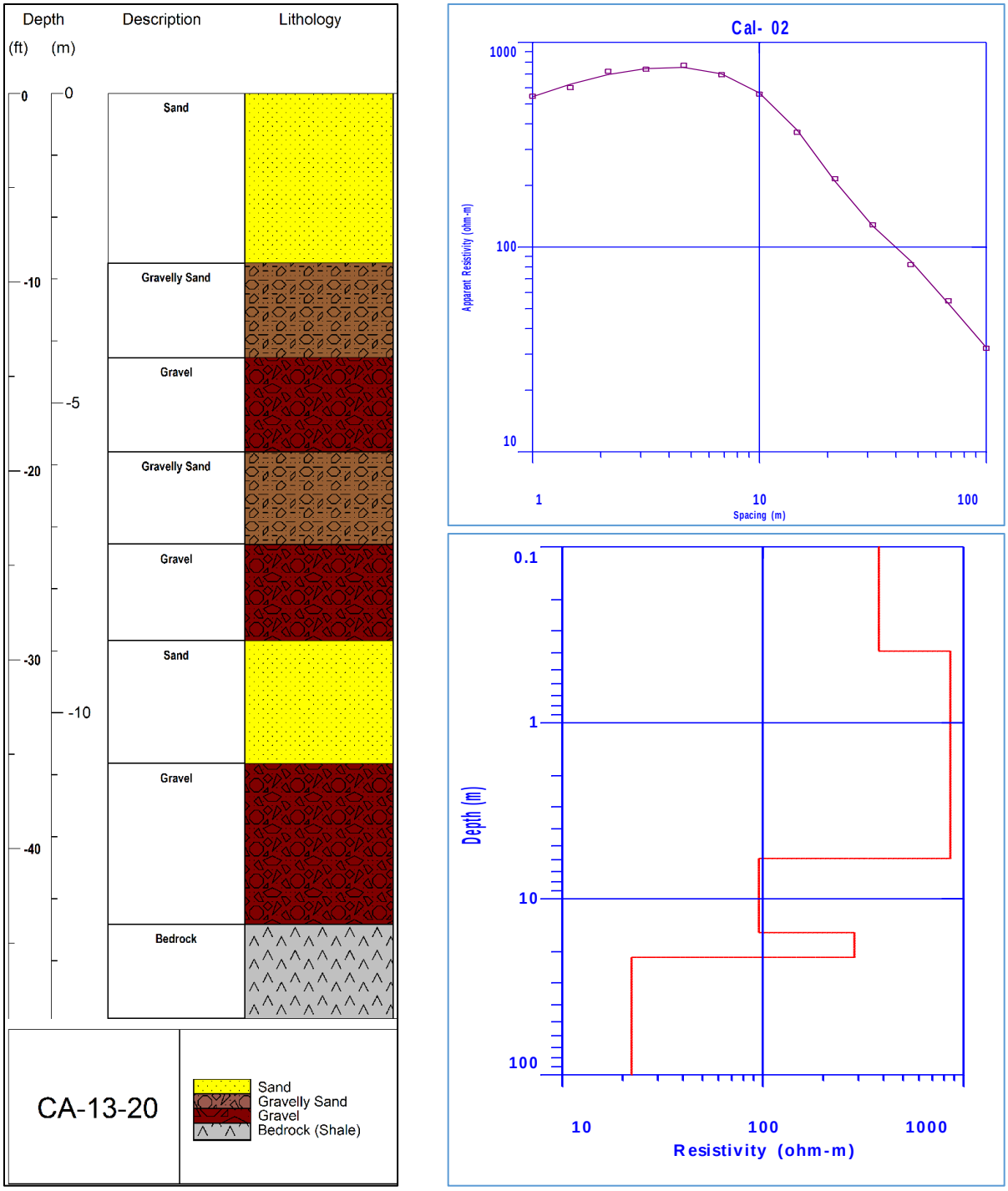

Figure 34. Results of the second VES, Cal-02, at site CA-GTS-2 (Right) and boring log from Kehew and Esch, 2014 (Left). Note that a highly conductive layer was modeled at about 21.5m, while the shale bedrock occurs at approximately 13.4m in the boring log. Also note that HVSR station CAL-158 tagged bedrock at 14.6m (Appendix).

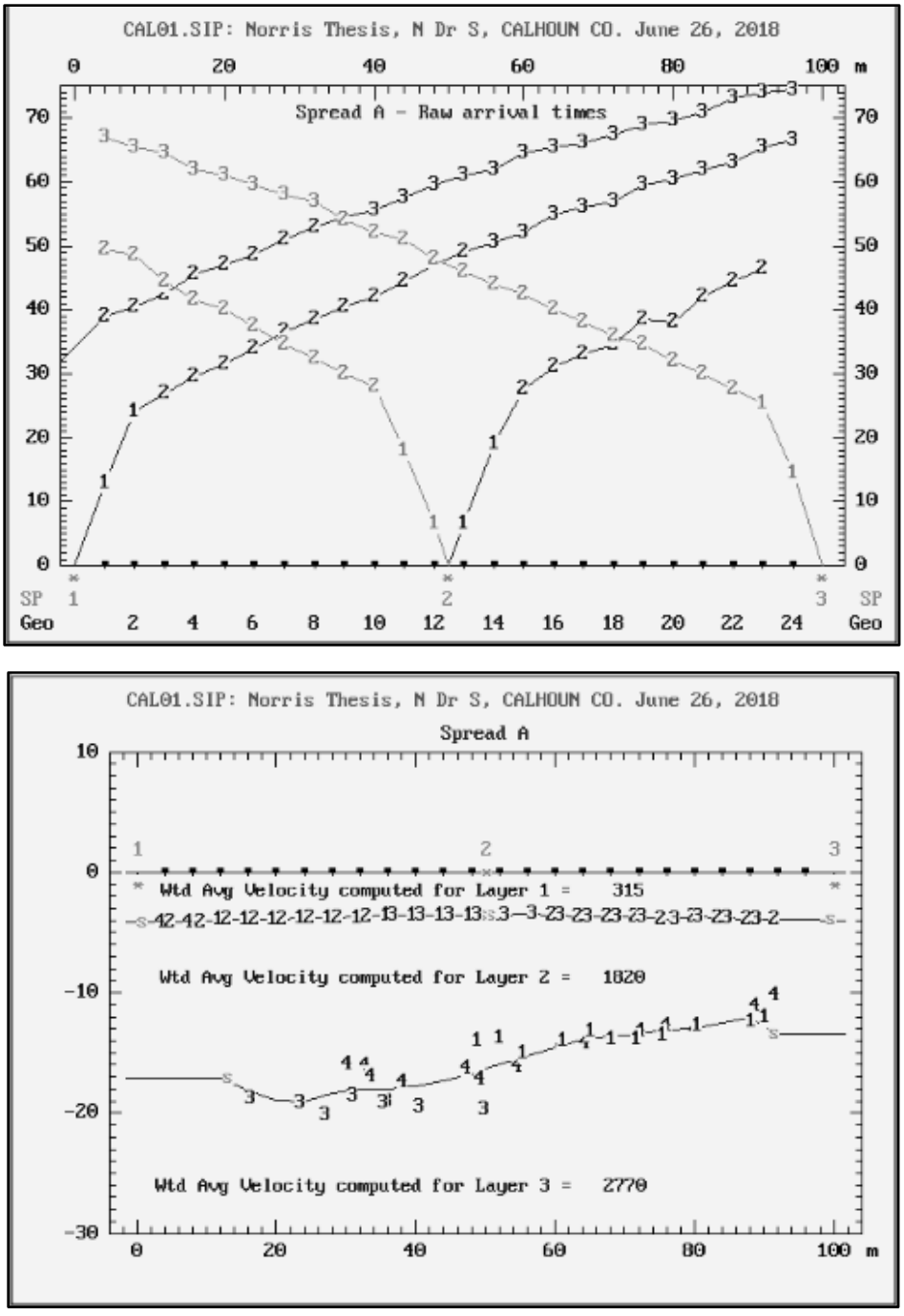

Figure 35. Seismic refraction analysis results for CA-GTS-2. **Top:** SIPT2 program time-distance graph denoting layering assigned from shotpoints. Layers were chosen in accordance with a change in slope of graphed first arrival time picks. **Bottom:** Depth model plot (inversion result). Note the uniform depth to the refractor between Layer 1 and 2, which is indicative of the top of water saturation. The depth to the refraction between Layer 2 and 3 is interpreted as bedrock. Note that the model suggests an irregular contact between saturated glacial sediment and bedrock, with depths varying between 13m and 17m. The depth to the second boundary is within the range of values determined from HVSR and drilling results (Figure 34).

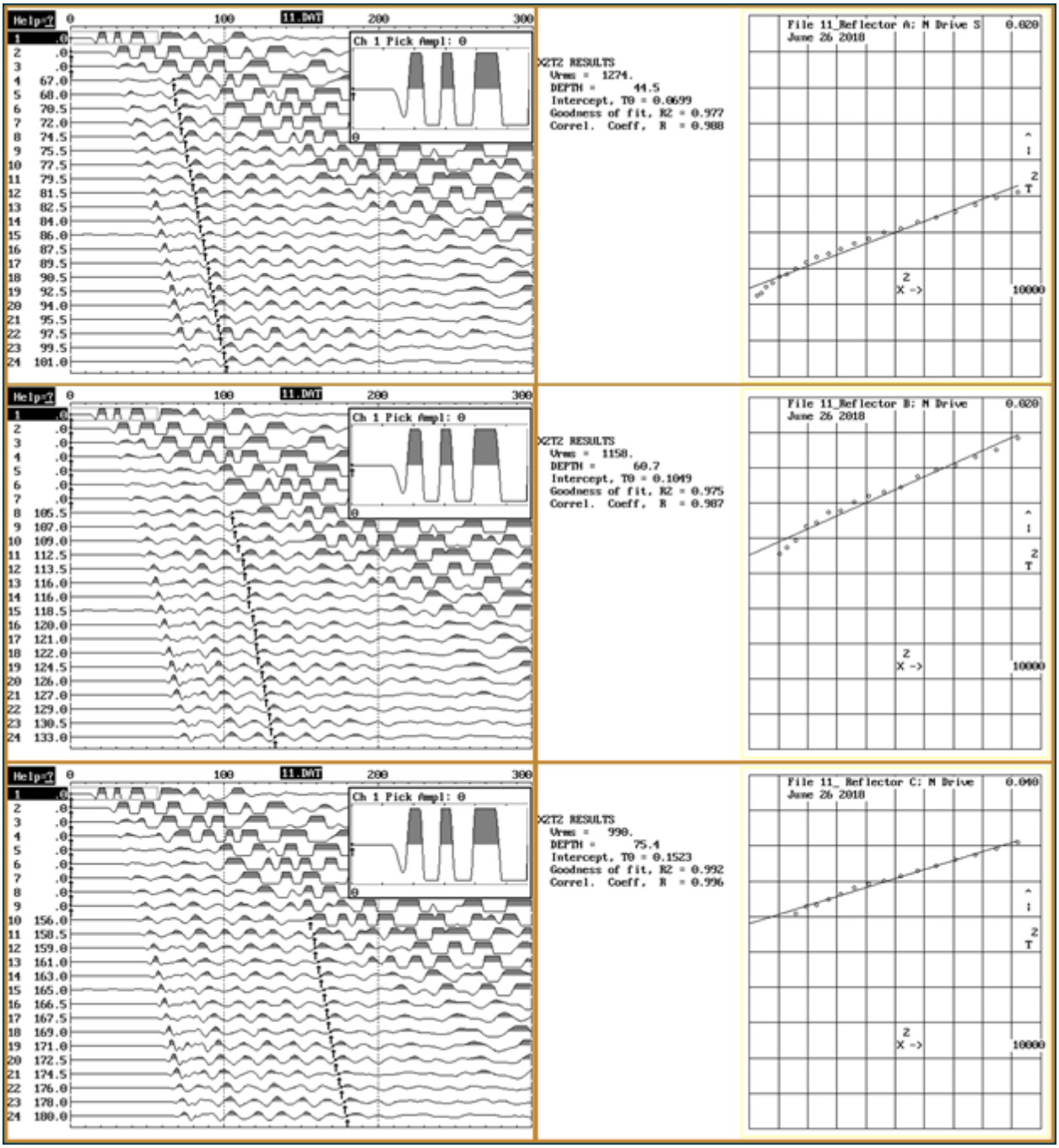

Figure 36. Seismic reflection analysis results for CA-GTS-2. Waveform picks for each reflector are displayed to the left (arrows), and the resulting X^2T^2 values are displayed to the right. These reflector depths are much deeper than previous bedrock surface estimates and may relate to lithology changes within the Coldwater Shale. However, the velocities appear to decrease with depth, and the plots do not have hyperbolic shapes, indicating that they may be reflection multiples.

A vertical electrical sounding (Cal-03) and a seismic survey with vertical and horizontal geophones (SEIS2; CAL02) were conducted at CA-GTS-3 (Figure 37). This site had no borings or direct subsurface information for comparison with geophysical data. This site is also designated as a “nature easement”, so drilling operations were not permitted on the property. The VES survey results show that slight conductive changes occur with depth until reaching a more resistive layer from 16m (52 ft) to 44m (144 ft) (fitting error 5.34%). This model provides a potential bedrock depth of 44m (144 ft). This bedrock depth reasonably agrees with the HVSR calculated bedrock depth of 47m (154 ft) (Figure 38).

The P-wave refraction results from the vertical geophone survey recorded the top of water saturation at 1m (3ft) depth (confirmed in the field when hand-auguring 1m deep holes for Seisgun shotpoints and noting the spread’s proximity to the nearby lake) and also what appears to be a poorly defined boundary between glacial layering at about 10m (33 ft) depth (Figure 39). Although reflection analysis revealed several multiples, reflected waveforms identified on two data files generated a depth solution of 48.2m (158 ft) and 60m (197 ft) (Figure 40). The reflector at 48.2m (158 ft) depth is similar to the HVSR estimate of 47m (154 ft) and the VES modelled depth of 44m (144 ft) (Figure 38). Shear waves analyzed for refraction events from horizontal geophone data (Figure 41) did not provide much insight to depth to bedrock and did not reveal enough layers to calculate average *Vs* estimates.

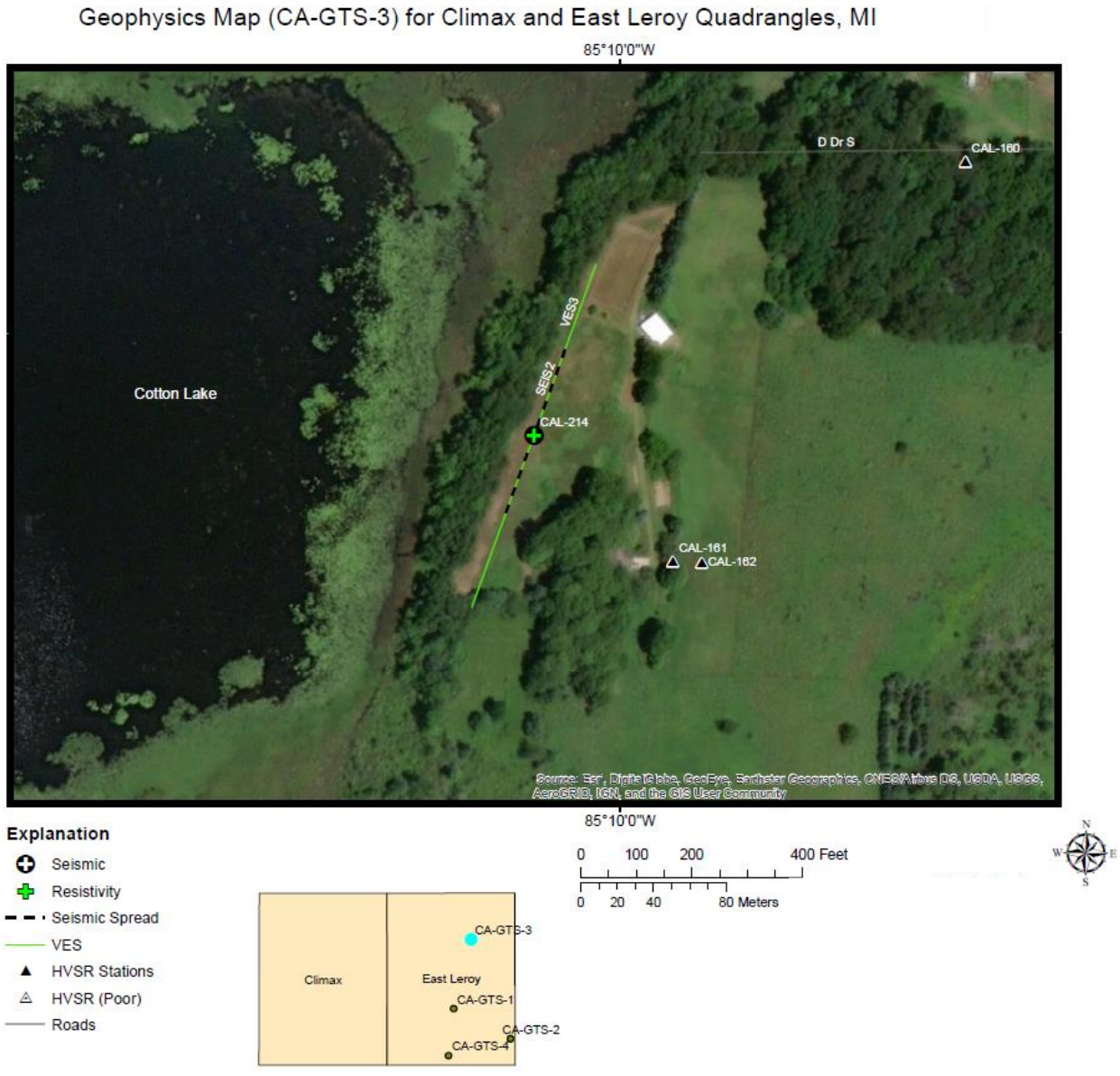

Figure 37. Map of CA-GTS-3 displaying resistivity VES location and seismic survey lines along the edge of a grass field near Cotton Lake. Note the location of several of HVSR stations.

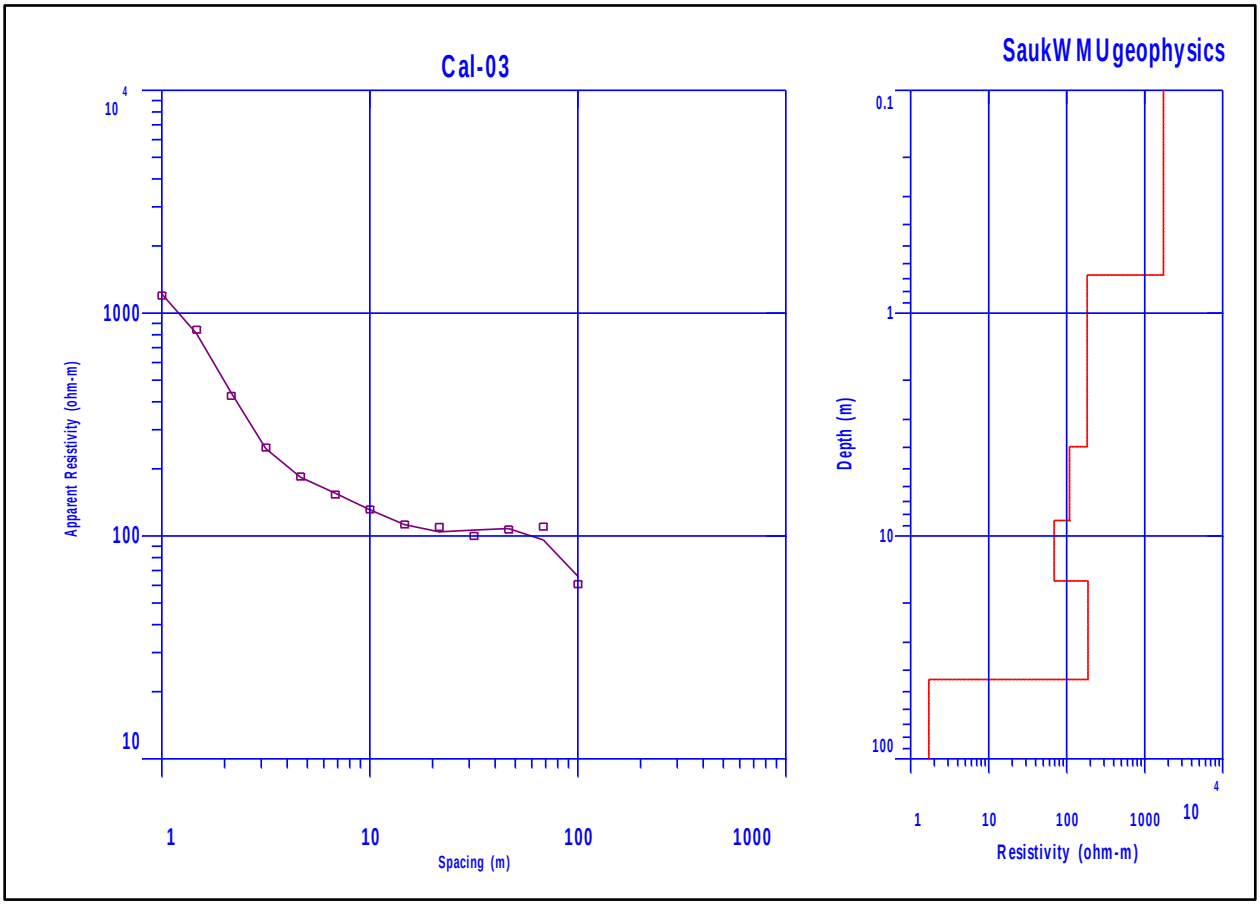

Figure 38. VES results at location CA-GTS-3. The sharp transition to a conductor at 44m depth (at approximately 1.7 Ohm-m) corroborates with the bedrock depth calculated for HVSR station CAL-214. Such a sudden drop in apparent resistivity creates a difficult model fit and may be due to the presence of a near-surface metallic object on site, such as a downed wire fence, that channeled current upon the array expansion rather than the bedrock. However, results are similar to passive and active seismic results (Figure 40).

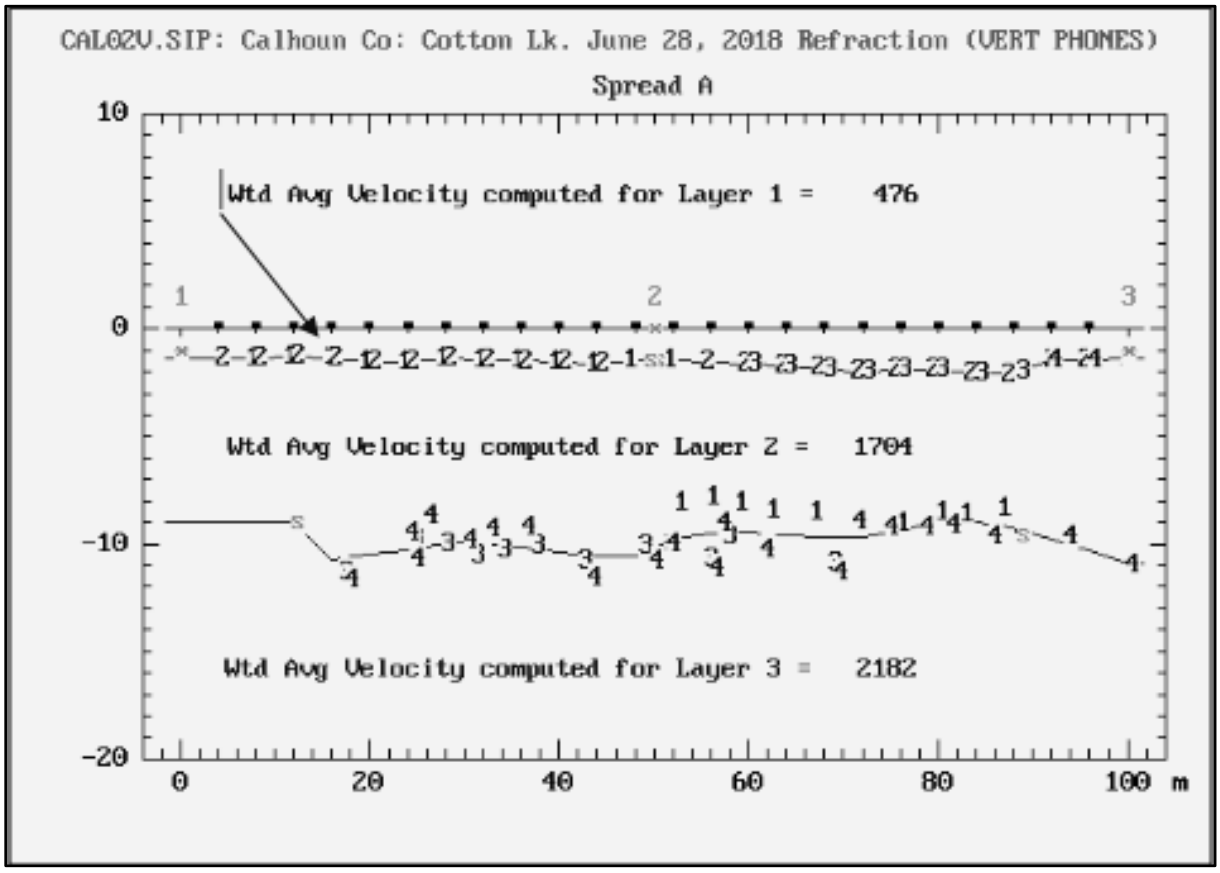

Figure 39. Seismic refraction analysis results for P-waves from CA-GTS-3. Note the uniform depth of approximately 1m to the shallow refractor between layers 1 and 2, which is indicative of the top of water saturation. The boundary between Layer 2 and 3 is likely a result of glacial sediment layering. VES results do not provide significant resistivity variations from 9-11m depth suggestive of bedrock, and HVSR (station CAL-214) results indicate a deeper bedrock depth of 47m (Appendix).

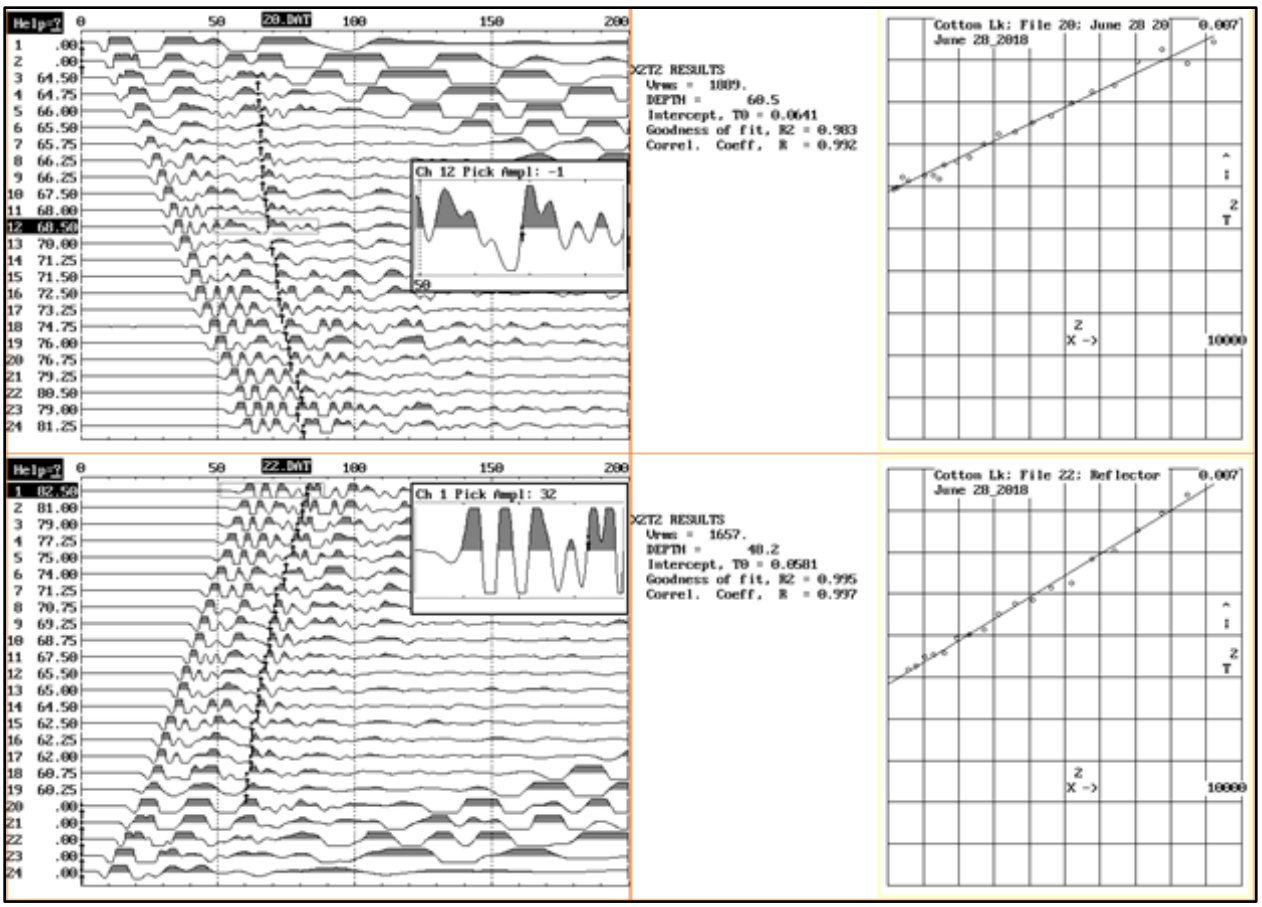

Figure 40. Seismic reflection analysis of P-waves from CA-GTS-3. The same reflection event was tracked at opposite ends of the spread (left) to yield the X^2T^2 solutions (right). This event is likely bedrock, suggesting a depth ranging from 48.2m to 60.5m. Also note that bedrock depth was tagged at 47m at HVSR station CAL-214.

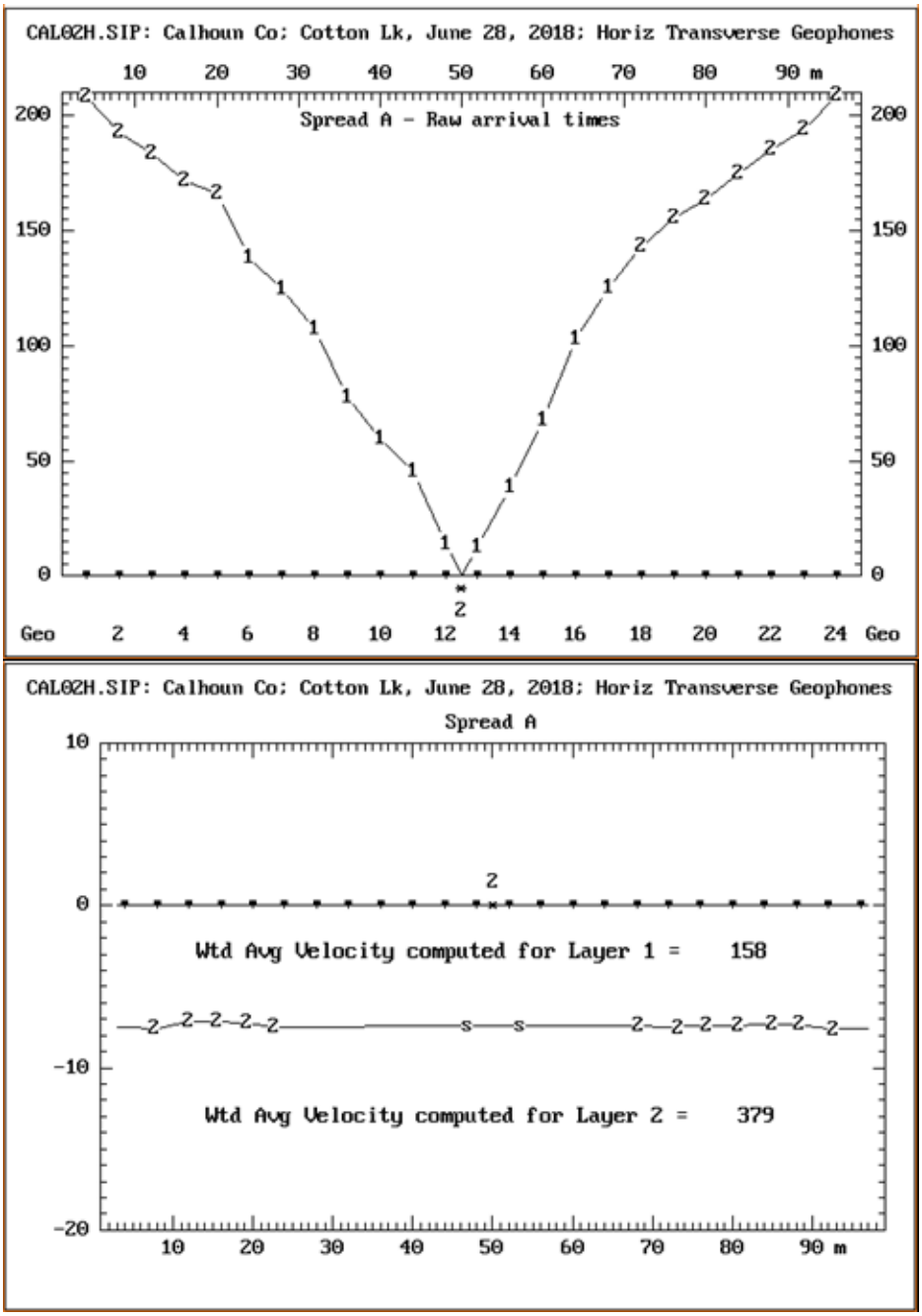

Figure 41. Seismic refraction analysis results for S-waves from CA-GTS-3. **Top:** SIPT2 program time-distance graph with layer assignments. Bottom axis indicates channel number, whereas top axis denotes distance. **Bottom:** Depth model plot. More shotpoints at greater offsets were likely needed to record bedrock refractions. Note that the average shear wave velocity could not be accurately calculated since the thickness of layer 2 is unknown.

Seismic surveys conducted at location CA-GTS-4 utilized horizontal and vertical geophones (SEIS3; CAL03) (Figure 42). Boring CA-F-18-01 was drilled at this site, providing an observable value of 31m (101 ft) for bedrock depth (Figure 28). The P-wave refraction modelling identified the top of water saturation at 3m (10 ft) and a deeper refractor ranging from 33m (108 ft) to 38m (125 ft). Bedrock was determined to be at a depth of 30m (98 ft) estimated from the HVSR station results (Figure 43). One S-wave reflection event yielded depth of 38.2m (125 ft), which is similar to the range of depths provided from the P-wave refraction event (32-38m; 105- 125 ft) (Figure 45). The reflection *Vrms* shear wave velocity between bedrock and the ground surface was then used to calculate independent depth to bedrock at HVSR stations for comparison (Table 4).

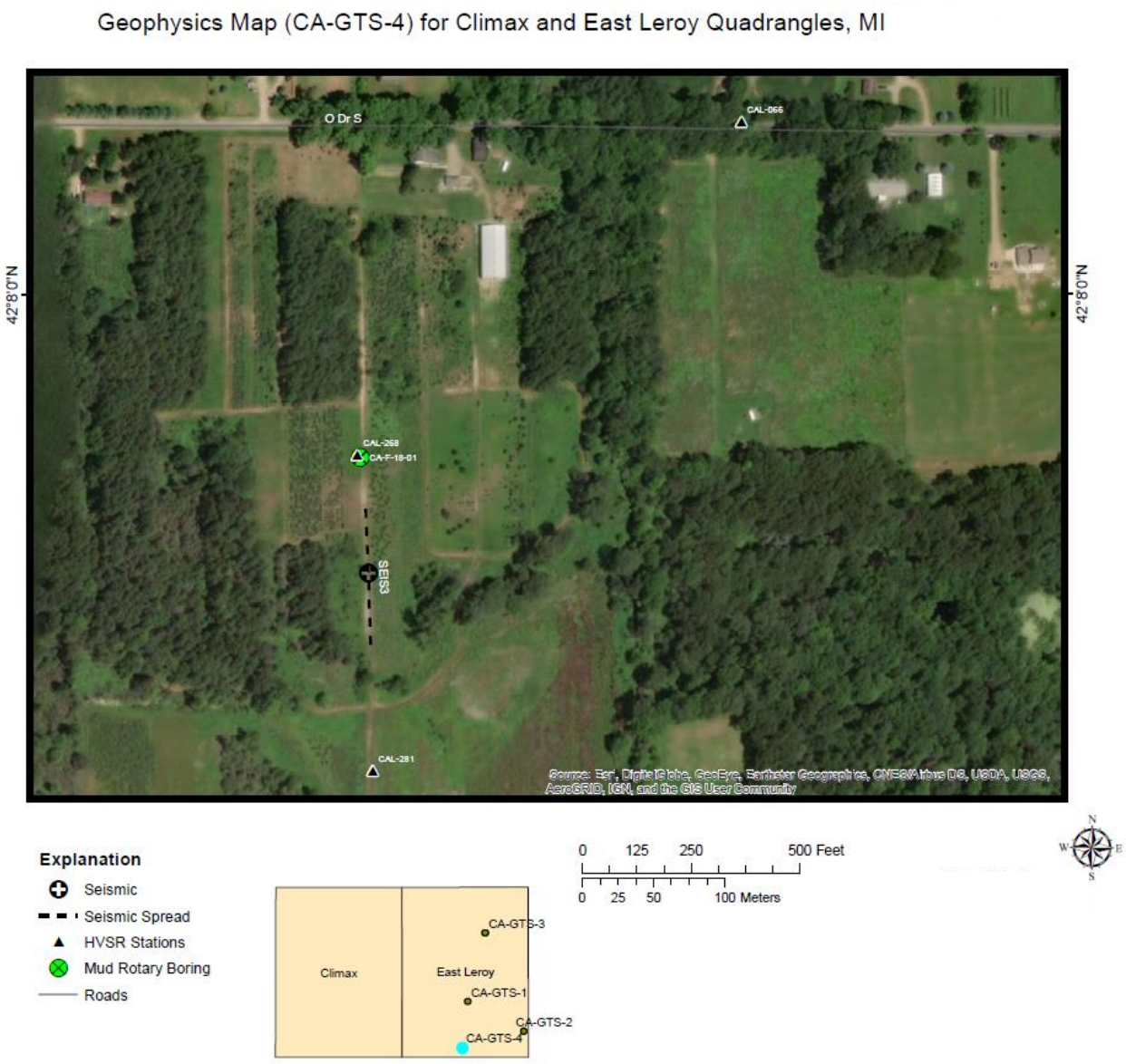

Figure 42. Map of CA-GTS-4 displaying seismic survey line along a dirt road near O Drive S. Note the location several HVSR stations and boring CA-F-18-01.

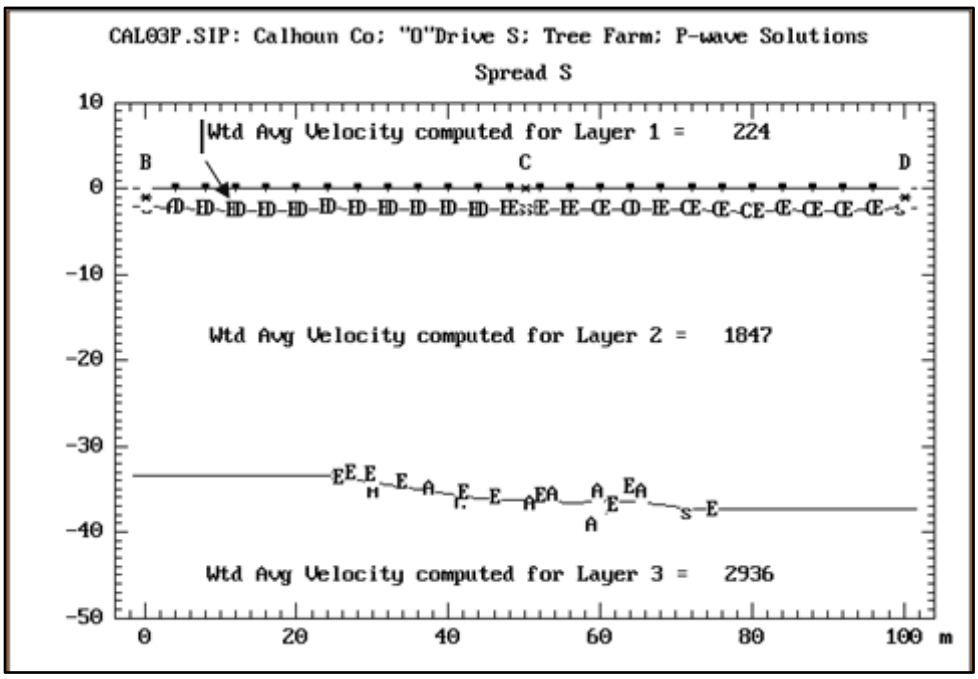

Figure 43. Seismic refraction depth-model plot results for P-waves from CA-GTS-4. The top of water saturation is shallow at approximately 2m depth. Layer 3 is likely bedrock, with an uneven upper boundary ranging from about 33m to 38m at the site. Note that this refractor nearly matches the shear wave reflection event (Figure 45).

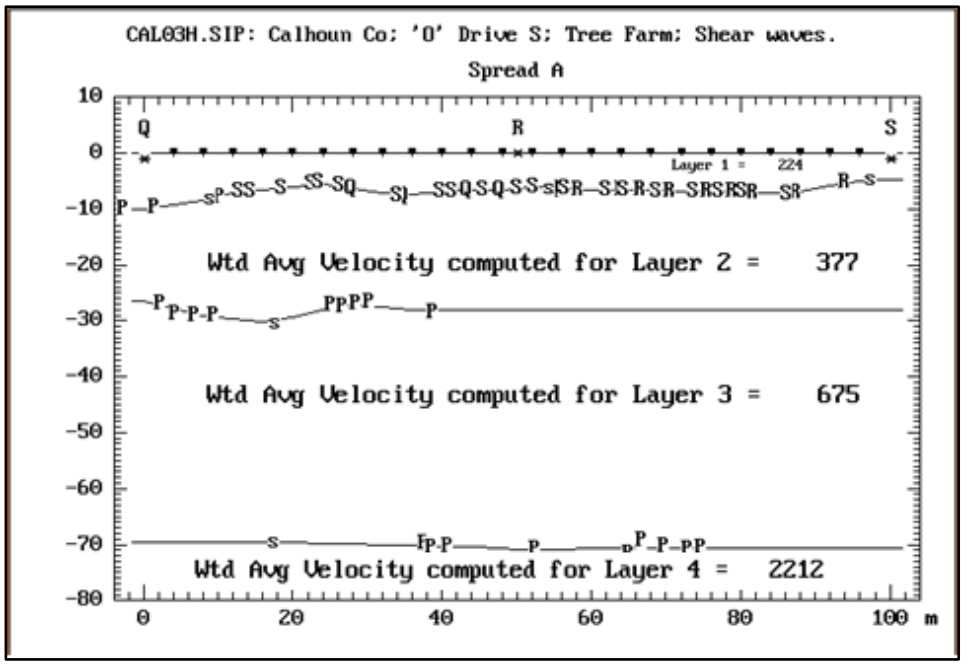

Figure 44. Seismic refraction depth-model plot results for S-waves from CA-GTS-4. Assuming that the shear velocity is similar to the bedrock surface at an approximate depth of 34m (Figures 43 and 45), the calculated average shear wave velocity is 342 m/s.

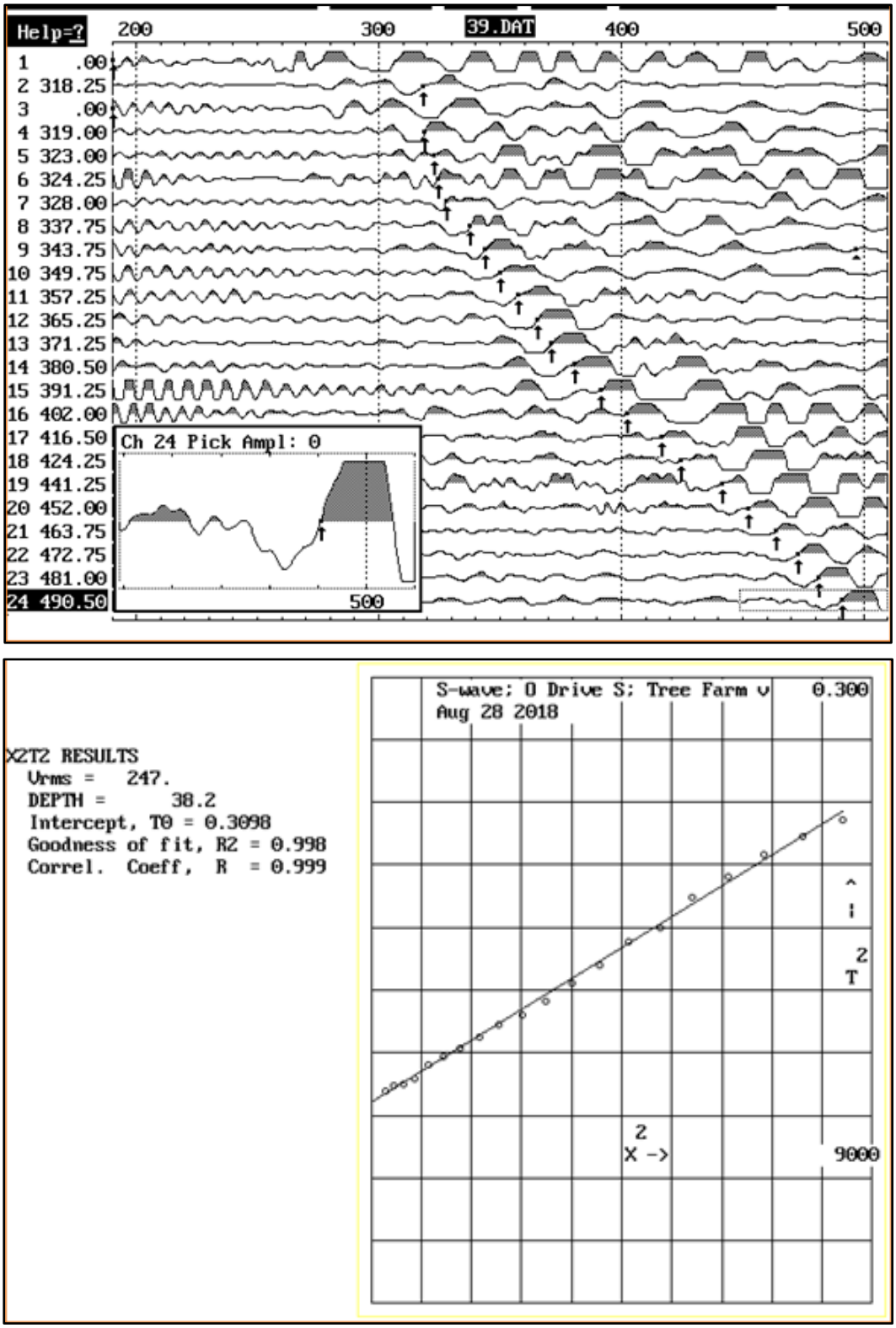

Figure 45. Seismic S-wave reflection at CA-GTS-4. **Top:** Reflection time picks from record; the event begins at approximately 318.25 ns on the record. **Bottom:** X^2T^2 results. Note that the depth to this shear reflector (38.2m) matches deeper P-wave refractor depth (Figure 43).

Table 4. Comparison of bedrock depths (*H*) obtained from using the calculated *Vrms* shear velocity from reflection results and from using the calibration equation at HVSR stations. An *H* value determined from boring CA-F-18-01 is also included for comparison.

Station No.	Fo (Hz)	CA-GTS-4 shear reflection Vs (m/s)	H=Vs/4*fo H1 (m)	Calib. Eq. H2 (m)	Difference (m)	% Diff	Approx. distance from measured Vs (m)	Direction	Boring H (m)	Boring
CAL-268	2.31	247	26.7	29.8	-3.1	0.77	5	W	30.8m	CA-F-18-01
CAL-281	2.78	247	22.2	22.7	-0.5	0.19	180	S		
CAL-056	4.05	247	15.2	13.1	2.1	2.15	360	NE		
CAL-252	3.56	247	17.3	15.8	1.5	1.13	1031	E		
CAL-267	3.06	247	20.2	19.7	0.5	0.24	1150	SE		

CHAPTER V

DISCUSSION

Quaternary Geology & Geomorphology

The HVSR method employed in this study resulted in the discovery of three linear bedrock lowlands that are interpreted as two different categories of bedrock valleys. Valley A and Valley B follow near-parallel NW-SE trends that correspond to either pre-glacial drainage or features created from older Lake Michigan Lobe advances into the study area. Thus, I hypothesize that because the third valley, Valley C, also appears to deeply incise through uplands and is nearly perpendicular to the shallower Valleys A and B, it should be identified as is the youngest of the valleys due to these cross-cutting relationships. Valley C is likely of subglacial origin related to the Saginaw Lobe. Regardless of formation, these valleys are likely excellent aquifers. The intersections of these buried valleys should be ideal locations for high capacity wells. Each of these valleys are buried and show little-to-no expression on the surface (Figure 46). Additionally, bedrock highs occur in similar locations as the local ice marginal position and may correlate with cuestas discovered in past studies. These bedrock highs also appear to have had some influence on modern surface water drainage patterns.

Bedrock Topography: Valleys

Valleys A and B (Figure 20; Figure 47) are interpreted as fluvial valleys that were once part of the area-wide pre-glacial drainage system. Valley A has a relief of 50m (165ft) and is approximately 3.2km (2 miles) wide. Valley B is broad and less defined, with an approximate relief of 60m (197ft) and width of 3.7km (2.3 miles). These NW-SE trending valleys are

perpendicular to the ice flow direction of the Saginaw Lobe, leaving little evidence to support an interpretation as subglacial erosion channels (unless earlier advances of the Lake Michigan Lobe reached this location). Upon glacial advance of the Laurentide Ice Sheet (Saginaw Lobe) into the study area, these valleys did not present favorable meltwater flow paths. Rather, these valleys were likely infilled with glacial ice, becoming buried during multiple ice retreats as a result of meltwater discharge and the melt-out of debris-rich ice within the valley. A pre-glacial origin of these valleys is also supported by the observation that modern surficial streams do not follow similar paths as the subsurface bedrock valley system.

The southeast portion of Valley A has a notable bend that may be a subtle bedrock lowland having some relationship with the north-south trending surficial valley (Figure 47). The surface valley is not directly mimicked by bedrock topography, which suggests either different origins or a complex relationship between tunnel valley formation and bedrock incision. This surface valley occupied by Pine Creek differs from other valleys in the area because of its two distinct trends. The NE-SW trending portions of the surface valley are parallel to ice flow, but do not have bedrock expression. The N-S trending portion of the valley could have been an earlier or minor subglacial meltwater pathway that carved into bedrock. It should be noted that HVSR station profiles in this valley were not collected extensively due to poor field coupling conditions of the Tromino instrument (e.g., swampy conditions, limited access, and constant flowing water). However, stations that were collected with adequate field conditions generally provided clear resonance frequency peaks with low standard deviations. Perhaps some parts of this N-S trending valley were formed by glacial erosion that created a clean bedrock- glacial sediment boundary. This condition would result in an ideal acoustic impedance surface that produces clear, large amplitude resonance peaks recordable by the Tromino measurements. Previous works have

suggested that such N-S trending tunnel valleys are older than those with a NE-SW orientation (Fisher et al., 2005)

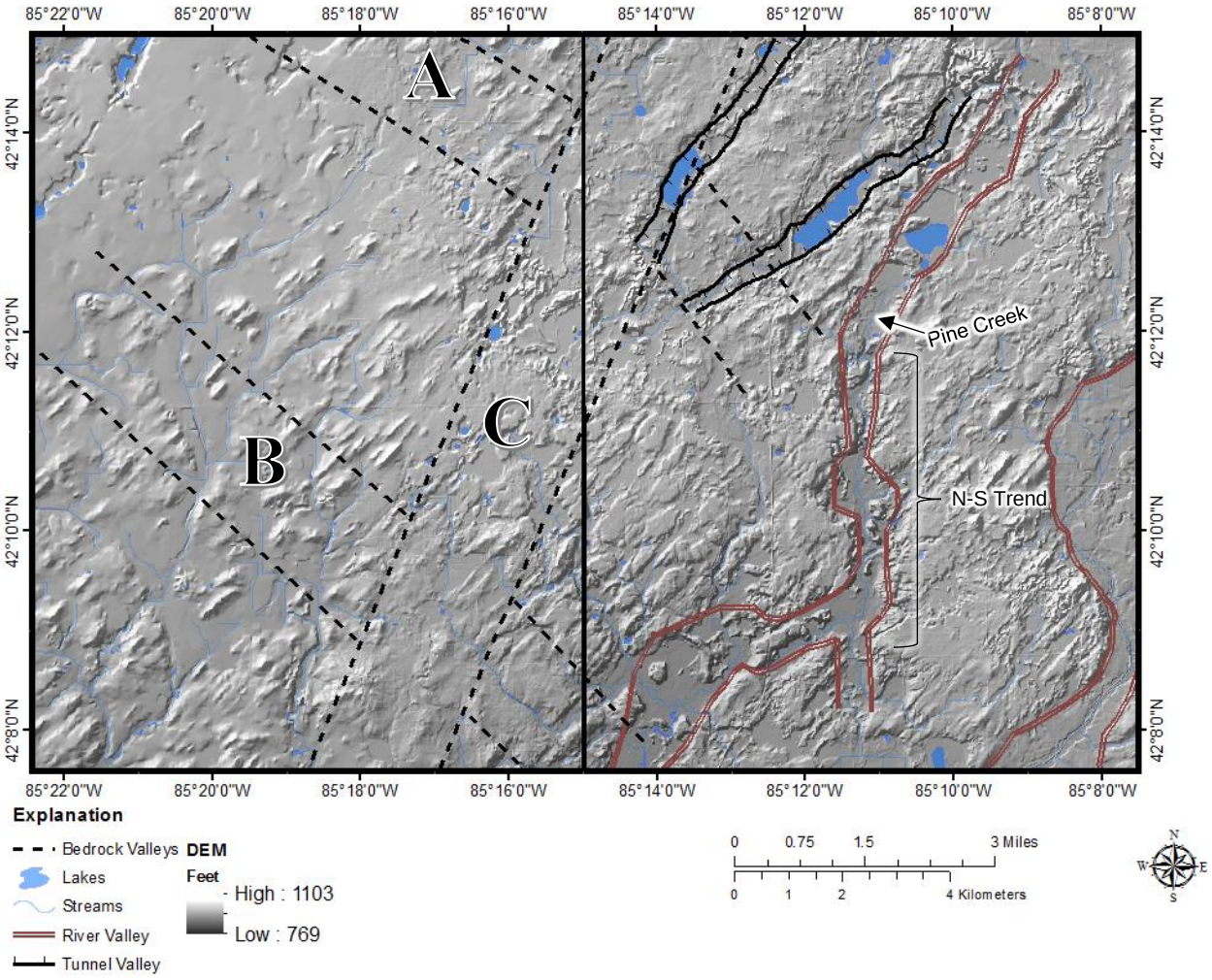

Figure 46. Surface topography DEM with bedrock valleys, open tunnel valleys, and notable river valleys outlined for reference (Figure 47).

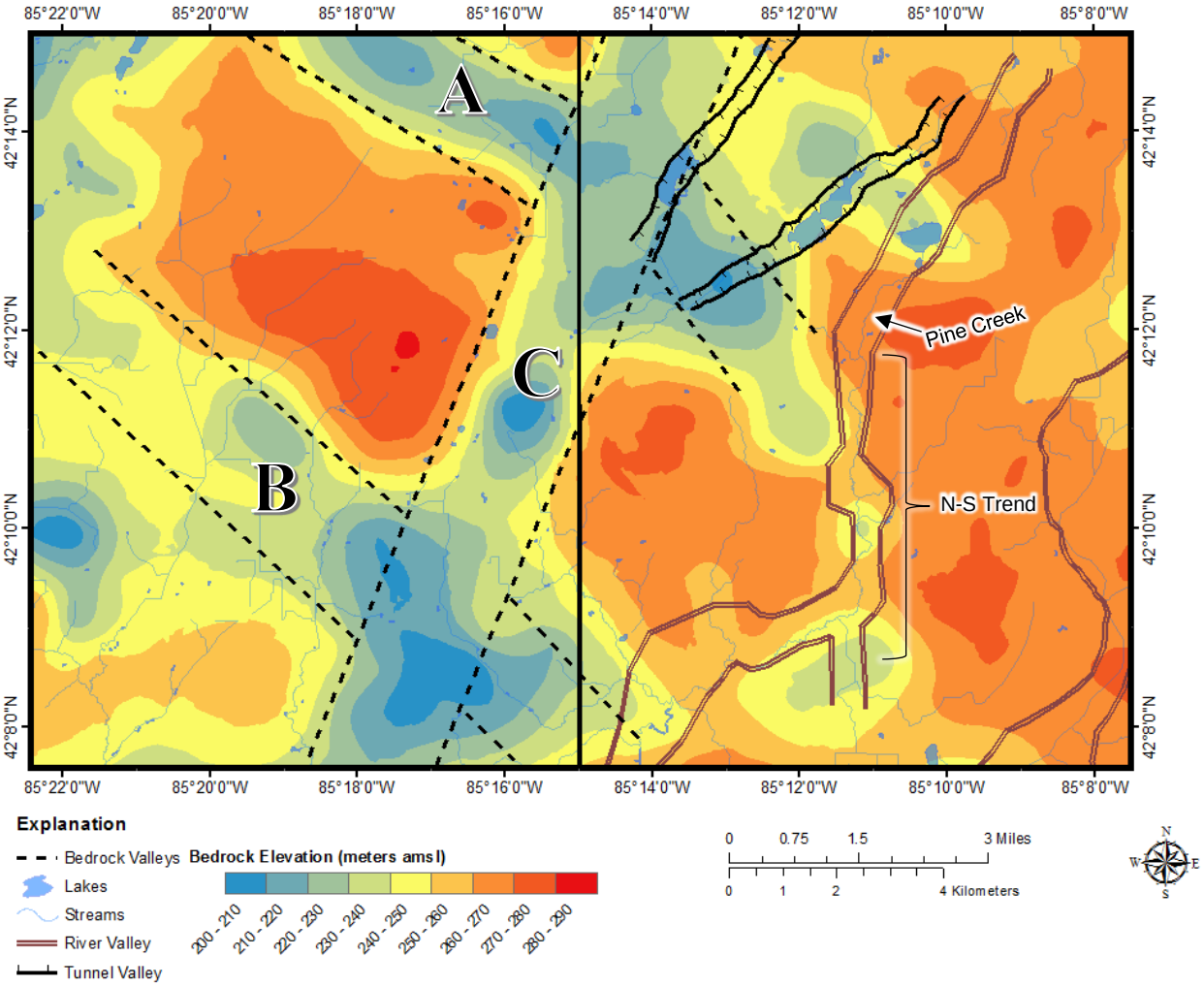

Figure 47. Bedrock topography map displaying bedrock valleys, surficial tunnel valleys, and the deep river valley (Pine Creek) outlined (Figure 46).

Valley C (Figure 20; Figure 47) is most likely a bedrock incised tunnel valley created by subglacial discharge from earlier advances of the Saginaw Lobe. Drumlinized surface features above this tunnel valley suggest that subglacial processes also occurred after valley formation, requiring a subsequent lobe re-advance. Valley C likely extends beyond the limits of the study area. It is an estimated 70m (230ft) deep trough with a width of 2.5km (1.5 miles). This feature displays tunnel valley characteristics such as having an extensive undulating profile, an orientation parallel to ice flow, and an association with other glacial landforms (Kehew et al., 2012). Furthermore, Valley C incises through a notable bedrock high and continues through both Valleys A and B, indicating a cross-cutting relationship that requires glacial processes producing high volume, highly erosive meltwater discharge. The surficial tunnel valleys are also oriented NE-SW, parallel to ice flow (Figure 46). However, these surficial valleys do not incise bedrock, suggesting that the open surficial valleys are more recent in age (Late Wisconsin Glaciation) and that Valley C is an older, pre- Late Wisconsin tunnel valley of the Saginaw Lobe.

Also, linear valleys A, B, and C occur along NE-SW or NW-SE strikes similar to the conjugate orientation of the bedrock fault system in Michigan (e.g., Michigan GeoWebface database). This alignment may be happenstance; however, it may imply that these faults influenced pre-glacial and subglacial flow pathways in some areas. Prior seismic activity in the region further suggests that faults exist in the area, so a relationship could possibly exist between the bedrock valleys and the fault pattern. Further investigation of fault orientation in this area would be needed for confirmation and is beyond the scope of this project.

Bedrock Topography: Uplands

Notable bedrock uplands composed of Coldwater Shale and Marshall Sandstone have been identified in southern Michigan (Rieck and Winters, 1982). Kozlowski (1999) suggested

that a bedrock escarpment trended throughout parts of East Leroy and Union City Quadrangles as a portion of a bedrock high known as the Marshall Cuesta. Furthermore, bedrock mapping to the south of the study area supports the continuation of another cuesta, the Coldwater Cuesta, throughout the Bronson North and Bronson South Quadrangles in Branch County and into the study area (Backhaus, 2018). Backhaus (2018) also marked the top elevation of the cuesta at 949-920 ft (280-290 m) a.m.s.l., which corresponds with the bedrock elevations observed in this study (Figure 48). Bedrock uplands observed in this study most likely continue eastward into the Ellis Corners quadrangle (John Esch, personal communication) and southward into the Union City quadrangle (Kozlowski, 1999). Therefore, the bedrock cuestas (or escarpments) proposed in previous works are likely related to the bedrock highs in this study area, as they follow similar regional trends (Kozlowski, 1999) and reported elevation values (Backhaus, 2018) (Figure 48).

These bedrock uplands coincide with an ice marginal position formed by the retreat of the Saginaw Lobe during the Late Wisconsin glaciation (as mapped by Kehew and Esch, 2014). Ice contact depositional units appear to be related to the formation of the Tekonsha margin and likely coincide with the steep sided scarps of the bedrock uplands mapped in this area. Juxtaposition of an upland scarp in conjunction with ice-marginal positions suggests that the bedrock high impeded forward movement, thus controlling the ice marginal position (Kozlowlski, 1999). This position is also noted by the abrupt termination of the two surficial tunnel valleys, further supporting the interpretation of this location being an ice marginal position (Figure 49).

Furthermore, bedrock highs throughout the area appear to control the surface water drainage. The drainage divide for the area is depicted in Figure 50 as a dashed line. Streams flow either north or south away from the bedrock high, which corresponds to the drainage divide.

Thus, the surface water divide also has a similar relationship with the Tekonsha upland at its ice contact position. However, higher order streams do not appear to follow similar orientations as the bedrock valleys in this region because these bedrock valleys do not have surface expression to influence drainage.

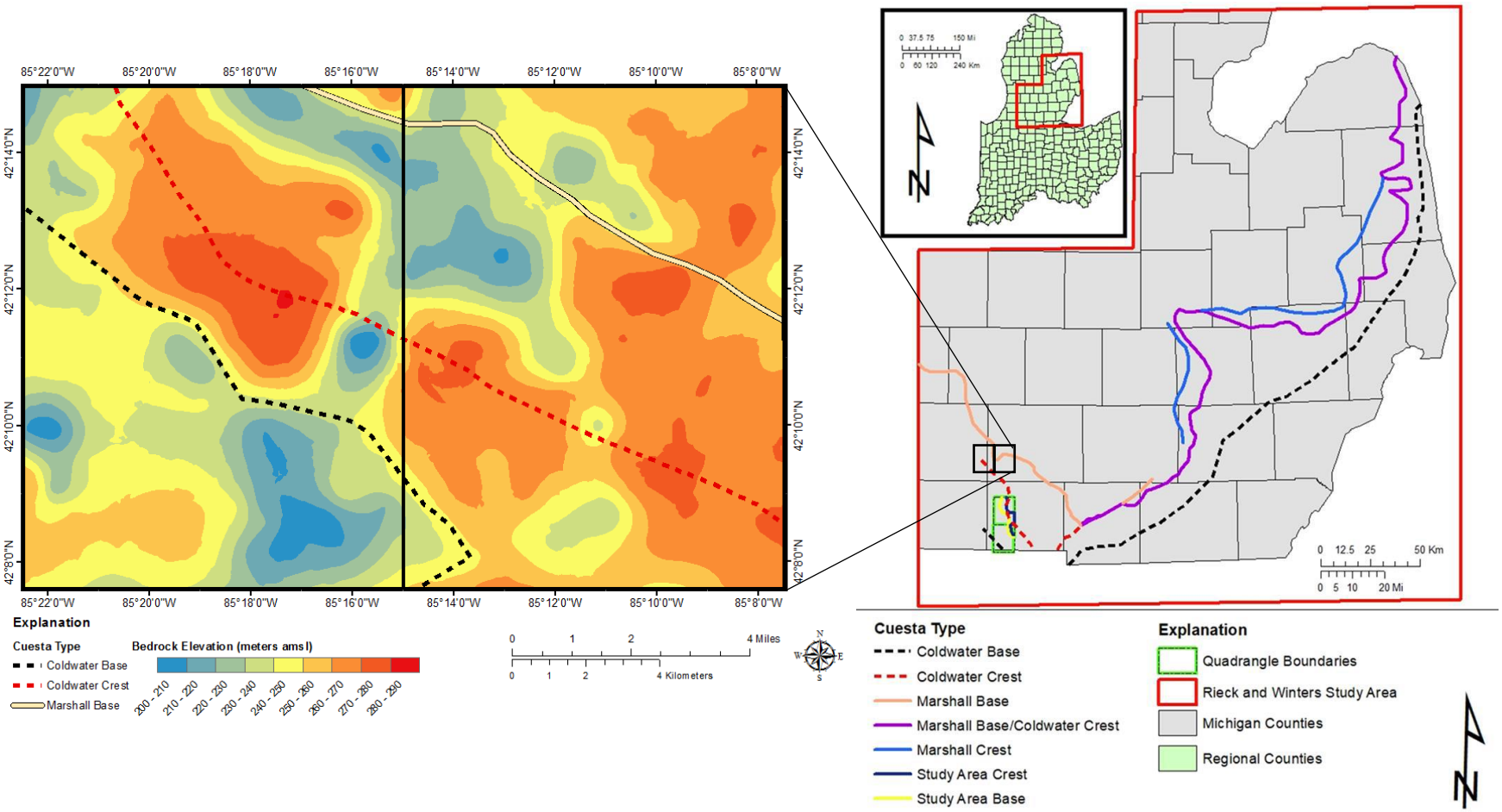

Figure 48. Generalized cuesta features in the study area (left) and projected bedrock cuesta locations in southern Michigan associated with Bronson North and Bronson South quadrangles (right) (regional cuesta map from Backhaus, 2018; adapted from Rieck and Winters, 1982). Note that the cuesta trends of the Marshall base and the Coldwater crest are supported by bedrock topography data collected for this study. An alternative interpretation of the base of the Coldwater Cuesta is also denoted for this study.

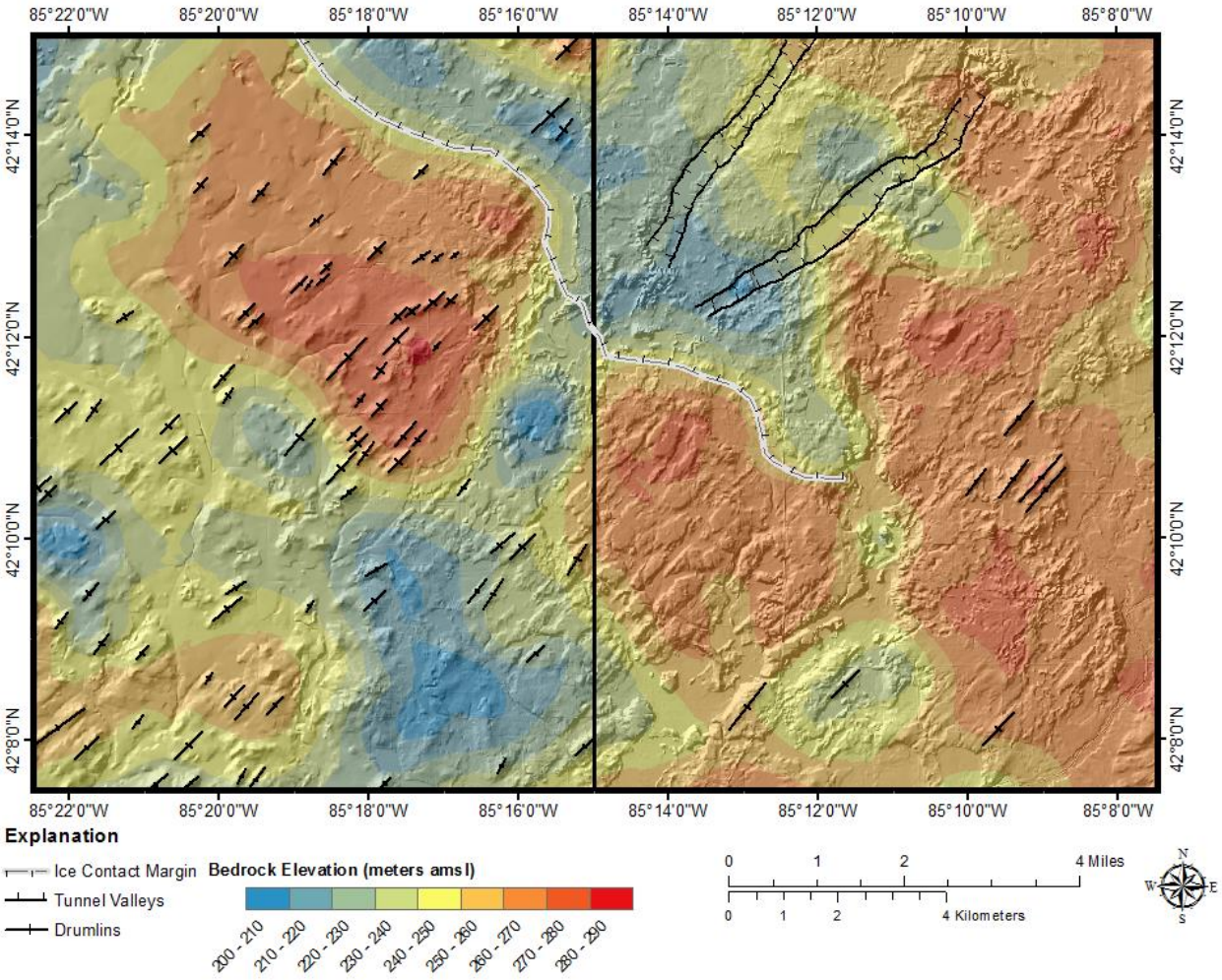

Figure 49. Relationship between bedrock uplands (colored) and surficial Quaternary features. Hillshade overlay provided for emphasis of surface topography. Note the position of the inferred ice margin (hatch marks point towards ice lobe) based on bedrock highs near the termination of surficial tunnel valleys and the presence of glaciofluvial fans along the ice margin.

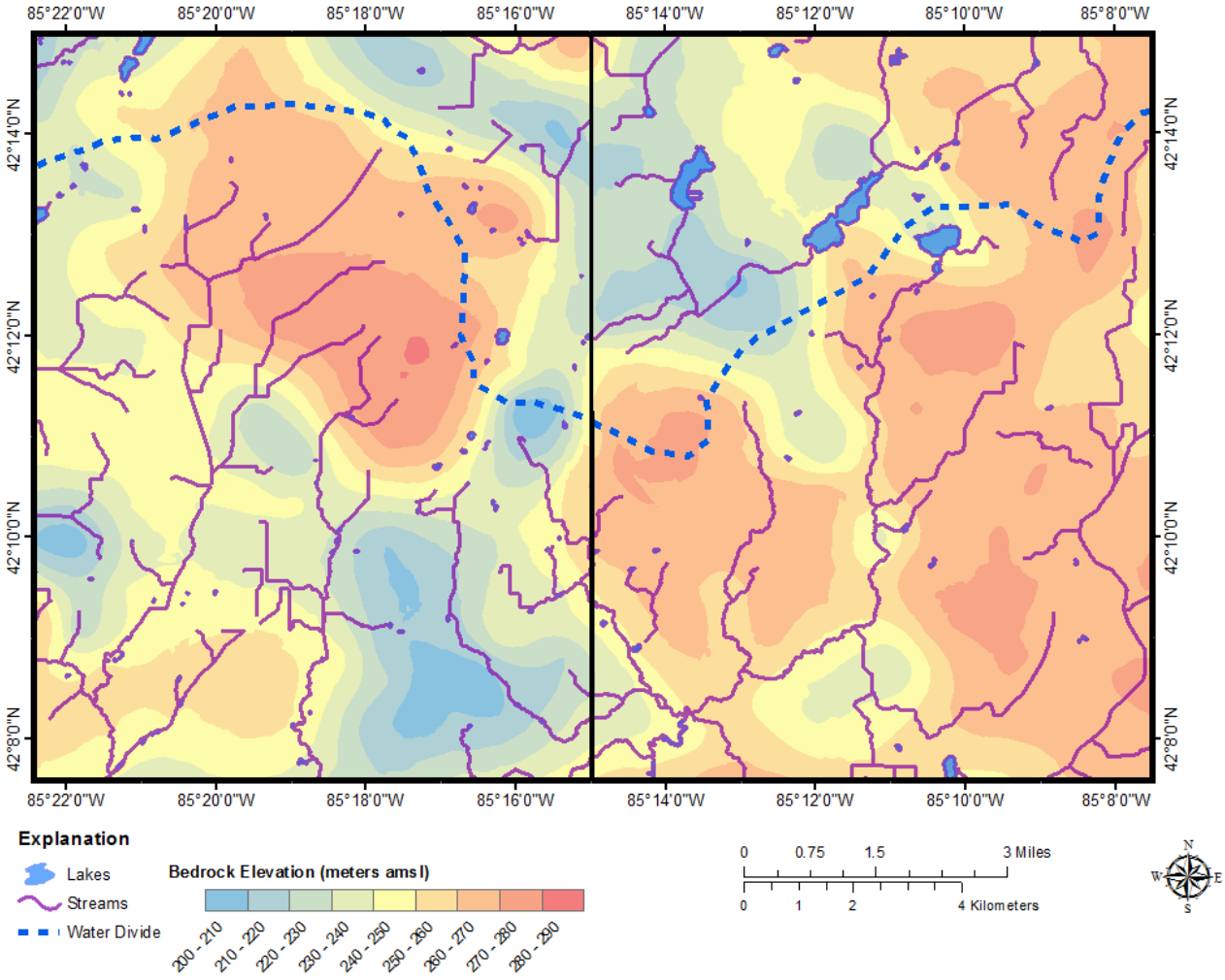

Figure 50. Relationship between bedrock topography and surface drainage in the area. Blue dashed line represents the inferred surface water divide. Note how the divide is closely associated with the bedrock highs.

Geophysics and Subsurface Relationships

Only about 60% of the total HVSR stations were usable in the study. This low success rate proves that this region is one of the most difficult locations in Michigan for the HVSR method, as studies in neighboring counties had greater success (e.g., Feldpausch, 2017, Backhaus, 2018, Seiderman, 2018). Despite having a lower usable sample size than anticipated, a bedrock topography map was created with reasonable resolution when combined with well data (Figure 17). Furthermore, contouring bedrock elevations solely with HVSR data yielded a comparable map (Figure 19), suggesting that experimental data agrees well with actual data from bedrock wells. However, site specific analyses using test borings and other geophysical methods document the complications that arise due to heterogeneous and indiscernible subsurface layering. It should be noted that interpolated contour values are an *estimate* of bedrock depth, especially due to the fact that each resonance peak is associated with a standard deviation that translates into a range of depth uncertainty for each measurement (Appendix, Tables 2 and 3).

HVSR Data and Quality

According to the standards of several previous studies and guidelines (e.g., Chandler and Lively, 2016; SESAME, 2004), most of the data points collected in the East Leroy and Climax quadrangles are considered as “poor” in quality; this is evidenced by frequent multiple, low amplitude peaks contained in the dataset. Although multiple H/V amplitude peaks were often observed, peaks >2.0 amplitude were likely significant in some manner, even if obscured by larger peaks within the H/V record. Ambiguous peaks were assumed to be products of a potentially deeply weathered bedrock - glacial interface and/or an uneven bedrock surface resulting from basal shearing. Both of these factors can contribute to a low shear wave acoustical impedance contrast. Additionally, this area was subjected to multiple advances of a wet based

glacier, which may have irregularly deposited till. Rieck and Winters (1979) noted that the bedrock surface may be "rugged" along the southern extent of the cuestas in this region, which may have contributed to an uneven bedrock surface at distal edges of the uplands, resulting in poor HVSR readings. Stations that exhibited non-directional, sharp, high amplitude peaks denote locations of high acoustic impedance contrasts that may correspond to: (1) unweathered/ evenly sheared shale bedrock, (2) subcropping of dense Marshall Sandstone, (3) limestone or dolomite units in the Coldwater Shale, or (4) dense consolidated till layers within the glacial drift. Although unconsolidated or weathered bedrock is likely the cause of a majority of the poor readings in the southwestern portion of the study area, results are otherwise inconclusive regarding spatial trends of HVSR data quality (Figure 13). Results suggest that data obtained in the study area often violated the simple two-layer model (soft homogeneous drift over hard bedrock) and fundamental assumptions of the HVSR method.

Despite subsurface irregularities, HVSR calculated depths should be considered reasonable due to the similarity with the local calibration equation for this study and those developed for HVSR surveys in other areas in SW Michigan (Figure 51). Applicability of the local calibration curve for this area is dependent upon the accuracy of pre-existing subsurface data from water well borings. Additionally, calibration curve development for this project was difficult not because of lack of bedrock control, but due to a lack of clear, quality HVSR records from other calibration stations. Many stations intended for calibration were either too poor in quality or were removed as significant outliers on the calibration curve.

Repeated and concurrent readings further show that HVSR station quality can change spatially and temporally (Table 2 and Table 3; Figure 27). Some of the f_0 values obtained from these stations did not agree with the original value. Stations obtained simultaneously had

comparable results overall, with variations that could be attributed to operator error or soil/coupling conditions. Repeated stations generally had a greater error, which was likely due to the variation in the strength of background noise at the tested locations throughout time. Results suggest that HVSR stations are not strictly repeatable, but similar results adequate for regional studies can be obtained.

The constant validation of HVSR bedrock depths through comparison with water wells in this study prove that passive seismic may be a poor method to solely rely on when determining geological structures without bedrock control. Comparing depth values to well logs, employing other geophysical methods, and taking repeat quality control measurements may be needed to validate data in similar study locations. Supporting data are especially needed in areas with a low bedrock-drift acoustic impedance contrast. Variable glacial lithology combined with uneven, weathered, and/or unconsolidated bedrock contacts create additional difficulties for obtaining accurate HVSR data and making valid interpretations.

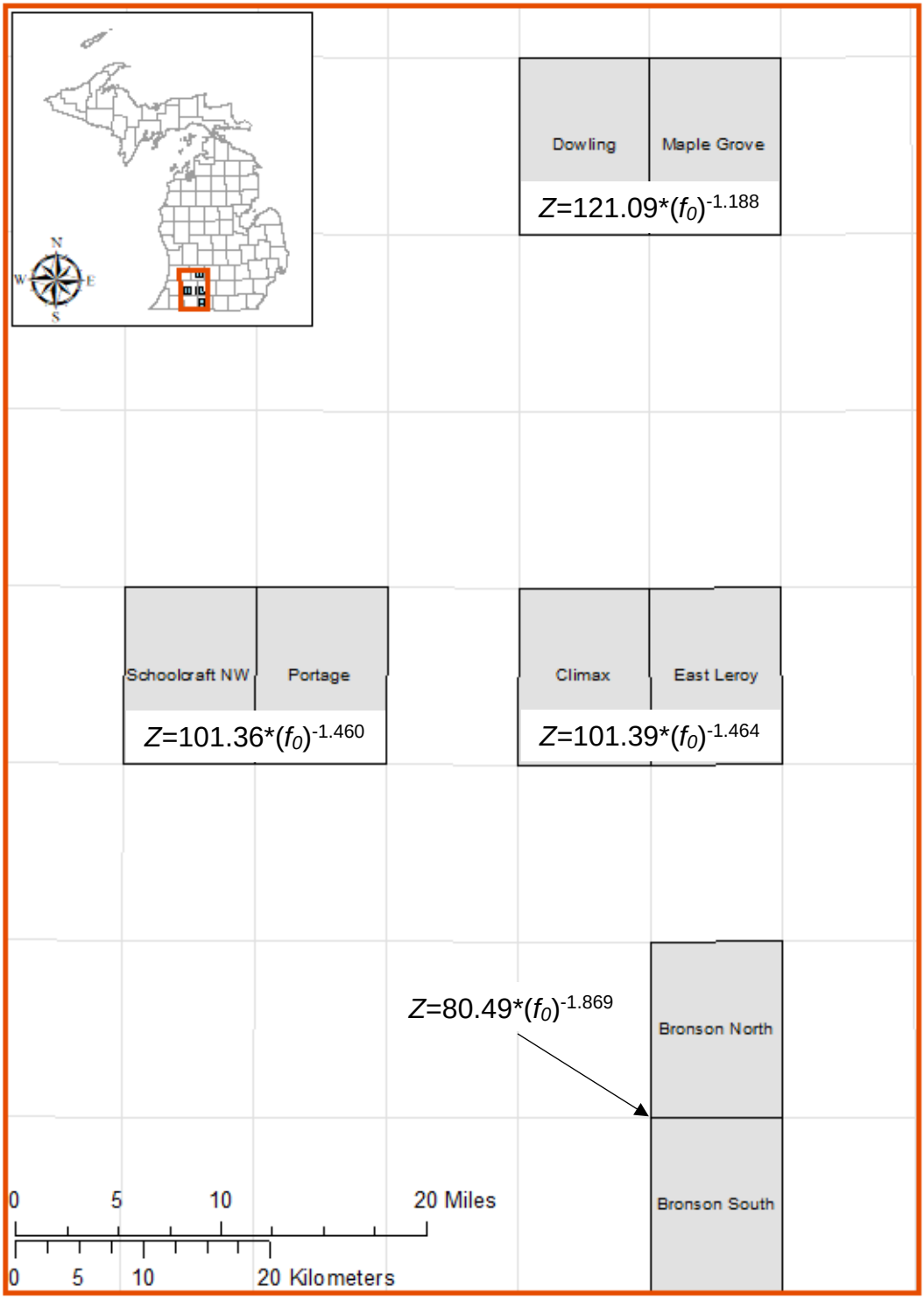

Figure 51. Spatial distribution of power law regression curve equations for published HVSR surveys in southwestern Michigan (Feldpausch, 2017; Seiderman, 2018; Backhaus, 2018) and this study. Note the similarity to Schoolcraft NW and Portage quadrangles, which suggests similar subsurface geologies that yield similar shear wave velocities. The statewide calibration equation as of 2018 is $Z=108.19*(f_0)^{-1.393}$ (John Esch, personal communication).

Relationship Between HVSR and Other Methods

HVSR data were compared to conventional resistivity and active seismic results for analysis of near-surface conditions and validation of the passive seismic method performed in poor subsurface conditions. Resistivity (VES) was the least accurate method when using the Schlumberger sounding technique due to the need to have prior knowledge of some parameters, such as layer thickness and resistivity, to produce a geologically reasonable model. Additionally, the field data supported more than one model due to layer equivalence, so a range of ratios (for conductive layers) or product of thicknesses and resistivities (for resistive layers) could be fit "accurately" upon inversion. Moreover, some subsurface glacial layers may be too thin or may have low-contrast resistivities that will cause them to be suppressed. Extensive, larger scale resistivity work would be needed for a given site to spatially characterize potential bedrock contact depths and morphologies (e.g., Thomason et al., 2018). Conventional VES resistivity methods performed for this project would be inefficient for regional mapping of bedrock but were useful when analyzing site specific comparisons with HVSR. This method should be used with caution due to glacial drift heterogeneities and variable electrical properties.

Active seismic reflection and refraction surveys are mostly compatible with HVSR results and with data from borings. The combination of P- and S- wave refraction/reflection data produced comparable results to HVSR, resistivity, and well information. However, dense, high-velocity zones overlying low velocity units could create a seismic model that misrepresents the subsurface. For example, the seismic refraction method requires that layer velocities must increase with depth. Reflection analysis also allows one to interpret bedrock surfaces, but deep reflectors and multiples in the dataset can mislead seismic analysis.

Horizontal geophones aptly provided shear wave velocities for use in calculating HVSR bedrock depths independently from the calibration curve. Depth to bedrock at site CA-GTS-4 was calculated using the average shear velocity (Equation 1 – Chapter 2 in this study). This analysis produced similar bedrock depths as those calculated from the calibration equation (Table 4). Some discrepancy in these results may be due to error in shear wave picking or to inadequate shear wave detection at the site. The bedrock depth calculated directly from field- derived shear wave velocity was fairly consistent with bedrock depth calculated from the calibration equation. The differences in these values were inconsistent when comparing each station analyzed with the same shear wave velocity, with varying differences further away from the site where the shear wave velocity was determined. This spatial variation is likely caused by changes in shear velocity due to subsurface lithology changes. Additional experimentation at many different sites is needed to investigate the relationship between using independently calculated shear velocities and using a regional regression law equation. Note that active seismic *Vs* is specific to the particular site, whereas the calibration equation provides a regional average *Vs* that varies with thickness.

Drilling results further indicate the difficulty in identifying the "true" bedrock surface in the area. Both holes drilled during this project contained a similar lowermost unit; lower lithologies were a dense, grey clay mixed with shale chips that became more prominent with depth. This lowermost unit transitioning into bedrock could be the hard, grey clay-rich till glacial unit described in previous works regarding the lithologies of Landsystem 1 (Kehew at al., 2017). However, a deeply weathered Coldwater Shale would also exhibit similar texture, color, and other similar sample descriptions from mud rotary cuttings. Bedrock shearing during glacial advance may possibly create such a heterogeneous basal unit consisting of a mixture till and

local bedrock clasts. Additionally, conversations with well drillers indicate that drillers often describe this unit as shale bedrock in locations outside the study area, therefore water well logs may be biased and should be used with caution. These factors all contribute to a problematic subsurface layer that exhibits multiple qualities that could be indicative of either glacial till or bedrock. The HVSR method provided an indication of the uppermost dense unit at the drilling locations, which implies that the HVSR method likely identifies the top of the first competent bedrock layer in some parts of the study area.

Comparisons of cross-sections based on either HVSR or gravity data indicate similar valley morphologies and depths (Figures 21, 22, and 23). Bedrock units are typically denser than the overlying glacial sediments. This density contrast creates a variation in gravitational force intensity force at the local scale; anomalies tend to coincide with varying subsurface densities and can be detected by careful gravity surveys (Carmichael and Henry, 1977). However, tunnel channels not incised into bedrock can sometimes be difficult to delineate if the density of their glaciofluvial fill material is similar to the surrounding drift. Thus, infilled valleys that do not penetrate bedrock will not be detected using gravity methods. This caveat is also true for the HVSR method. Farnsworth (1980) performed several gravity survey lines (employing approximately ¼ mile station spacings) near Battle Creek, MI and East Leroy to delineate buried river valleys and regional trends. Both gravity anomaly interpretations from Farnsworth (1980) and the HVSR data presented in this study agree well. These results further establish the occurrence of incised bedrock valleys within the study area and proves that the HVSR method is verifiable by other geophysical methods, even in challenging subsurface conditions.

Industry 2D seismic data included several kilometer-long profiles that qualitatively agree with HVSR derived bedrock surfaces (Figures 21, 24, 25, and 26). The most striking correlation

is observed across cross-section line D – D' (Figure 25), where both passive and active seismic survey results display buried tunnel and bedrock valleys. Cross-section lines C – C' (Figure 24) and E – E' (Figure 26) demonstrate variability and difficulty in detecting the drift-bedrock interface. In such cases, HVSR results provide potentially better bedrock topography resolution. Detecting the boundary between glacial drift and bedrock was challenging for every method employed in this study.

Additional Notes:

Vibroseis survey

During field data collection, I encountered a geophysical crew performing a 3D seismic survey using a Vibroseis energy source. Several HSVR stations were unknowingly recorded while the Vibroseis survey was active. Such records showed a series of rhythmic seismic disturbances; the Vibroseis sweep length was 12 seconds total with 6 second pauses between 6 sweep stacks at a single location. The vibrator sweep went from 4 to 128 Hz; however, the upper range of frequencies could not be recorded because the Tromino was set to sample at 128 Hz. Therefore, any signals above 64 Hz (the Nyquist frequency) were aliased to lower apparent frequencies. Stations affected by such events were identified by the presence of a low to high frequency sweep of 12 seconds in the raw record; amplitudes of the vibrated frequency decreased with distance away from the Vibroseis source. About fifteen HVSR stations exhibited this pattern. Five of the affected stations were repeated when the survey crew was not working in the area (included in Table 3: CAL-253, CAL-254, CAL-257, KAL-513, and KAL-548). The active energy source did not appear to compromise HVSR data quality but may in fact have served as a local energy source, which improved the overall seismic energy over a wide frequency band for the Tromino recording.

Persistent Peak in HVSR Records

A broad peak, nearly constant in frequency ranging from 1.0-1.15 Hz, was commonly observed throughout the study area (example, Figure 52). This peak was typically not the resonant peak, and such signals were not observed in previous studies in the region (Backhaus 2018, Feldpausch 2017, Seiderman, 2018). Additionally, the source almost always appeared as a unidirectional source. Such a low frequency peak would yield deeper than expected bedrock depths, which never appeared to represent the true bedrock surface when compared to nearby wells. These low frequency peaks appeared with no correlated relationship to time, elevation, or notable proximity to anthropogenic sources. The signal may represent a deeper acoustic impedance contrast within the Paleozoic section such as the base of the Coldwater Shale, but one would then expect a gradual decrease in resonant frequency (increase in depth) toward the NE due to Michigan Basin stratigraphy. Further analysis of this oddity awaits a future study.

Earthquake Events

Distant, large magnitude, shallow earthquakes may have contributed to some poor readings and unique frequency peaks, as surface waves can travel vast distances with ground motion for many hours and aftershocks from these tremors can adversely affect passive seismic data quality (Sauck, 2017). Shallow (~ less than 20km epicenter depth) earthquakes of magnitude 6.0 or greater around the world were identified using the USGS earthquake database to compare with days when HVSR stations were collected (U.S. Geological Survey, 2019) (Figure 53 and Table 5). No notable correlation was observed between earthquakes and station quality; SESAME scores, processing notes, field notes, and general usability of potentially affected stations were typical of HVSR stations collected in general. (i.e., data did not display any earthquake-generated signal that degraded station quality) (Appendix).

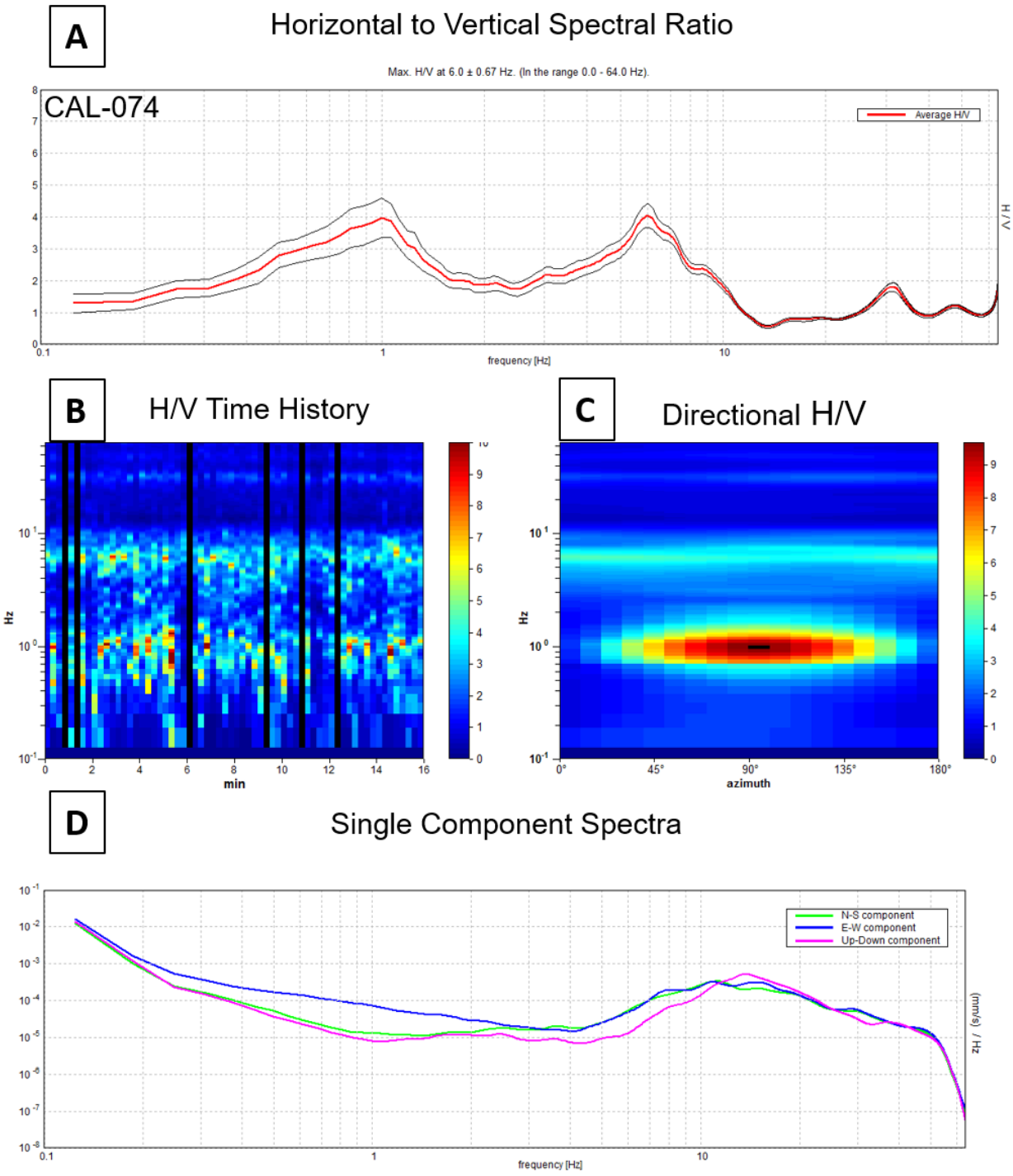

Figure 52. Example of HVSR data exhibiting the broad ~1 Hz peak (CAL-074). **A.** 6.0 Hz was chosen as the resonance peak by Grilla, but the 1 Hz peak is just as significant **B.** H/V time history for the 1 Hz peak is irregular **C.** Particle motion for the 1Hz peak is very strongly biased to E-W, while 6 Hz is uniform at all azimuths. **D.** A broad"eye" is prevalent on the single component spectra at 1 Hz but is otherwise not characteristic of bedrock signature. Note that this example is an extreme case, as other records with this ~ 1Hz peak show a broader, lower amplitude peak (Figure 9).

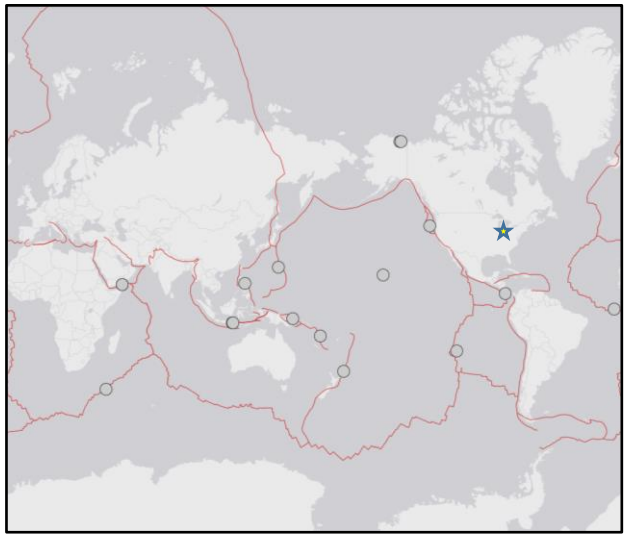

Earthquake Location	Date	Time	Latitude	Longitude	Depth (km)	Magnitude
Prince Edward Islands region	4/19/2018	21:09:17.000Z	-42.7797	42.1877	10	6
Easter Island region	5/2/2018	06:32:49.020Z	-24.2723	-111.6328	10	6
19km SSW of Leilani Estates, Hawaii	5/4/2018	22:32:54.650Z	19.3182	-154.9997	5.81	6.9
64km NNW of Pandan, Philippines	5/5/2018	06:19:05.040Z	14.5708	123.9192	18	6.1
177km SSW of Kokopo, Papua New Guinea	5/9/2018	07:57:54.950Z	-5.8822	151.7836	9	6
South of the Kermadec Islands	5/18/2018	01:45:31.460Z	-34.5886	-178.4143	11	6.1
159km SSE of Sayhut, Yemen	7/15/2018	13:09:16.470Z	13.8484	51.7170	10	6
137km SSE of Sayhut, Yemen	7/15/2018	01:57:19.410Z	14.0625	51.7365	10	6
Central Mid-Atlantic Ridge	7/23/2018	10:35:59.590Z	-0.2994	-19.2520	10	6
5km WNW of Obelobel, Indonesia	7/28/2018	22:47:38.740Z	-8.2395	116.5080	14	6.4
73km SSW of Kaktovik, Alaska	8/12/2018	21:15:01.841Z	69.5205	-144.3602	1.7	6.1
90km SW of Kaktovik, Alaska	8/12/2018	14:58:54.286Z	69.5619	-145.2998	2.2	6.3
251km SE of Iwo Jima, Japan	8/16/2018	18:22:53.360Z	23.4226	143.3187	20	6.3
15km N of Golfito, Costa Rica	8/17/2018	23:22:24.950Z	8.7791	-83.1527	15	6.1
4km SW of Belanting, Indonesia	8/19/2018	04:10:22.640Z	-8.3366	116.5993	16	6.3
78km E of Lakatoro, Vanuatu	8/21/2018	22:32:26.470Z	-16.0315	168.1428	9	6.5
272km WNW of Bandon, Oregon	8/22/2018	09:31:45.530Z	43.5637	-127.7166	10	6.2
64km SSE of Tanaga Volcano, Alaska	8/23/2018	03:35:12.270Z	51.3500	-177.7604	20	6.3

Figure 53. Worldwide earthquake events of magnitude 6.0 or higher that occurred during field collection (April 13, 2018 – August 22, 2018). See Table 5 for a list of HVSR stations that were recorded on days of earthquake events. Data and map generated from USGS earthquake catalog database (2019). Star denotes study area location in southwestern Michigan.

Table 5. HVSR stations and observations recorded during high magnitude earthquake events.

Date	Station No.	Lat -Deg N	Long-Deg W	Record Notes	Overall Notes	SESAME	Used in Map?
5/5/2018	CAL-044	42.152409	-85.208613			7	Y
	CAL-045	42.152033	-85.218564		small creek nearby- but peak frequency gives reasonable BR depth	9	Y
	CAL-046	42.151494	-85.23127	compound	weak, BR peak uncertain	7	N
	CAL-047	42.151731	-85.246567	1 decent peak with smaller compound peaks		6	Y
	CAL-048	42.15144	-85.254788	directional noise, higher amplitudes	noisy,some peaks may be due to wind	6	Y
	CAL-049	42.150849	-85.261475	broad: 1.06-3.32Hz. Trough at 4.2hz	weak, directional noise	6	N
	CAL-050	42.150755	-85.268878	compound	weak, directional noise	6	Y
	CAL-051	42.150159	-85.275551	compound	tractor noise, directional, unreasonable peaks. Trough at 4.4hz significant, BR uncertain	6	N
	CAL-052	42.155248	-85.276379	compound @ high frequency	Strong peak, but noise directional. BR uncertain	7	N
	CAL-053	42.1583402	-85.285292	peak3 weak	cows; tactor noise	7	N
	CAL-054	42.165394	-85.285615		tractor noise; peaks strong, but BR uncertain	7	N
	CAL-055	42.160925	-85.197338		gas pipeline nearby	7	Y
	CAL-056	42.158853	-85.20465		next to well; people and dogs walking nearby: analyzed .9-56 Hz	5	Y
	CAL-057	42.158637	-85.205826		underground structure?	7	Y
	CAL-058	42.166414	-85.206733	compound		7	Y
5/9/2018	CAL-086	42.188507	-85.175227	compound	nearby creek. BR pick unclear	7	N
	CAL-087	42.188469	-85.164806		strong wind gusts; same location as CAL-088	6	N
	CAL-088	42.188469	-85.164806		wind protection; same location as CAL-087	6	Y
	CAL-089	42.188513	-85.156655		weak	9	N
	CAL-090	42.186149	-85.146574	high frequency peak @ 44.18	possible pipeline around 200' away	9	Y
	CAL-091	42.174155	-85.150817	steady between 1.63-3.5Hz		5	N
	CAL-092	42.182733	-85.146827	compound	possible pipeline	6	N
	CAL-093	42.17543	-85.140669	light peak @ 5.8 Hz	possible pipeline	9	Y
	CAL-094	42.178164	-85.126158		nearby CAL-95	4	N
	CAL-095	42.17938	-85.126568	compound	north of CAL-95	8	Y
	CAL-096	42.174067	-85.156246	compound	broad low frequency peak; pipeline nearby (no marker)	7	Y
	CAL-097	42.173998	-85.167856	triple peaks	possible pipeline (no marker)	6	Y
	CAL-098	42.170657	-85.172726		Trough at ~8.8 to 9.1; 4.4hz chosen for 1/2 trough for peak 3.	6	Y
	CAL-099	42.179819	-85.17824		weak; Fo seems reasonable	6	Y
7/23/2018	KAL-500	42.13833	-85.382583	trough at 3.77 Hz and 16.14 Hz	logging/chainsaw running to the south (high frequency peak at 44Hz)	9	N
	KAL-501	42.144093	-85.387132	trough at 24.99 Hz	peak at 12.81 with 20 second window; planting soft	9	N
	KAL-502	42.144033	-85.380357	compound; another peak at19.1hz. Broad to 1.7hz and 2.2hz	poor overall, near wetlands	6	N
	KAL-503	42.144071	-85.37152		wetlands nearby	7	Y
	KAL-504	42.144074	-85.361718	compound, weak	small nearby stream	6	N
	KAL-505	42.144025	-85.350461	Poor high and low freq. peak. Trough at 4.08hz. (1/2= 2.04hz fo?)	poor coupling?	6	N
	KAL-506	42.144121	-85.343958	Low ampl peaks, trough at 4.12hz; another peak at 6.85hz		7	N
	KAL-507	42.144067	-85.33728	trough @18.74hz		7	N
	KAL-508	42.145865	-85.324269	poor, compound. Trough at 4.1hz.	weak vibroseis (up component). Quiet	7	N
	KAL-509	42.147645	-85.314256	poor, compound	weak vibroseis (up component). Quiet	5	N
	KAL-510	42.146993	-85.305008	trough at 4.1hz	weak vibroseis	9	Y
	KAL-511	42.154799	-85.305069	1.07hz; trough at 14.21hz	weak vibroseis	9	N
	KAL-512	42.15818	-85.295601	Compound	weak vibroseis	7	N
	KAL-513	42.148321	-85.295247		weak vibroseis	9	Y
	KAL-514	42.142895	-85.295125	Compound		7	Y
	KAL-515	42.127514	-85.304486	plateau from 1.0-1.8		7	Y
	KAL-516	42.122054	-85.304204	broad from 1.19 to ~1.63hz	high freq. peak probably from mowing to the south	8	Y
8/17/2018	CAL-275	42.16513	-85.184404		East Leroy Gravel Pit, 100m south of CAL-027	9	Y
8/22/2018	CAL-276	42.224245	-85.233613	poor	poor	5	N
	CAL-277	42.232788	-85.178847	poor	poor	6	N
	CAL-278	42.248275	-85.177146			9	Y
	CAL-279	42.166558	-85.168456		~400' E of CAL-280	9	N
	CAL-280	42.166601	-85.16949	compound	~400' W of CAL-279	7	N

CHAPTER VI

CONCLUSIONS

Bedrock elevations and drift thicknesses throughout the East Leroy and Climax quadrangles were mapped using the HVSR method and were compared to other geophysical methods to find three buried bedrock valleys and a prominent bedrock upland feature. Two bedrock valleys were interpreted to be of pre-glacial origin, whereas one was interpreted as a buried tunnel valley. None of these valleys exhibited notable surface expression, other than a unique bedrock pattern observed beneath the Pine Creek river valley in the East Leroy Quadrangle. Results prove that the presence of a surficial valley does not imply the presence of a bedrock valley, and *vice versa*. Additionally, bedrock topographic uplands controlled the Saginaw Lobe ice marginal position in this area. This influence continued to control the development of modern drainage patterns in the region by establishing the surface water divide that runs across the two quadrangles. These basements uplands are correlatable to the Marshall and Coldwater Cuestas.

This project showcases the strengths and limitations of passive seismic, active seismic, and electrical resistivity methods combined with bedrock control in a region overlain by relatively thin drift, and where the bedrock surface was heavily altered by fluvial and glacial erosion. Active seismic methods employing horizontal geophones successfully complemented passive seismic data and provided independent *Vs* values for depth calculations. The Schlumberger VES method also provided comparable results to HVSR data at individual points, but some knowledge of the subsurface was necessary to fix some layer parameters to produce an appropriate, plausible model. Cross-sections reproduced from two prior gravity surveys and three industry 2D seismic lines also yielded similar results to HVSR data by displaying similar

relationships between the surface and bedrock topography. This study also suggests that the HVSR method can be employed without relying on other geophysical methods for validation. The self-reliance of the HVSR method extends to challenging subsurface conditions that may violate the assumptions critical to obtaining an ideal, simple two-layer case or having a strong acoustic impedance contrast at the bedrock boundary. The HVSR method is valid as long as the study site has some independent bedrock depth control.

Mud rotary test borings provided insight into the subsurface at two locations, but the bedrock contact was indistinct due to a poorly lithified bedrock-and-drift interface. The lowermost unit may be a clay-rich till or diacmicton mixed with glacially sheared Coldwater Shale debris, further complicating subsurface interpretations. Bedrock depths determined from passive seismic analysis likely identified the uppermost portion of the dense, unweathered bedrock in some cases, while at other locations the lack of a strong shear wave acoustic impedance contrast led to HVSR plots with no usable peaks. The heterogeneous subsurface and the highly variable bedrock qualities of this portion of Calhoun and Kalamazoo Counties likely contributed to the cause of many of the poor HVSR readings.

Overall, the passive seismic method provided a low cost and rapid approach to producing bedrock topography maps in post glacial landscapes covered by drift. The HVSR method is usable provided that numerous and reliable control wells are available as a control standard to eliminate poor HVSR records from the dataset. Conducting passive seismic surveys in areas of glacial drift is thus an effective method to utilize when exploring for buried bedrock valleys that constitute valuable aquifers for residential use and agriculture. Findings also contribute to new insights into the rather complex glacial history of this area.

REFERENCES

Backhaus, K. J., 2018, Geologic mapping of the Bronson North and Bronson South 7.5-Minute Quadrangles, Branch County, Michigan: Masters Thesis, Western Michigan University, Kalamazoo. 3432.https://scholarworks.wmich.edu/masters_theses/3432.

Blake D. R., and Nash, T. A., 2018, Mapping bedrock topography and drift thickness of the preglacial Teays River within the Anna Seismic Zone, Ohio: Columbus, Ohio, Ohio Department of Natural Resources, Division of Geological Survey Open-File Report 2018-2, 18p.

Burger, H. R., Sheehan, A. F., Jones C. H., 2006, Introduction to applied geophysics: exploring the shallow subsurface: W. W. Norton & Company, Inc., New York, p. 554.

Carmichael, R. S., and Henry, G., 1977, Gravity exploration for ground water and bedrock topography in glaciated areas: Geophysics. v. 42, no. 4, p. 850-859

Chandler, V. W., and Lively, R. S., 2014, Evaluation of the horizontal-to-vertical spectral ratio (HVSR) passive seismic method for estimating the thickness of Quaternary deposits in Minnesota and adjacent part of Wisconsin: Minnesota Geological Survey Open File Report 14-01, 52 p.

Chandler, V. W., and Lively, R. S., 2016, Utility of the horizontal-to-vertical spectral ratio passive seismic method for estimating thickness of Quaternary sediments in Minnesota and adjacent parts of Wisconsin: Interpretation, v. 4, no. 3, p. SH71-SH90.

Clayton L., Attig J. W., and Mickelson D. M., 1999, Tunnel channels formed in Wisconsin during the last glaciation. *In* Mickelson D. M. and Attig J. W. Glacial Processes Past and Present, Geological Society of America Special Paper 337, p. 69-82.

Colgan, P. M., Vanderclip, C. A., and Braunschneider, K. N., 2015, Athens subepisode (Wisconsin Episode) non-glacial and older glacial sediments in the subsurface of southwestern Michigan, USA: Quaternary Research, v. 84, p.382-397.

Curry, B., Loope, H. M., Lowell, T. V., Wang, H., Thomason, J., Caron, O., J., 2016, Recent changes to the time-distance diagram of the Lake Michigan lobe (Michigan Subepisode, Wisconsin Episode): Geological Society of America, 50th Annual Meeting of the North-Central Section. Geological Society of America Program 48 (5): p. 16.

Dodson, R.L., 1985, Topographic and sedimentary characteristics of the Union Streamlined Plain and surrounding morainic areas: PhD Dissertation, Michigan State University, East Lansing.

Dorr Jr., J.A., Eschman, D.F., 1979, Geology of Michigan: The University of Michigan Press, Ann Arbor, MI, 476pp.

Erber, N., 2016, Differentiating Saginaw from Huron-Erie Ice Lobe meltwater deposits in South Central Michigan using longitudinal profiles, grain size analysis, and lithology: Masters Thesis, Western Michigan University, Kalamazoo, 87p.

Farrand, W.R., and Bell, D.L., 1982, Quaternary Geology of Southern Michigan map: Lansing, Michigan, Michigan Department of Natural Resources, Geological Survey Division, scale 1:500,000.

Farnsworth, J. W., 1980, Relationship of gravity anomalies to a drift filled bedrock valley system in Calhoun County Michigan: Masters Thesis, Western Michigan University, Kalamazoo.

Feldpausch, S., 2017, Gravity and passive seismic methods used jointly for understanding the subsurface in a glaciated terrain: Dowling and Maple Grove quadrangles, Barry County, Michigan: Masters thesis, Western Michigan University, Kalamazoo.

Fisher, T.G., and Taylor, L.D., 2002, Sedimentary and stratigraphic evidence for subglacial flooding, south-central Michigan, USA: Quaternary International, v. 90, p. 87–115, doi:10.1016/S1040-6182(01)00095-7

Fisher, T.G., Taylor, L.D., and Jol, H.M., 2003, Boulder-gravel hummocks and basal till wavy contacts: Products of subglacial meltwater flow beneath the Saginaw Lobe, south-central Michigan, U.S.A.: Boreas, v. 32, p. 328–336, doi:10.1080/03009480301820.

Fisher, T.G., Jol, H.M., and Boudreau, A.M., 2005, Saginaw Lobe tunnel channels (Laurentide ice sheet) and their significance in south-central Michigan, USA: Quaternary Science Reviews 24, 2375-2391

Fujita, K. and Sleep, N.H., 1991, A re-examination of the seismicity of Michigan: Tectonophysics, v. 186 (1–2), p. 75–106.

Gabriel G., Kirsch R., Siemon B., Wiederhold, H., 2003, Geophysical investigation of buried Pleistocene subglacial valleys in Northern Germany: Journal of Applied Geophysics, v. 53, 4., p. 159-180.

Gao, C., Shirota, J., Kelly, R. I., Brunton, F. R., Haaften, S. V., 2006, Bedrock topography and overburden thickness mapping, southern Ontario: Ontario Geological Survey, Miscellaneous Release – Data 201.

Gillespie, R., Harrison III, W. B., Grammer, G. M., 2008, Geology of Michigan and the Great Lakes: Cengage Books, Michigan Geological Repository for Research and Education & Western Michigan University, 39 p.

Gosar A. and Lenart A., 2010, Mapping thickness of sediments in the Ljubljana Moor basin (Slovenia) using microtremors: Bulletin of Earthquake Engineering, v. 8, p. 501.

Hansel, A. K., and Johnson, W. H., 1996, Wedron and Mason groups. Lithostratigraphic reclassification of deposits of the Wisconsin Episode, Lake Michigan Lobe area: Illinois Geological Survey, Bulletin 104, p. 116.

Heider, F., 1982, Gravity profile over a buried valley in northeastern Kansas: Kansas Geological Survey, Open-file Report, M.S. research project, 55 p.

Hinze W., Kellogg, R. L., Merritt D., 1971, Gravity and aeromagnetic anomaly maps of the southern peninsula of Michigan: Department of Natural Resources Geological Survey Division Report of Investigation 14, p. 1-11.

Hooke, R. L., Jennings, C. E., 2006, On the formation of the tunnel valleys of the southern Laurentide ice sheet: Quaternary Science Reviews, v. 25, i. 11-12, p. 1364-1372.

Howell, P. D., and van der Pluijm, B. A., 1990, Early history of the Michigan basin: subsidence and Appalachian tectonics: Geology, v. 18, p. 1195–1198.

Høyer, A. S., Jørgensen F., Sandersen, P.B.E., Viezzoli A., Møller I., 2015, 3D geological modelling of a complex buried-valley network delineated from borehole and AEM data: Journal of Applied Geophysics, v. 122, p. 94-102.

Ibs-von Seht, M. I. V, and J. Wohlenberg. 1999, Microtremor measurements used to map thickness of soft sediments: Bulletin of the Seismological Society of America 89:250–259.

Jennings, C.E., 2006, Terrestrial ice streams - a view from the lobe: Geomorphology 75, 100-124.

Jørgensen F., Sandersen P., 2006, Buried and open tunnel valleys in Denmark – erosion beneath multiple ice sheets: Quaternary Science Reviews, v. 25, p. 1339–1363.

Kearsey T., Whitbread, K., Arkley, S., Morgan, D., Boon, D., Raines, M., 2018, How accurate is your model between boreholes? Using shallow geophysics to test the best method to model buried tunnel valleys in Scotland, UK: Illinois State Geologic Survey Open-File Series 2018-1, p. 39.

Kosinski, W.K. and Kelly, W.E., 1981, Geoelectric soundings for predicting aquifer properties: Groundwater, v. 19, p. 163-171.

Thomason J., Larson, T.R., Ismail, A., Sargent, S., 2018, Characterizing glacial sediments and features in northeast Illinois using electrical resistivity and seismic-reflection profiling: *in* Kehew, A.E., Curry, B.B., 2018. Quaternary Glaciation of the Great Lakes Region: process, landforms, sediments, and chronology: Geological Society of America Special Papers, v. 530, p 233.

Kehew A.E., Nicks L.P. and Straw W.T., 1999, Palimpsest tunnel valleys: evidence for relative timing of advances in an interlobate area of the Laurentide Ice Sheet: Annals of Glaciology, 28:47-52.

Kehew, A.E., Beukema, S. P., Bird, B.C. and Kozlowski, A.L. 2005., Fast flow of the Lake Michigan Lobe of the Laurentide Ice Sheet: evidence from sediment-landform

assemblages in southwestern Michigan, USA: Quaternary Science Reviews 24 2335-2353.

Kehew, A. E., Esch, J. M., 2013, Surficial geology of the Climax 7.5 Minute Quadrangle, Calhoun and Kalamazoo Counties, Michigan: Surficial Geologic Map Series SGM-13-03, scale 1:24000

Kehew, A.E. and Esch, J.M., 2014, Surficial geology of the East Leroy 7.5 Minute Quadrangle, Calhoun County, Michigan: Surficial Geologic Map Series SGM-14-01, scale 1:24000.

Kehew, A. E. and Kozlowski, A.L. 2007, Tunnel channels of the Saginaw Lobe, Michigan, USA, *in*, Johannsson, P., and Sarala, P. (eds.) Applied Quaternary research in the central part of glaciated terrain, Geological Survey of Finland, Special Paper 46, pp. 69-77.

Kehew, A.E., Esch, J.M., Kozlowski, A.L. and Ewald, S.K., 2012, Glacial landsystems and dynamics of the Saginaw Lobe of the Laurentide Ice Sheet, Michigan, USA: Quaternary International v.60, p. 21-31.

Kehew, A.E., Ewald, S.K., Esch, J.M. and Kozlowski, A.L. 2013, On the origin of tunnel channels of the Saginaw Lobe, Laurentide Ice Sheet, Michigan USA: Boreas, v. 42, pp. 442–462.

Kehew, A.E., Esch, J.M., and Karki, S., 2017, Sediment-landform assemblages in southern Michigan: Implications for basal processes of the Saginaw Lobe of the Laurentide ice sheet, *in* Kehew, A., and Curry, B.B., eds., Quaternary Glaciation of the Great Lakes Region: Process, Landforms, Sediments, and Chronology: Geological Society of America Special Paper 530, doi:10.1130/2017.2530(06).

Keller, S. J., and Rexroad, C. B., 1986, Coldwater Shale, *in* Shaver, R. H., Ault, C. H., Burger, A. M., Carr, D. D., Droste, J. B., Eggert, D. L., Gray, H. H., Harper, Denver, Hasenmueller, N. R., Hasenmueller, W. A., Horowitz, A. S., Hutchison, H. C., Keith, B. D., Keller, S. J., Patton, J. B., Rexroad, C. B., and Wier, C. E., Compendium of Paleozoic rock-unit stratigraphy in Indiana–a revision: Indiana Geological Survey Bulletin 59, p. 31.

Kozlowski, A.L. 1999, Three-dimensional mapping of the East Leroy and Union City 7.5 minute quadrangles in southwest Michigan: Masters Thesis, Western Michigan University, Kalamazoo.

Lane, J. W., E. A. White, G. V Steele, and J. C. Cannia. 2008, Estimation of bedrock depth using the horizontal-to-vertical (H/V) ambient-noise seismic method. Symposium on the Application of Geophysics to Engineering and Environmental Problems, April 6-10, 2008, Philadelphia, Pennsylvania, Proceedings: Denver, Colorado, Environmental and Engineering Geophysical Society:1–13.

Leverett, F. and Taylor F., 1915, Pleistocene of Indiana and Michigan and the history of the Great Lakes: U.S. Geological Survey Monograph 53, 529 p.

Martin, H.M., 1955, Map of the surface formations of the Southern Peninsula of Michigan: Michigan Department of Conservation, Geological Survey Division, Publication 49, scale 1:500,000.

McGinnis, L. D., and Kempton, J. P., 1961, Integrated seismic, resistivity, and geologic studies pf glacial deposits: Illinois Geological Survey Circular 323, 28 p.

Milstein, R. L. (compiler), 1987, Bedrock geology of southern Michigan: Geological Survey Division, Michigan Dept. of Natural Resources, scale= 1:500,000

Nakamura, Y., 1989, A method for dynamic characteristics estimation of subsurface using microtremor on the ground surface: Quarterly Report of RTRI, v. 30, no. 1, p. 25–33.

Obiadazie, A. C., 2011, Application of geophysical methods to locate buried tunnel channels beneath the glacial drift deposits in Texas Township, Kalamazoo County, MI: Masters Thesis, Western Michigan University. http://scholarworks.wmich.edu/masters_theses/396.

O'Cofaigh, C., 1996, Tunnel valley genesis: Progress in Physical Geography, v. 20, 1-19 p.

Olcott, P. G., 1992, Groundwater atlas of the United States: Iowa, Michigan, Minnesota, Wisconsin: U.S. Geological Survey Hydrologic Investigations Atlas HA 730-J.

U.S Geological Survey, 2019, Earthquake Catalog: U.S. Geological Survey database available at: https://earthquake.usgs.gov/earthquakes/search/ (accessed February 20, 2019).

Patterson, C.J., 1997, Southern Laurentide ice lobes were created by ice streams: Des Moines Lobe in Minnesota, USA: Sedimentary Geology 111, 249e261.

Pellicer, X. M., and Gibson, P., 2011, Electrical resistivity and ground penetrating radar for the characterization of the internal architecture of Quaternary sediments in the Midlands of Ireland: Journal of Applied Geophysics, v. 75. p. 638-647.

Rieck, R. L., and Winters, H. A., 1979, Lake, stream, and bedrock in southcentral Michigan: Annals of the Association of American Geographers, Vol. 69, No. 2, pp. 276-288.

Rieck, R. L., and Winters, H. A., 1982, Characteristics of a glacially buried cuesta in Southeast Michigan: Annals of the Associations of American Geographers, Vol. 72, pp. 482-494.

Rieck, R. L., 1983, Glacial drift thickness map, Southern Peninsula. Plate 15: Hydrogeological Atlas of Michigan. Kalamazoo, Michigan: Western Michigan University.

Seiderman, B. B., 2018, Mapping bedrock topography of the Portage and Schoolcraft NW 7.5' Quadrangles, Kalamazoo Co. MI, using the HVSR passive seismic method: Masters Thesis, Western Michigan, Kalamazoo. https://scholarworks.wmich.edu/masters_theses/3401

Sauck, W.A., 2017, Wind, earthquakes, traffic, and other factors in HVSR passive seismic data quality; two years of experience in Michigan: abstract, Proceedings of the Symposium on the Application of Geophysics to Engineering and Environmental Problems (SAGEEP), Denver, CO, Mar. 19-23.

SESAME, 2004, Guidelines for the implementation of the H/V spectral ratio technique on ambient vibrations. Measurements, processing and interpretation, WP12 European commission - Research general directorate project no. EVG1-CT-2000-0026 SESAME, report D23.12, 62 pp.

Smith, E.M., 1974, Exploration for a buried valley by resistivity and thermal probe surveys: Ground Water v. 12, No. 2, p. 78-83.

Telford, W.M., Geldart, L. P., and Sheriff, R. E., 1990, Applied geophysics 2nd edition: Cambridge University Press, New York.

Vandermeer, S., 2018, Mapping and interpreting the Quaternary Geology of Pictured Rocks National Lakeshore, Michigan: Doctoral Dissertation, Western Michigan University, Kalamazoo.

Woollard, G. P., and Joesting, H. R., 1964, Bouguer gravity anomaly map of the United States: U. S. Geol. Survey Spec. Map.

APPENDIX A

HVSR Data Spreadsheet

Station No.	Date	Lat -Deg N	Long-Deg W	Elevation (m)	Pr. Window	Fo (Hz)	Fo Std.Dev	Fo H/V ampl.	Peak 2 (Hz)	Peak2 H/V ampl.	Peak 3 (Hz)	Peak3 H/V ampl.	SESAME	Bedrock Pick (Hz)	Drift Thickness (m)	Bedrock Elevation (m)
CAL-007	4/13/2018	42.16617	-85.21727	280.4	15	5.5	0.44	4.7796	1.03	3.38	4.09	4.2964	7	5.5	8.4	272.1
CAL-008	4/13/2018	42.16654	-85.22689	281.6	15	3.75	0.93	3.1721	1.09	3.1721	4.62	5.3197	7	3.75	14.6	267.0
CAL-022A	4/30/2018	42.18803	-85.208029	283.8	15	1.69	0.1	4.9279	0.95	3.9615			8	1.69	47.0	236.7
CAL-023R	8/17/2018	42.18617	-85.202596	283.5	15	1.44	0.02	6.0345					9	1.44	59.5	224.0
CAL-027R	8/17/2018	42.16648	-85.185364	271.9	20	1.75	0.05	5.5476					9	1.75	44.7	227.2
CAL-030	5/1/2018	42.14522	-85.182701	275.2	15	1.56	0.13	4.4926	13.01	2.1322			8	1.19	52.9	222.4
CAL-031	5/1/2018	42.14534	-85.177458	280.1	15	2.13	0.08	3.5766	0.85	2.5916	1.89	0.8529	8	1.89	39.9	240.2
CAL-039	5/1/2018	42.14594	-85.123668	277.7	15	5.19	0.19	5.8909	1.06	3.157	3.3	3.031	9	5.19	9.1	268.6
CAL-042	5/1/2018	42.15655	-85.15555	286.2	15	3.38	1.97	5.4462	1.04	3.5329	9.39	1.9057	6	3.38	17.0	269.2
CAL-043	5/1/2018	42.1596	-85.144492	284.7	15	3.31	0.15	4.7885	1.06	2.4314	13.3	1.6281	9	3.31	17.6	267.1
CAL-055	5/5/2018	42.16093	-85.197338	278.3	15	3.88	0.2	5.9133	1.17	2.2553	37.01	1.9315	7	3.88	13.9	264.4
CAL-060R	8/17/2018	42.13806	-85.129258	277.1	15	4.94	0.05	5.0088	3.51	3.6485			9	4.94	9.8	267.3
CAL-077	5/8/2018	42.13239	-85.229639	264.6	15	2.94	0.03	5.1408	1.08	1.8017	7	1.6491	9	2.94	20.9	243.7
CAL-078	5/8/2018	42.13717	-85.24492	268.8	15	1.88	1.51	3.3325	8.31	2.6942	4.81	1.9215	7	1.88	40.2	228.6
KAL-471	5/8/2018	42.13634	-85.29882	286.5	15	1.25	0.17	5.9245					7	1.25	73.1	213.4
KAL-472	5/8/2018	42.13524	-85.298839	284.7	15	1.19	0.08	6.0122	3.6	1.5328			8	1.19	78.6	206.1
CAL-101R	8/17/2018	42.19565	-85.138889	286.8	15	2.31	0.08	5.5098					9	2.31	29.8	257.1
CAL-111	5/10/2018	42.21161	-85.178486	283.5	20	2.5	0.06	6.2573					9	2.5	26.5	257.0
CAL-116R	8/22/2018	42.19719	-85.247372	291.7	18	1.88	0.07	5.0782	3.96	2.453	1.13	2.7616	9	1.88	40.2	251.5
CAL-123	6/1/2018	42.20279	-85.200937	288.6	20	1.56	0.19	4.3146					7	1.56	52.9	235.8
CAL-125	6/1/2018	42.20537	-85.19799	292.9	20	1.84	0.22	3.3256	1.12	2.9358			7	1.84	41.5	251.4
CAL-126	6/1/2018	42.21169	-85.193262	287.4	15	3.69	0.69	3.7175	2.52	3.2907	1.08	2.3018	7	3.69	15.0	272.4
CAL-127	6/1/2018	42.21109	-85.202313	281.6	20	1.56	0.16	4.9766					8	1.56	52.9	228.8
CAL-134	6/2/2018	42.21684	-85.260352	289.0	20	2	0.25	5.6255	1.18	4.073			8	2	36.8	252.2
CAL-136	6/2/2018	42.21193	-85.276999	299.3	15	1.63	0.04	4.9341	7	2.1082			9	1.63	49.6	249.7
CAL-143	6/12/2018	42.23181	-85.214809	284.7	15	1.81	0.21	4.1006	1	2.5361	12.24	2.5435	7	1.81	42.5	242.1

CAL-145	6/12/2018	42.23104	-85.196531	285.0	15	1.19	0.06	7.2019	6.62	1.6625	31.35	1.8913	8	1.19	78.6	206.4
CAL-148	6/12/2018	42.23273	-85.171512	279.8	15	2.38	0.1	4.4284	5.02	1.907			9	2.38	28.5	251.3
CAL-149	6/12/2018	42.23039	-85.169002	284.1	15	2	0.05	5.59					9	2	36.8	247.3
CAL-150	6/12/2018	42.23205	-85.158609	281.6	15	2.94	0.31	4.8248	1	2.7786	4.97	2.6532	7	2.94	20.9	260.7
CAL-151	6/12/2018	42.23191	-85.155174	281.6	20	2.81	0.04	4.9638					9	2.81	22.3	259.3
CAL-154	6/12/2018	42.23221	-85.138401	289.3	20	2.69	0.09	3.0442	1.06	2.0756			9	2.69	23.8	265.4
CAL-156	6/12/2018	42.227	-85.168457	287.1	18	2.72	0.09	2.8742	9.92	2.4949		2.1161	8	2.72	23.4	263.7
CAL-162	6/13/2018	42.21553	-85.166118	284.4	15	1.81	0.32	3.7583	5.52	2.5878	11.02	2.6855	6	1.81	42.5	241.8
CAL-164	6/13/2018	42.25808	-85.169379	284.7	15	2.19	0.11	3.6737					9	2.19	32.2	252.5
CAL-166	6/13/2018	42.24361	-85.168823	290.5	15	2.5	0.12	4.3696	1.08	2.6386			9	2.5	26.5	264.0
CAL-172R	8/17/2018	42.22034	-85.121003	288.0	15	1.5	0.01	4.4657					9	1.5	56.0	232.0
CAL-179	6/14/2018	42.24571	-85.156962	287.1	15	2.5	0.12	4.5445	0.96	2.1822			9	2.5	26.5	260.6
CAL-180	6/14/2018	42.24673	-85.145874	278.3	15	4.69	0.16	4.2871	3	3.341	1	1.7498	9	4.69	10.6	267.7
CAL-181	6/14/2018	42.25204	-85.149243	277.4	15	2.31	0.07	6.249	1.12	2.1827			9	2.31	29.8	247.6
CAL-182	6/14/2018	42.25969	-85.148099	279.2	15	3.06	0.12	5.2689	4.65	3.2032	1.18	1.9682	9	3.06	19.7	259.5
CAL-183R	8/22/2018	42.23119	-85.237561	286.2	20	1.31	0.08	4.5748					8	1.31	68.3	217.9
CAL-191	6/15/2018	42.25012	-85.22303	286.8	15	1.56	0.12	4.2724					8	1.56	52.9	233.9
CAL-192	6/15/2018	42.24639	-85.237831	286.8	15	1.25	0.05	7.1483	3.56	1.2792	8.04	1.097	9	1.25	73.1	213.7
CAL-198A	6/19/2018	42.1658	-85.272782	286.8	15	1.31	0.09	4.0276					8	1.31	68.3	218.5
CAL-200	6/21/2018	42.13643	-85.23957	277.4	15	1.81	0.03	4.4807	1.08	2.5962	5.67	1.6664	9	1.81	42.5	234.8
CAL-203	6/25/2018	42.22598	-85.262527	290.2	20	1.78	0.05	3.4794					9	1.78	43.6	246.6
CAL-204	6/25/2018	42.23566	-85.267311	295.0	15	1.19	0.04	4.9436					9	1.19	78.6	216.5
CAL-205	6/25/2018	42.23507	-85.277065	291.1	15	1.25	0.04	4.9364	10.96	2.0068			9	1.25	73.1	218.0
CAL-207	6/25/2018	42.24309	-85.291965	297.2	15	1.13	0.05	4.9372	5.43	1.7829			9	1.13	84.8	212.4
CAL-208	6/25/2018	42.24838	-85.28418	296.9	18	1.16	0.06	5.2188	7.2	2.1689			8	1.16	81.6	215.3
CAL-214	6/28/2018	42.21616	-85.167233	281.3	15	1.69	0.06	3.4026	5.25	2.4917	1.18	2.7028	7	1.69	47.0	234.3
CAL-215	7/10/2018	42.21754	-85.173912	282.5	20	1.34	0.04	6.5354					9	1.34	66.1	216.5
CAL-221	7/11/2018	42.18843	-85.20368	286.5	15	1.5	0.01	5.8413	6	1.4009			9	1.5	56.0	230.5

CAL-222	7/11/2018	42.18809	-85.210476	286.2	18	2.06	0.06	3.1456	1.08	2.7935			9	2.06	35.2	251.0
CAL-227	7/11/2018	42.17979	-85.197657	286.5	20	1.34	0.02	4.9298					9	1.34	66.1	220.5
CAL-229	7/11/2018	42.19877	-85.197981	282.2	20	2.41	0.18	3.7728	6.52	2.1294	1.13	2.4336	7	2.41	28.0	254.3
KAL-492	7/12/2018	42.11525	-85.352643	277.7	20	1.13	0.03	4.8047	6.3	3.2138	1.25	4.5308	9	1.25	73.1	204.5
KAL-493	7/12/2018	42.11508	-85.342954	277.7	15	1.25	0.15	4.9433	1.44	4.9136	6.85	2.5393	7	1.25	73.1	204.5
KAL-494	7/12/2018	42.11504	-85.333203	281.9	20	1.47	0.14	4.7975					8	1.47	57.7	224.3
KAL-495	7/12/2018	42.11519	-85.32076	282.2	20	1.47	0.09	4.5279	6.96	3.0708			8	1.47	57.7	224.6
KAL-496	7/12/2018	42.11485	-85.309487	274.3	15	2	0.28	4.0699	1.65	3.9313	1.17	3.052	7	2	36.8	237.6
CAL-237	7/12/2018	42.12936	-85.265355	273.1	20	1.81	0.05	3.8203	7.48	2.0836			9	1.81	42.5	230.6
CAL-238	7/12/2018	42.14039	-85.255936	279.2	20	1.44	0.03	3.849	1.88	2.9719	6.55	1.7565	9	1.44	59.5	219.7
CAL-239	7/12/2018	42.1475	-85.255787	281.6	20	1.25	0.03	4.4279	6.2	1.6799			9	1.25	73.1	208.5
CAL-241	7/12/2018	42.17951	-85.266421	292.0	20	1.22	0.07	3.1114					7	1.22	75.8	216.2
CAL-244	7/16/2018	42.20987	-85.216249	280.4	15	1.19	0.03	4.1469	2.87	2.3392			9	1.19	78.6	201.8
CAL-245	7/16/2018	42.23188	-85.221342	283.8	15	1.38	0.05	5.6399					9	1.38	63.3	220.5
CAL-247	7/16/2018	42.19739	-85.266702	294.1	18	1.34	0.05	4.1975					9	1.34	66.1	228.1
KAL-513	7/23/2018	42.14832	-85.295247	285.6	18	1.16	0.02	4.7768					9	1.16	81.6	204.0
KAL-514	7/23/2018	42.1429	-85.295125	285.6	20	1.47	0.24	3.4827	0.97	2.683	3.23	2.2125	7	1.47	57.7	227.9
KAL-534	7/25/2018	42.1583	-85.353729	286.8	20	1.88	0.28	2.8435	1.55	2.6205			7	1.88	40.2	246.6
KAL-536	7/25/2018	42.17933	-85.364486	289.3	15	1.88	0.15	3.8073	1.25	2.7868	8.13	2.265	8	1.88	40.2	249.0
KAL-550	7/27/2018	42.20152	-85.382016	282.9	20	2.13	0.05	5.1407	1.09	2.7781			9	2.13	33.5	249.3
KAL-555	7/27/2018	42.2018	-85.344142	289.0	20	2.19	0.19	3.5107	1.14	2.6908			7	2.19	32.2	256.8
KAL-571R	8/17/2018	42.21934	-85.335461	286.5	15	2.75	0.08	3.9032	4	3.7261	5.19	2.9239	9	2.75	23.1	263.5
KAL-574	7/30/2018	42.23808	-85.330506	294.1	20	2.31	0.16	5.2872	1.12	2.7717			7	2.31	29.8	264.4
KAL-575	7/30/2018	42.23816	-85.343309	295.7	20	1.75	0.07	3.1299	2.99	2.0755			9	1.75	44.7	251.0
KAL-576	7/30/2018	42.23783	-85.354149	293.5	20	2.09	0.08	4.363	4.03	1.9188			9	2.09	34.5	259.1
KAL-577	7/30/2018	42.2309	-85.355374	292.6	20	1.78	0.03	4.5595	4.03	2.2577			9	1.78	43.6	249.0
CAL-260	8/1/2018	42.24311	-85.217854	287.7	15	1.56	0.12	3.5095					8	1.56	52.9	234.9
CAL-261	8/1/2018	42.22832	-85.217814	286.8	20	1.53	0.14	3.2543	1.85	3.028			8	1.53	54.4	232.4

CAL-262	8/1/2018	42.13828	-85.144783	280.7	20	3.44	0.02	6.1847					9	3.44	16.6	264.1
CAL-263	8/1/2018	42.13822	-85.15321	283.2	20	4.03	0.13	3.5716	2.6	2.4008	1.14	1.8837	9	4.03	13.2	270.0
CAL-268	8/1/2018	42.13232	-85.189751	272.8	20	2.31	0.03	4.0679	9.39	3.3027	1.12	2.3181	9	2.31	29.8	243.0
KAL-592	8/2/2018	42.25325	-85.325054	298.7	20	2.38	0.04	4.5211					9	2.38	28.5	270.2
KAL-593	8/2/2018	42.25332	-85.316992	298.1	15	1.56	0.03	3.8208	4.03	2.5134			9	1.56	52.9	245.2
KAL-594	8/2/2018	42.25343	-85.304409	295.7	15	1.13	0.06	6.9338					8	1.13	84.8	210.9
CAL-269	8/2/2018	42.24663	-85.296949	299.0	20	1.13	0.03	5.7827	3.6	1.5591	5	2.0619	9	1.13	84.8	214.2
CAL-271	8/2/2018	42.17402	-85.24698	286.2	15	4	0.17	4.3066	1.06	2.108	9.08	1.4122	9	4	13.3	272.9
CAL-273	8/2/2018	42.21034	-85.138692	291.7	18	3.34	0.25	3.3529					7	3.34	17.3	274.3
CAL-275	8/17/2018	42.16513	-85.184404	274.0	20	2.03	0.05	6.4416					9	2.03	36.0	238.1
CAL-278	8/22/2018	42.24828	-85.177146	289.9	20	2.16	0.07	5.6678	0.92	2.5901			9	2.16	32.8	257.0
CAL-288	9/15/2018	42.18438	-85.187563	274.9	20	2.5	0.35	4.3429					7	2.5	26.5	248.4
CAL-289	9/15/2018	42.18467	-85.189891	283.5	20	1.91	0.18	4.3665	1.1	2.6341			8	1.91	39.3	244.1
CAL-282	9/14/2018	42.27408	-85.20677	279.8	15	2.5	0.1	5.6796	1.03	2.1852			9	2.5	26.5	253.3
CAL-283	9/14/2018	42.27423	-85.207154	278.9	15	3	0.37	5.4691	2.45	5.1951			7	3	20.3	258.6
CAL-284	9/14/2018	42.27411	-85.207541	278.9	20	2.44	0.08	5.634	4.07	3.0987			9	2.44	27.5	251.4
CAL-285	9/14/2018	42.27393	-85.20746	281.3	20	2.44	0.04	6.1584	4.19	2.3227			9	2.44	27.5	253.9
CAL-009	4/13/2018	42.16693	-85.14861	281.9	15	3.25	1.16	3.6074	1.13	2.6832	4	3.471	7	3.25	18.1	263.9
CAL-010	4/13/2018	42.16651	-85.15936	289.0	15	4	0.45	2.7961	1.14	2.476	14.06	2.7771	6	4	13.3	275.6
CAL-011	4/13/2018	42.16647	-85.17831	273.7	15	3.56	0.95	3.9159	1.19	3.3272	5	3.4961	6	3.56	15.8	257.9
CAL-012	4/13/2018	42.16639	-85.19775	285.3	15	3.56	0.79	3.1496	1.13	2.1826	8.64	2.9058	7	3.56	15.8	269.5
CAL-015A	4/30/2018	42.1875	-85.274705	293.5	15	2.13	0.75	3.6977	0.95	3.6057	4.7	2.2313	6	2.13	33.5	260.0
CAL-016A	4/30/2018	42.1876	-85.266144	295.4	15	0.94	8.13	3.2735	5	2.4351			7	0.94	111.0	184.3
CAL-017A	4/30/2018	42.18739	-85.257964	295.4	15	1	0.19	5.8733	0.5	5.3801			7	1	101.4	194.0
CAL-021B	4/30/2018	42.18803	-85.21625	281.0	15	2.75	0.09	6.3387					9	2.75	23.1	258.0
CAL-025R	9/15/2018	42.18416	-85.186227	272.5	15	3.69	0.26	3.6785	2.46	3.139			6	3.69	15.0	257.5
CAL-028	5/1/2018	42.14513	-85.207608	269.7	15	1.13	1.14	3.1119	2.83	3.0331	5	2.6588	6	2.83	22.1	247.6
CAL-029	5/1/2018	42.14519	-85.194732	279.8	15	1.06	3.73	3.1551	6.44	2.8041			6	1.06	93.1	186.7

CAL-034	5/1/2018	42.14466	-85.144069	281.3	15	3.5	0.91	5.4864	1.12	4.2577	12.51	2.9379	7	3.5	16.2	265.1
CAL-035	5/1/2018	42.14733	-85.134325	283.2	15	1.06	0.09	4.589	4.55	3.6358	9.99	2.0842	6	4.55	11.0	272.1
CAL-040	5/1/2018	42.14581	-85.1313	278.0	15	1.13	2.08	3.9024	3.75	3.7568	5.25	3.8907	5	5.25	8.9	269.0
CAL-041	5/1/2018	42.15303	-85.159043	287.4	15	0.94	0.31	5.0318	3.71	3.6861	5.43	3.2352	5	3.71	14.9	272.6
CAL-044	5/5/2018	42.15241	-85.208613	275.2	15	1.13	0.07	5.8831	5.05	3.3599	15.44	3.292	7	5.05	9.5	265.8
CAL-045	5/5/2018	42.15203	-85.218564	267.3	15	4.38	0.04	9.5885	1.25	4.0023			9	4.38	11.7	255.6
CAL-047	5/5/2018	42.15173	-85.246567	273.4	15	2.44	0.3	4.1466	6.1	2.3512			6	2.44	27.5	245.9
CAL-048	5/5/2018	42.15144	-85.254788	283.2	15	1.19	0.27	4.6902	1.83	4.1338	11.84	2.6336	6	1.83	41.9	241.3
CAL-050	5/5/2018	42.15076	-85.268878	281.0	15	2.38	23.35	3.176	0.55	2.7167			6	2.38	28.5	252.5
CAL-056	5/5/2018	42.15885	-85.20465	281.9	15	1.13	16.81	3.8595	4.05	3.363	10.9	2.6409	5	4.05	13.1	268.9
CAL-057	5/5/2018	42.15864	-85.205826	282.5	15	5	0.48	5.2536	0.88	2.504	5.8	4.8052	7	5	9.6	272.9
CAL-058	5/5/2018	42.16641	-85.206733	283.2	15	3.13	0.35	4.0754	4.7	2.7438	1	2.4533	7	3.13	19.1	264.1
CAL-059	5/7/2018	42.13828	-85.122275	283.8	15	0.94	1.29	2.7745	3.94	2.4077	7.32	2.5483	6	3.94	13.6	270.1
CAL-066	5/7/2018	42.13442	-85.18649	275.8	15	1	0.16	3.9663	3.35	2.9937			5	3.35	17.3	258.6
CAL-068	5/7/2018	42.13802	-85.199337	274.3	15	1.81	0.03	3.5637	1.13	2.8553			8	1.81	42.5	231.8
CAL-070	5/7/2018	42.15339	-85.121158	279.2	15	5	2.07	3.897	6.48	3.81	3.17	2.68	7	5	9.6	269.6
CAL-072	5/8/2018	42.12625	-85.206747	276.1	15	4.94	0.79	3.8185	4.16	3.6946	1.01	3.0294	7	4.16	12.6	263.6
CAL-074	5/8/2018	42.12659	-85.220417	273.7	15	6	0.67	4.0421	1.01	3.9749	31.35	1.7968	7	6	7.4	266.4
CAL-075	5/8/2018	42.12652	-85.224396	272.8	15	6.19	0.24	4.951	1.11	2.585	3.1	2.3266	9	6.19	7.0	265.8
CAL-076	5/8/2018	42.12615	-85.231229	269.7	15	5.63	1.49	3.2997	0.63	2.8159	2.95	2.5274	7	5.63	8.1	261.7
CAL-080	5/8/2018	42.13814	-85.252051	278.9	15	1.06	0.36	3.7369	1.87	3.6736	11.84	2.442	7	1.87	40.6	238.3
CAL-082	5/8/2018	42.13713	-85.270599	279.5	15	1.25	0.02	4.8172	1.55	4.2825	15.96	2.1338	9	1.25	73.1	206.4
CAL-083	5/8/2018	42.14416	-85.275301	279.2	15	1.13	1.11	6.0105	10.54	4.0832	7.04	2.8377	7	1.13	84.8	194.4
CAL-084	5/8/2018	42.13707	-85.280862	276.8	15	1.44	0.19	5.3686	4.94	2.0793	6.85	2.2116	7	1.44	59.5	217.3
CAL-085	5/8/2018	42.137	-85.286942	280.7	15	1.13	0.17	4.3931	1.42	3.9882	6.06	1.9253	7	1.13	84.8	195.9
CAL-088	5/9/2018	42.18847	-85.164806	283.8	15	3.06	0.77	4.3512	1.11	4.0444	4.7	3.1176	6	3.06	19.7	264.0
CAL-090	5/9/2018	42.18615	-85.146574	281.3	15	4	0.15	4.8309	5.52	3.7607	1	3.0723	9	4	13.3	268.0
CAL-093	5/9/2018	42.17543	-85.140669	277.4	15	3.69	0.06	5.4818	1.96	1.9079	1.11	1.9171	9	3.69	15.0	262.4

CAL-095	5/9/2018	42.17938	-85.126568	277.7	15	3.31	0.07	3.5361	0.87	2.9305	4.5	2.6901	8	3.31	17.6	260.1
CAL-096	5/9/2018	42.17407	-85.156246	288.6	10	3.31	0.68	3.4338	7.86	2.8526	0.99	2.0422	7	3.31	17.6	271.1
CAL-097	5/9/2018	42.174	-85.167856	288.6	15	2.94	3.56	2.7004	10.6	2.6696	1.21	2.2149	6	2.94	20.9	267.7
CAL-098	5/9/2018	42.17066	-85.172726	284.7	10	4.31	1.05	4.1962	1.1	3.0014	4.4		6	4.4	11.6	273.1
CAL-099	5/9/2018	42.17982	-85.17824	287.7	15	3.31	10.92	2.4338	6.06	1.8967	0.44	1.8949	6	3.31	17.6	270.2
CAL-102	5/10/2018	42.1871	-85.129397	278.3	20	3.28	0.12	3.7443	1.18	2.9784			9	3.28	17.8	260.5
CAL-108	5/10/2018	42.20418	-85.161039	287.7	10	1.13	0.61	3.4872	6.03	3.226	2.25	2.4302	5	6.03	7.3	280.4
CAL-109	5/10/2018	42.20338	-85.160887	286.8	15	7.69	1.46	2.8271	2.5	2.5315	1.06	2.5268	6	7.69	5.1	281.7
CAL-114	6/1/2018	42.20238	-85.246878	291.7	15	1.13	0.11	3.3218	1.79	2.2092			8	1.13	84.8	206.9
CAL-115	6/1/2018	42.20254	-85.237806	285.0	15	1.06	0.29	3.4068	1.42	3.1691	1.25	3.3949	7	1.42	60.7	224.3
CAL-117	6/1/2018	42.18703	-85.22099	281.9	15	3.94	0.78	3.2141	3.07	3.029	1.05	3.1251	6	3.94	13.6	268.3
CAL-118	6/1/2018	42.1881	-85.21955	282.2	15	3.88	2.17	3.0143	3.14	2.9843	0.92	2.6294	6	3.88	13.9	268.3
CAL-120	6/1/2018	42.19653	-85.217957	284.7	15	1.5	0.23	4.3143	1.04	4.1476	7.86	2.4549	7	1.5	56.0	228.7
CAL-121	6/1/2018	42.20273	-85.214722	289.0	15	1.25	0.26	3.7403	9.7	2.5447	0.94	2.9634	7	1.25	73.1	215.8
CAL-122	6/1/2018	42.20302	-85.207711	292.6	15	1.19	0.05	3.5186	1.64	3.1404	6	1.989	9	1.19	78.6	214.0
CAL-128	6/2/2018	42.21776	-85.203678	280.4	15	1.81	0.32	4.0016	6.55	2.2871	1.24	3.913	7	1.81	42.5	237.9
CAL-129	6/2/2018	42.21741	-85.20831	286.5	15	1.69	0.36	2.884	1.03	2.8794			7	1.69	47.0	239.5
CAL-130	6/2/2018	42.2175	-85.217901	287.1	15	1.81	0.35	2.5964	0.99	2.3499			7	1.81	42.5	244.6
CAL-131	6/2/2018	42.21716	-85.227604	282.2	15	1.19	0.11	3.726	10.6	3.2264	16.41	2.2401	8	1.19	78.6	203.6
CAL-132	6/2/2018	42.21704	-85.238302	286.2	15	1.69	0.67	3.3463	2.34	2.982	1.06	2.7559	7	1.69	47.0	239.2
CAL-133	6/2/2018	42.21689	-85.250043	287.4	15	1.25	0.12	3.9083	2	3.0862	4.7	2.1177	8	1.25	73.1	214.3
CAL-135	6/2/2018	42.21899	-85.267337	301.1	10	2.94	0.91	2.9392	4.57	2.6223	0.87	2.5959	6	2.94	20.9	280.2
CAL-139	6/2/2018	42.21661	-85.293208	296.9	15	2.31	0.3	3.6663	4.65	2.6104	1.23	2.3697	7	2.31	29.8	267.1
CAL-144	6/12/2018	42.23181	-85.206955	290.2	18	2	0.08	3.1572	11.33	1.8762			7	2	36.8	253.4
CAL-146	6/12/2018	42.23198	-85.185715	280.4	15	1.44	0.73	4.3567	5.52	3.0223	22.25	3.0844	6	1.44	59.5	221.0
CAL-147	6/12/2018	42.23171	-85.179093	284.7	15	2.63	0.47	3.4186	4.97	3.0304	1.19	2.4235	7	2.63	24.6	260.1
CAL-152	6/12/2018	42.23213	-85.120701	285.9	20	2.19	0.37	2.8708	3.19	2.2107	12.04	2.2973	7	2.19	32.2	253.7
CAL-155	6/12/2018	42.23205	-85.15062	285.0	15	3.13	0.28	3.2124	4.73	2.5929	1.06	1.9219	7	3.13	19.1	265.9

CAL-158	6/13/2018	42.14304	-85.129579	276.1	15	3.75	0.1	3.9154	0.93	3.0362			8	3.75	14.6	261.5
CAL-159	6/13/2018	42.2105	-85.160606	286.5	15	1.75	0.18	3.9368	1	3.5582	4.3	2.5462	6	1.75	44.7	241.8
CAL-160	6/13/2018	42.21751	-85.164359	289.3	15	5	0.99	2.5001	2.19	2.3468			6	2.19	32.2	257.1
CAL-161	6/13/2018	42.21554	-85.16631	284.4	15	15.31	4.89	3.7089	1.88	3.5581	5.46	2.1526	7	1.88	40.2	244.1
CAL-163	6/13/2018	42.2224	-85.162243	282.9	15	2.94	0.97	3.8602	4.05	3.3285	5.9	3.1042	6	2.94	20.9	261.9
CAL-165	6/13/2018	42.24939	-85.169096	296.9	15	1.81	0.19	4.9548	2.1	4.8366			7	1.81	42.5	254.3
CAL-167	6/13/2018	42.24108	-85.168465	288.3	15	2.5	0.43	4.0529	4.7	3.5247	1.12	3.016	6	2.5	26.5	261.8
CAL-178	6/14/2018	42.24417	-85.134653	277.7	15	3.13	0.17	3.1168	7.44	2.2275	1.09	2.1161	7	3.13	19.1	258.6
CAL-184	6/15/2018	42.23151	-85.247819	290.8	15	1.06	0.1	6.1178	5.28	1.605	3.53	0.9882	8	1.06	93.1	197.7
CAL-185	6/15/2018	42.23162	-85.254487	287.7	15	1.06	0.12	5.7045					7	1.06	93.1	194.6
CAL-186	6/15/2018	42.23492	-85.258294	290.5	15	1.06	0.01	5.8794	5.67	2.1631			9	1.06	93.1	197.4
CAL-190	6/15/2018	42.25665	-85.238	286.8	15	1.25	0.23	4.6911	1.76	4.1829	5	2.181	7	1.25	73.1	213.7
CAL-193	6/15/2018	42.24043	-85.228104	286.5	15	1.63	0.26	3.6601	1.25	3.5762	1.05	3.2762	7	1.63	49.6	236.9
CAL-194	6/15/2018	42.25019	-85.210612	290.2	15	1.13	0.21	4.0544	1.88	2.7832	9.08	2.4682	7	1.88	40.2	249.9
CAL-195	6/15/2018	42.23952	-85.200317	289.9	15	1.06	0.01	4.111	1.6	3.6802	6.44	2.3962	9	1.6	51.0	238.9
CAL-197A	6/19/2018	42.16839	-85.266212	285.6	18	1.88	0.29	3.6737	8.69	3.0931			7	1.88	40.2	245.4
CAL-199A	6/19/2018	42.16562	-85.295315	285.0	15	1.13	0.42	3.3827	4.65	2.5484	1.87	2.6782	6	1.13	84.8	200.2
KAL-478A	6/19/2018	42.17256	-85.315362	289.3	15	1.88	0.27	3.3056	1.15	3.1325			7	1.88	40.2	249.0
KAL-479A	6/19/2018	42.17292	-85.326553	284.7	15	2.38	0.48	3.58	1.88	3.3881	1.13	2.664	7	2.38	28.5	256.2
KAL-482A	6/19/2018	42.17128	-85.35181	284.4	15	1.88	0.42	2.6701	1.19	2.5911	2.86	2.0603	7	1.88	40.2	244.1
CAL-201	6/25/2018	42.22443	-85.28247	299.3	15	1.19	0.14	3.2584	2.14	3.1689	6.03	2.7042	7	2.14	33.3	266.0
CAL-202	6/25/2018	42.22421	-85.271134	302.4	15	2.19	1.33	2.6262	1.07	2.4305	10.14	2.136	6	2.19	32.2	270.2
KAL-489	7/10/2018	42.1313	-85.325234	290.8	15	1.75	0.11	3.386	17.73	2.3615	14.86	2.3006	8	1.75	44.7	246.1
KAL-490	7/10/2018	42.13424	-85.316943	281.3	15	2.31	0.07	4.4184	3.55	2.1817	13.45	2.0461	9	2.31	29.8	251.6
CAL-216	7/10/2018	42.21796	-85.19038	279.5	15	2.5	0.31	3.5631					7	2.5	26.5	253.0
CAL-218	7/10/2018	42.20161	-85.17872	286.2	15	4.13	0.23	3.0821	2.2	1.9376	1.07	2.355	7	4.13	12.7	273.5
CAL-219	7/11/2018	42.19146	-85.178647	282.9	15	3.5	0.32	2.9523	5.83	2.1475	8.59	2.1283	6	3.5	16.2	266.7
CAL-220	7/11/2018	42.18447	-85.178585	286.8	15	3.5	2.82	2.8255	1.13	1.825	13.15	1.995	7	3.5	16.2	270.6

CAL-224	7/11/2018	42.18635	-85.227157	290.2	15	3.44	0.2	3.2549	1.13	2.4173	8.45	2.3364	7	3.44	16.6	273.6
CAL-226	7/11/2018	42.17347	-85.199844	281.0	15	5.63	0.13	2.5721	3.13	2.4089	1.17	2.1554	9	5.63	8.1	272.9
CAL-228	7/11/2018	42.19091	-85.197848	283.8	15	2.19	0.19	3.2221	3	2.8505	1	2.3466	7	2.19	32.2	251.6
CAL-231	7/12/2018	42.12223	-85.289935	276.8	15	1.88	0.4	3.0317	1.24	2.8845	0.89	2.5259	6	1.88	40.2	236.5
CAL-234	7/12/2018	42.12245	-85.25836	271.0	15	2.44	0.67	2.8841	1.16	2.6436			6	2.44	27.5	243.5
CAL-240	7/12/2018	42.15869	-85.25629	283.2	15	1.63	0.18	3.7132	1.21	3.5847			7	1.63	49.6	233.6
CAL-243	7/16/2018	42.20767	-85.217246	281.0	20	1.25	0.08	3.2296	1.63	2.9796			7	1.25	73.1	207.9
KAL-499	7/16/2018	42.21913	-85.311038	292.9	20	2.16	0.48	2.8504	6.48	1.902			7	2.16	32.8	260.1
KAL-503	7/23/2018	42.14407	-85.37152	277.4	15	2.25	0.68	2.8533	1.02	2.6227	12.65	1.9293	7	2.25	30.9	246.4
KAL-510	7/23/2018	42.14699	-85.305008	281.9	18	2.16	0.02	3.3499	6.7	2.8967	1.07	2.4827	9	2.16	32.8	249.1
KAL-515	7/23/2018	42.12751	-85.304486	277.4	15	1.81	0.46	3.4618					7	1.81	42.5	234.8
KAL-516	7/23/2018	42.12205	-85.304204	278.9	20	1.25	0.09	3.7032					8	1.25	73.1	205.8
CAL-251	7/24/2018	42.15419	-85.177906	279.2	15	3.75	1.26	3.9612	4.89	3.2927	6.77	2.7055	7	3.75	14.6	264.6
CAL-252	7/24/2018	42.13071	-85.177412	274.0	15	3.56	0.41	3.3829	4.62	2.6087			6	3.56	15.8	258.2
KAL-517	7/24/2018	42.12218	-85.333335	285.0	15	1.56	0.19	3.5149					7	1.56	52.9	232.1
KAL-521	7/24/2018	42.1655	-85.330753	287.4	18	1.5	0.11	3.4055	1.87	2.9491	10.54	2.364	8	1.5	56.0	231.4
KAL-524	7/24/2018	42.16549	-85.363996	287.4	20	1.06	0	3.7844	10.31	3.4156	1.56	3.2811	9	1.06	93.1	194.3
KAL-525	7/24/2018	42.16544	-85.373666	287.1	15	1.06	2.24	2.7211	2.12	2.4633	9.49	1.8446	7	1.06	93.1	194.0
KAL-529	7/25/2018	42.12538	-85.353119	276.1	20	1.66	0.02	3.9436	1.1	3.3207			9	1.66	48.3	227.9
KAL-530	7/25/2018	42.13691	-85.353157	276.5	15	1.19	0.08	3.3523	2.12	2.1033	8.5	2.2763	7	1.19	33.7	242.7
KAL-532	7/25/2018	42.15151	-85.3644	280.7	15	1.13	0.47	2.8899	1.77	2.4775	8.98	2.4031	7	1.13	84.8	195.9
KAL-542	7/25/2018	42.18677	-85.334027	284.7	15	11.13	2.14	2.951	1.88	2.8174			7	1.88	40.2	244.4
KAL-543	7/25/2018	42.18715	-85.324323	288.6	15	1.25	0.25	2.591					6	1.25	73.1	215.5
KAL-546	7/26/2018	42.18016	-85.315005	289.9	15	1.13	1.87	2.5877					7	1.13	84.8	205.1
KAL-548	7/26/2018	42.18014	-85.295724	292.3	15	3.31	0.64	2.6343	1.06	2.0095	8.5	1.7472	6	3.31	17.6	274.7
CAL-253	7/26/2018	42.17984	-85.28578	290.5	20	2.28	0.73	4.1416					7	2.28	30.3	260.1
CAL-254	7/26/2018	42.17328	-85.285627	285.3	15	1.75	0.24	3.6242	1.23	2.875	4.05	2.6419	6	1.75	44.7	240.6
KAL-549	7/26/2018	42.18717	-85.306483	286.5	15	3.56	0.97	3.1516	4.3	3.0325	1.14	1.9961	7	3.56	15.8	270.7

CAL-257	7/26/2018	42.19472	-85.286232	295.4	15	4	0.47	3.3838	1.14	2.6202	4.81	2.4479	6	4	13.3	282.0
CAL-258Y	7/26/2018	42.2019	-85.286164	296.6	20	3.5	0.53	2.9039	1.13	1.7738			7	3.5	16.2	280.4
CAL-259	7/26/2018	42.20196	-85.296024	296.0	20	3.13	0.15	2.6131	4.03	2.3645	1.07	2.0559	9	3.13	19.1	276.9
KAL-551	7/27/2018	42.20185	-85.371634	284.4	15	1.56	0.41	3.8085	1.11	3.2443			7	1.56	52.9	231.5
KAL-553	7/27/2018	42.20058	-85.349756	289.9	20	1.47	0.06	2.9293	1.84	2.6481			9	1.47	57.7	232.2
KAL-560	7/27/2018	42.20177	-85.319598	288.6	15	6.63	0.3	4.9486					9	6.63	6.4	282.3
KAL-562	7/27/2018	42.19355	-85.325401	286.5	20	1.81	0.06	3.4968	5.55	2.7256			9	1.81	42.5	244.0
KAL-565	7/27/2018	42.23087	-85.38325	288.3	15	1.88	0.07	4.0193	1.16	3.132	2.75	2.6612	9	1.88	40.2	248.1
KAL-566	7/27/2018	42.23084	-85.372614	289.6	15	1.81	0.07	2.9459	4.03	2.4913	8.45	1.3678	8	1.81	42.5	247.0
KAL-568	7/30/2018	42.21836	-85.374606	282.9	15	1.44	0.14	6.9123	1.81	5.8966	2.76	4.4589	8	1.44	59.5	223.4
KAL-570	7/30/2018	42.21214	-85.349932	286.2	15	3.25	0.42	4.5546	2.67	4.31			7	2.67	24.1	262.1
KAL-578	7/30/2018	42.23092	-85.364712	291.1	20	1.25	0.29	3.757	1.82	3.373	3.35	2.647	7	1.25	73.1	218.0
KAL-579	7/30/2018	42.23442	-85.337293	295.0	15	1.88	0.34	3.0187					6	1.88	40.2	254.8
KAL-580	7/30/2018	42.22822	-85.335469	291.4	15	2.31	0.08	4.1168	4.07	3.7566			9	2.31	29.8	261.6
KAL-581	8/1/2018	42.22338	-85.354284	289.9	18	1.25	0.1	3.757					8	1.25	73.1	216.7
KAL-583	8/1/2018	42.22363	-85.341313	288.3	15	2.25	0.19	2.9982	1.13	2.3147			7	2.25	30.9	257.4
KAL-584	8/1/2018	42.21585	-85.359781	288.3	15	2.19	0.09	3.4245	1.07	3.0653	5.49	2.3402	9	2.19	32.2	256.2
KAL-585	8/1/2018	42.25494	-85.336581	300.2	15	1.25	0.12	3.586	1.63	3.4289			8	1.25	73.1	227.1
CAL-264	8/1/2018	42.12394	-85.14896	275.5	15	2.94	0.28	3.2565	1.25	2.4545			7	2.94	20.9	254.6
CAL-265	8/1/2018	42.12347	-85.168642	275.8	16	2	0.14	3.2923	2.5	2.9957	1.17	2.9642	6	2	36.8	239.1
CAL-267	8/1/2018	42.12693	-85.177773	272.8	15	3.06	0.28	2.8303	1.13	2.6387	1.88	2.1515	5	3.06	19.7	253.1
KAL-588	8/2/2018	42.23815	-85.362349	292.3	15	2	1.14	2.7075	4.03	2.44	2.76	2.3088	7	2	36.8	255.6
KAL-589	8/2/2018	42.23833	-85.373702	288.6	15	4.06	1.84	3.4669	1.23	3.3608	1.7	2.7021	7	1.23	74.9	213.8
KAL-590	8/2/2018	42.24512	-85.380206	285.9	20	1.19	0.24	4.4665					7	1.19	78.6	207.3
KAL-591	8/2/2018	42.25262	-85.376237	292.0	18	1.13	0.12	3.4761	4.55	1.9186			7	1.13	84.8	207.2
CAL-272	8/2/2018	42.17917	-85.22725	287.7	15	3.75	1.07	2.6847	5.46	2.4895			6	3.75	14.6	273.1
CAL-274	8/2/2018	42.22651	-85.13911	292.6	15	2.69	0.32	3.0882	1.06	2.6214			6	2.69	23.8	268.8
CAL-281	8/28/2018	42.13033	-85.189623	272.2	20	2.78	2.48	3.421	11.02	3.3994	1.15	3.3452	7	2.78	22.7	249.5